TÉCNICO LISBOA

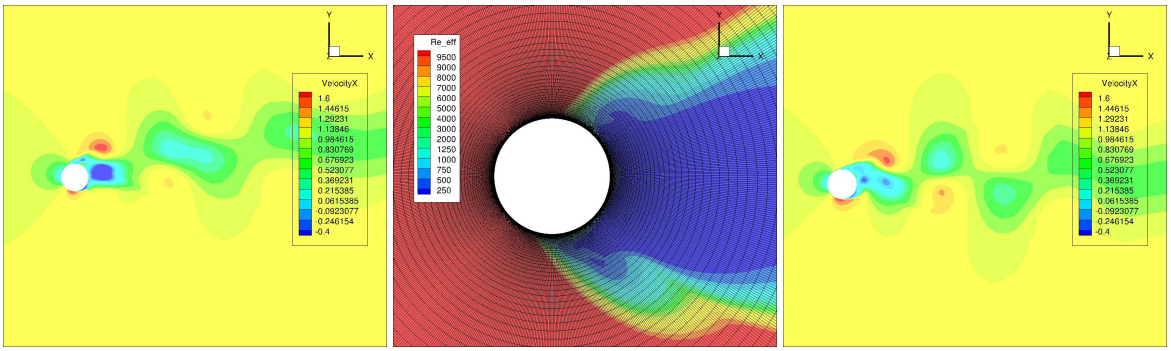

Assessing RANS numerical and modelling properties in the simulation of the flow around fixed and moving cylinders

Rita Jesus de Mendonça e Costa

Thesis to obtain the Master of Science Degree in

Aerospace Engineering

Supervisor: Prof. Luís Rego da Cunha de Eça

Examination Committee

Chairperson: Prof. Fernando José Parracho Lau

Supervisor: Prof. Luís Rego da Cunha de Eça

Member of the Committee: Dr. Guilherme Nuno Vasconcelos Beleza Vaz

November 2019

To the most special dreamers - my parents, Ana Paula and Jorge.

Acknowledgements

I would like to express my sincere gratitude to my supervisor, Prof. Luís Eça, for the opportunity to work in this project in the scope of the collaboration IST/MARIN. Furthermore, I would like to thank him for his guidance, comments and suggestions throughout this work; for his encouragement, inspiration and unwavering support over the past months. Additionally, a very special thank you to Rui Lopes - for his constant advice, help, availability and eagerness to share his experience as a PhD student. Finally, I am grateful to Eduardo Fernandes, my MSc. fellow student, with whom I had the chance to share an office during the development of this work, and many working hours at IST, often filled with productive discussions concerning both our research topics.

This work would not have been possible without the commitment and inspiration from my previous educators. To my teachers, mentors, Professors, I would like to address a word of kind appreciation, for motivating and challenging me to always go an extra mile in my academic studies and to pursue my goals confidently.

To my colleagues and closest friends, I thank you for your enthusiasm, support, and countless hours of teamwork. I thank you for your unconditional encouragement through the (many!) hard times, for the laughters and moments shared, which I shall always remember fondly.

Last, but certainly not least, a heartfelt thank you to my family, for their reassuring presence, affection and support over the past months. And finally, in particular, a word of immense gratitude to my parents, for their unconditional love, patience and encouragement throughout the years. For nurturing and guiding me in my personal growth, I am forever grateful.

Resumo

A análise do escoamento em torno de corpos não fuselados encontra-se detalhada na literatura, uma vez que fornece um caso canónico para a verificação de soluções e validação de modelos matemáticos. Adicionalmente, o escoamento compreende fenómenos físicos complexos (transição, separação, libertação de vórtices...) ao longo de uma larga gama de números de Reynolds, cujo estudo tem aplicações na aeronáutica e nas energias renováveis *offshore*.

Esta dissertação foca-se no escoamento estatisticamente não estacionário em torno de um cilindro circular, a um número de Reynolds de 1×10^4, em condições fixas e de movimento imposto. As equações de Navier-Stokes em média de Reynolds (RANS) são utilizadas para modelação, (captação das propriedades médias do escoamento, no sentido de uma média de conjunto), e completadas com o modelo de turbulência $k - \omega$ SST.

Estudam-se casos bidimensionais. Analisam-se técnicas de movimento/deformação de malha para tratar o movimento imposto, e avalia-se a respetiva influência nas condições fronteira aplicadas ao domínio computacional. Apresenta-se ainda um procedimento sistemático para calcular o erro estatístico, iterativo, e de discretização (tanto para o caso fixo como de movimento imposto), bem como uma breve análise dos resultados de casos tridimensionais.

Finalmente, avaliam-se alguns detalhes do escoamento para casos de teste selecionados, realiza-se um exercício de validação, e discutem-se as limitações do modelo matemático escolhido. Demonstram-se as semelhanças entre os resultados obtidos com as várias técnicas de movimento/deformação da malha, e apresentam-se conclusões relativas aos casos em que a formulação RANS + $k - \omega$ SST capta ou não as propriedades médias do escoamento.

Palavras-chave: Cilindro, Fixo/Movimento imposto, Malhas móveis/deformáveis, RANS, Média de conjunto, $k - \omega$ SST.

Abstract

The analysis of the flow around bluff bodies is a well reviewed topic in computational fluid dynamics (CFD) since it provides a canonical test case to perform solution verification and mathematical model validation. Furthermore, it features complex physical phenomena (transition, separation, vortex shedding...) over a wide range of Reynolds numbers, whose study finds relevant applications in the fields of aeronautics and offshore renewable energies.

This work focuses on the statistically unsteady flow around a circular cylinder, at a Reynolds number of 1×10^4, in fixed and imposed motion conditions. The Reynolds-averaged Navier-Stokes (RANS) equations are used for modelling in order to capture mean flow properties (in the sense of an ensemble average), and closed with the $k - \omega$ SST turbulence model.

Two-dimensional test cases are studied. An analysis of the available moving/deforming grid techniques to handle imposed motion is performed, and the influence of the chosen technique on the selected set of boundary conditions for the computational domain is evaluated. A systematic procedure to calculate the statistical, iterative and discretisation error is presented, both for the fixed and imposed motion cases, and a brief analysis of results from three dimensional simulations is performed.

Finally, flow field details are evaluated for selected test cases, a validation exercise is presented, and the limitations of the mathematical model are discussed. Similarities in the results obtained with the moving/deforming grid techniques are shown, and insight is provided on cases in which the RANS + $k - \omega$ SST formulation successfully/unsuccessfully captures the mean flow properties.

Keywords: Cylinder, Fixed/Imposed Motion, Moving/Deforming grids, RANS, Ensemble average, $k - \omega$ SST.

Contents

List of Tables

List of Figures

Nomenclature

2D Two dimensional

3D Three dimensional

BC Boundary conditions

BC-DEF Boundary conditions corresponding to the deforming grid setup

BC-MVG Boundary conditions corresponding to the moving grid setup

CDS Central Difference Scheme

FFT Fast-Fourier-Transform

FOU First Order Upwind

IDW Inverse Distance Weighting

$k - \omega$ SST (Menter's) Shear Stress Transport Turbulence Model

LES Large Eddy Simulations

RANS Reynolds-Averaged Navier-Stokes Equations

RBF Radial Basis Functions

Greek symbols

α_{exp} Explicit under relaxation factor.

α_{imp} Implicit under relaxation factor.

ϵ Turbulence dissipation rate.

μ Dynamic viscosity of the fluid.

μ_t Dynamic turbulent (eddy) viscosity.

ν Kinematic viscosity of the fluid.

ν_t Kinematic turbulent (eddy) viscosity.

ρ Density.

τ Shear stress.

$\overline{\phi}$ Average value of a given quantity ϕ.

ω Specific turbulence dissipation rate.

Ω Vorticity.

Roman symbols

A Amplitude of cylinder motion.

C_D Drag coefficient.

C_L Lift coefficient.

D Cylinder diameter.

f_s Vortex shedding frequency.

F_x Total force on the cylinder along the x direction.

F_y Total force on the cylinder along the y direction.

k Turbulence kinetic energy.

L Cylinder length.

L/D Cylinder aspect ratio.

m_x Quantity of interest for the ensemble of the N samples.

N Number of samples to be used for error estimation.

N_b Number of nodes on the boundary of the domain (RBF).

n_g Number of grids.

N_{sp} Number of surface points (RBF).

N_{vp} Number of volume points (RBF).

p Pressure.

Re Reynolds number.

S Strain rate.

s Standard deviation associated to each variable of interest.

St Strouhal number.

T_i Cylinder imposed motion period.

u Absolute uncertainty associated to each variable of interest.

U, U_∞ Inflow velocity.

U_R Reduced velocity.

x_i Quantity of interest for each of the N samples.

y^+ Dimensionless wall distance.

Subscripts

A_{ij} Coefficient matrix of the linear system.

avg Average value of a given quantity.

RHS_i Right-hand side vector of the linear system.

rms Root-mean square value of a given quantity.

u_i Cartesian velocity components (tensor notation).

x_i Cartesian coordinates (tensor notation).

Superscripts

ϕ' Fluctuation of a given quantity ϕ, with respect to the average value $\overline{\phi}$.

Chapter 1

Introduction

The analysis of the flow around cylinders employed in the supporting structures of offshore platforms has proved to be a fairly well-reviewed topic, being extensively documented in ocean engineering literature. Moreover, recent studies have been focusing on a more specific analysis, within the scope of low aspect ratio cylinders (being this quantity defined as the ratio between the cylinder length, L, and the cylinder diameter, D). In fact, low aspect ratio cylinders are known to model offshore platform support structures (e.g. spar, monocolumn) more accurately than the far more analysed infinite cylinders (or with a substantially larger aspect ratio), which is one of the prime reasons for the growing interest in their analysis, concerning maritime applications.

As for aeronautical applications, the study of the flow around bluff bodies has gained particular relevance in the noise-reduction studies performed for landing gears; in these cases, the analysis of the wake phenomena observed in bluff bodies provides fundamental insight to identify noise sources and subsequently carry out geometry/design modifications. Thus, investigating the landing gear contribution for overall airframe noise is fundamental to comply with the strict noise regulations concerning the approach phase. [1] [2]

1.1 Motivation

From a general standpoint, the numerical analysis of the flow around offshore structures can be considered relevant for several reasons. Either to predict a certain behaviour in a possible situation/scenario or to evaluate the feasibility of a proposed design, numerical analysis procedures (such as CFD) prove their importance in providing answers to the aforementioned needs. It is also crucial to outline that the use of CFD codes in preliminary and conceptual design stages allows a better understanding of the most relevant physical phenomena involved, and, ultimately, leads to more efficient, time and cost-saving design strategies.

As a result, the necessity to better predict offshore structures' behaviour, in order to improve development quality and reduce costs has proved to be one of the main reasons to further investigate the flow around low aspect ratio cylinders, that correctly model the currently employed supporting devices in this

type of environment.

Neverteheless, the study of the flow around bluff bodies finds relevant applications in other fields of expertise. Concerning the aerospace sector, recent studies such as [3] have focused on the use of ”low aspect ratio circular pins as a flow control means to mitigate separation over a flapped airfoil”. Studying the flowfield resulting from the ”interaction of a low aspect ratio static/dynamic cylindrical pin with a laminar boundary layer over a flat plate”, it was found that adding motion to the cylinder increased the strength of the generated vortical structures, ”increased downwash over the pin and entrainment of fluid around the cylinder sides”. Furthermore, the analysis of Gildersleeve *et. al* [3] showed that the use of the fixed array of pins ”demonstrated reduction (or complete mitigation) of the separated flow over the control surface, as well as a change in the global circulation”, thus predicting an enhancement of the lift force and reduction of drag; moreover, the aforementioned study shed light on the potential of finite span, low aspect ratio cylinders as a valid strategy for flow control.

1.2 Topic Overview and scope of the investigation

The flow around the cylinders in an offshore platform can become a fairly cumbersome problem if one fails to make the correct assumptions at an early stage. Namely, it is important to concisely state the problem to be studied and the simplifications chosen in the scope of the research.

As it was previously mentioned, the study of low aspect ratio cylinders has recently gained some importance in the literature, mainly focusing on the 3D effects of the flow when opposed to the analysis of infinite (2D) cylinders. [4] [5] [6]. Yet another important variable to be taken into account is the difference between the flow around a fixed and a moving cylindrical body.

Extensive studies have been carried out regarding the analysis of fixed cylinders. A first downside to this approach is the fact that it does not accurately model the real behaviour observed in an offshore structure (the cylinders **do** move). Additionally, previous studies have shed light on the limitations of the numerical modelling of fixed cylinder cases: in [7], the Unsteady Reynolds Averaged Navier Stokes (URANS) equations (together with a turbulence model) were used to better understand the role of turbulence on the flow. It was found that the use of standard turbulence models (such as the $k-\omega-SST$) often resulted in an inaccurate prediction of the turbulent flow scales, therefore requiring improved formulations such as the SAS (Scale Adaptive Simulation).

In a clear contrast to the fixed cylinder scenario, the investigation on moving cylinders is not as detailed or widespread. Despite the insight of the authors of [5] regarding the behaviour of such cylinders when allowed some degrees of freedom (DOF), and the material found in [7] concerning the relative importance of turbulence modelling in the cases involving driven or freely moving cylinders, additional aspects concerning the movement have not yet been appropriately and extensively tackled. Namely, when focusing on the implementation of **moving/deforming** grids, there is no clear trend in the selection of deforming/moving methods, making the available results in the literature difficult to be accurately assessed or even reproduced. As a result, it can be argued that a lack of understanding of the behaviour of low aspect ratio moving cylinders still prevails.

1.3 Objectives

The core aim of the present work is to study the flow around fixed and moving cylinders (imposed periodical motion), in the latter case through the use of moving and deforming grid techniques, with different sets of boundary conditions applied. Additionally, since no clear agreement has been found in the available literature regarding the choice of **deforming**/**moving** grid methods to accurately simulate the movement, the present study aims at providing further insight on this topic, analysing the problem from a numerical standpoint and assessing the modelling error of the obtained results, taking as a reference the available experimental data from the literature.

Furthermore, there is a focus on the analysis of some relevant flow features (such as the characterization of the vortical patterns in the cylinder wake) and on the discussion of the recorded differences between the 2D and 3D test cases.

An additional objective is to diagnose relevant techniques allowing to identify if the Reynolds equations in a statistically unsteady problem (such as the moving cylinder) are capturing exclusively the mean flow. If the diffusion provided by the turbulence model is not sufficient, there is a risk to start solving unwanted fluctuations.

The main goals of this investigation can be summarized in the following questions:

- How does the choice of **boundary conditions** applied to the computational domain influence the obtained results, both in fixed and moving cylinder cases?
- How does the choice of **deforming**/**moving** grid methods influence the accuracy of the numerical solution obtained when the cylinder is externally forced to move?
- What are the main differences registered in the convergence properties of the fixed and moving cases?
- What are the main differences registered in the flow around the cylinder in the 2D and 3D cases?
- In which cases are the Reynolds equations a suitable modelling approach for statistically unsteady problems? Moreover, how can this suitability be assessed?

1.4 Thesis Outline

The present work has been divided into several chapters, each focusing on different aspects relevant for the investigation:

- Chapter 2 focuses on some of the most relevant state-of-the-art information found in the literature, regarding the fundamental, theoretical differences of the flow around infinite and low aspect ratio cylinders. A brief review of the different vortex shedding patterns displayed by the wake of cylinders (according to the Reynolds number selected) is also presented, along with a description of well-known vortex synchronization regions for the imposed motion cases.

- Chapter 3 defines the problem to be approached, by stating the mathematical model, characterizing the computational domain and defining the sets of boundary conditions to be used.
- Chapter 4 describes in some detail the numerical options used in the software *ReFRESCO* [8] to numerically solve the selected mathematical formulation of the problem. In addition, the characteristics of the generated grids (used to discretise the computational domain) are presented, followed by a brief description of the mesh deformation and moving mesh algorithms employed in the moving cylinder cases (theoretical formulation + most relevant implementation details on the software *ReFRESCO*). Finally, the selected test cases are presented, and the quantities of interest to be monitored are stated.
- Chapter 5 first presents the necessary statistical, iterative, and grid refinement studies (in order to provide an estimation of the numerical accuracy of the computed solution) for the 2D test cases, followed by the most relevant results obtained for the corresponding 3D cases.
- Chapter 6 assesses the obtained results according to the initial expectations/predictions, in order to appropriately meet the originally devised goals. The selected literature data (mostly experimental) is taken as a reference, in order to provide an assessment of the modelling error.
- Chapter 7 attempts to briefly revisit some of the most relevant conclusions yielded by the project, while also presenting future paths to further develop the present investigation.

Chapter 2

Background

The study of the flow around cylinders has been extensively documented in the literature. Namely, the flow around infinite or very high aspect ratio cylinders has been investigated as a common academic case, as it provides a very clear insight on the relevant structures formed within the flow. In its most simplified numerical treatment, it can be seen as a two-dimensional (2D) approximation of the problem, and it is therefore considered a necessary starting point to any investigation, as it yields preliminary results relevant for comparison with a more complex formulation of the same problem: the three-dimensional case (3D).

Likewise, the three-dimensional analysis of the flow around cylinders has also been a well-reviewed topic among the scientific community over the years [4] [5] [9] [10] . Namely, the analysis of low aspect ratio cylinders has received growing attention, as they accurately model the spar/mono-column structures employed in offshore platforms [5] and therefore represent a relevant case study. Furthermore, these cases clearly display the most relevant three-dimensional features of the flow. In particular, authors [4] have verified that for extremely low aspect ratios (for example, for values of $0.2 \leq L/D \leq 0.5$), free end effects were found to be predominant. In spite of an absence of von-Kármán street characteristics around the majority of the length of the cylinder, vortex shedding is responsible for producing alternating forces in the transverse direction. Namely, the interaction between the trailing vortices with streamwise vorticity is the main cause for the force generation in the direction perpendicular to the inflow. All in all, the work reported in [4] presents a comprehensive analysis of the distinctive features of the flow around fixed, low aspect ratio cylinders.

Another aspect that has received some attention within the scope of this problem is the importance of free surface effects. The work developed by [4] investigated the flow around low aspect ratio cylinders piercing a free surface. However, the studies performed by [11] identified a superior limit for the Froude number, below which the free surface effects can be considered negligible. It should be outlined that the numerical modelling of free-surface effects in the context of this problem has also received some previous attention, in works such as [6]. However, as previously discussed, the main objective of the present work was not to provide additional focus on the free-surface effects (mainly due to the possibility to neglect them following the aforementioned criterion identified by [11]), and therefore the literature

references focusing on this topic were solely used to provide a better understanding of the state of the art for the cylinder problem.

Finally, the experimental work of [5] and numerical contributions of [12] shed additional light on the understanding of the flow around moving cylinders (both in free motion and imposed motion). In [12] a moving grid approach was used for the numerical treatment of the mesh used in the moving cylinder case, which proved to be a valuable standpoint to further investigate the numerical treatment given to this case, and identify other possibilities (deforming grid methods) to address this problem in the present investigation.

All in all, it is important to outline that the literature background focused so far is mostly relevant for the analysis of the differences found between 2D and 3D cases (which were only superficially covered in the present study), and potentially, for further studies concerning free motion cases (which were not addressed in the present analysis). Nonetheless, this literature review was considered helpful to appropriately outline some of the most recent work concerning the flow around bluff bodies.

2.1 Theoretical Overview

The following subsections present a theoretical description of some of the most significant features characterizing the flow around cylinders, in order to provide a better description of the studied problem in this investigation. While subsection 2.1.1 again focuses on the main differences between 2D and 3D cases, subsections 2.1.2 and 2.1.3 deepen the analysis by providing the necessary background concerning the flow regimes in a fixed setup (according to the selected Reynolds number) and wake characteristics (vortex synchronization patterns) in imposed motion setups.

2.1.1 Flow around 2D (Infinite) Circular Cylinder vs Finite Circular Cylinder

The flow around infinite circular cylinders has been extensively explored, due to the phenomenon of vortex shedding. The boundary layer developing from the surface separates, therefore causing the resulting shear layer to become unstable. Consequently, it evolves into a vortex in the wake region, which is eventually washed away from the cylinder. At the opposite side of the cylinder, the same aforementioned phenomena are observed, therefore producing and shedding a counter-rotating vortex (with respect to the first one described). This behaviour, characterized by the alternating generation and shedding of counter-rotating vortices, is known as a von-Kármán vortex street. [13]

While the wake of a 2D cylinder displays the aforementioned von-Kármán vortex street (over a wide range of Reynolds numbers), for a finite height cylinder mounted on a flat plate, the wake becomes far more complex, as three-dimensional effects become predominant. The study of the flow around finite height cylinders mounted on a flat plate has motivated several discussions, therefore turning this topic into a deeply and widely reviewed one among the scientific community [14] [9].

In [9] the authors experimentally investigated the turbulent wake of a circular cylinder mounted to a wall and partially or fully immersed in a turbulent boundary layer. The aspect ratios tested were $L/D =$

$3, 5, 7, 9$, at a Reynolds number $Re_D = 6 \times 10^4$ (which falls into the subcritical regime). In this study, the wall-normal and streamwise velocity components were measured, and the mean velocity, turbulence intensity and Reynolds shear stress fields were obtained. The authors identified a comparable turbulent wake structure for the cylinders with aspect ratios of $5, 7$ and 9. In fact, these displayed a region with low streamwise velocity and high turbulence intensity behind the cylinder, and further verified that this region was limited by the four main streamwise vortex structures (a counter-rotating pair of tip vortices originating from the free end, and another pair of counter-rotating vortices, within the flat plate boundary layer). Additionally, the two tip vortices were found to comprise a region with a strong downwash velocity in between them, whereas the base vortices limited an area with an upwash velocity (closer to the ground plane). Finally, and through an analysis of the Reynolds shear stresses, the authors identified a change of sign downstream of the cylinder, in the region where the upwash and downwash flow fields intersected.

However, the results found for the shortest cylinder (that is, with the lowest aspect ratio, 3) indicated a distinct wake structure, namely due to the fundamentally different flow field observed near the flat plate (absence of base vortices and consequent upwash velocity field). Furthermore, a fundamental difference regarding the von-Kármán vortex shedding was outlined: while a strong vortex shedding signal was registered for $L/D = 5, 7, 9$ (along the majority of the cylinder height), this behaviour was quite weaker or mostly absent for the lowest aspect ratio cylinder that was investigated ($L/D = 3$).

As a result, it is relevant to mention that the work provided by [9] identified not only major characteristics of the flow field of finite cylinders, but also the properties of the transitional turbulent wake structure for low aspect ratio cylinders. Nevertheless, it should be outlined that the transitional regime strongly depends, as stated by the authors, on "the cylinder's aspect ratio, and the thickness of the boundary layer developed on the wall relative to the cylinder height and diameter, i.e. the ratios δ/H and δ/D".

The work in [4] shed additional light on the study of very low aspect ratio cylinders. The authors investigated the flow around stationary circular cylinders, in a range of L/D from 0.1 to 2. Some of the most important results displayed a decrease in the drag force coefficients with decreasing aspect ratio, and a decrease in the non-dimensional vortex-shedding frequency (Strouhal number), also with decreasing aspect ratio. This behaviour shows an appropriate agreement with the previously described results, by [9]. Additionally, the study developed by the authors of [4] identified a predominance of free-end effects in the cylinder for aspect ratio values $L/D \leq 0.5$ (which again reinforces the importance of the three-dimensional behaviour of the flow in very low aspect ratio cylinders, also extensively discussed in [15] and [9]). However, an important finding in the investigation carried out in [4] was the existence of alternating forces in the plane perpendicular to the freestream, in the range $0.2 \leq L/D \leq 0.5$. Indeed, the authors found that despite the absence of von-Kármán vortex street characteristics (common in the wake of larger aspect ratio cylinders), the generation of transverse forces was motivated by the vortical structures created around the cylinder free end. Additionally, it was suggested that the recirculation regions (identified below the cylinder free end and behind the cylinder) could be responsible for the production of the well-known arch-type vortices. Consequently, it was identified that these structures, plus the trailing vortices (with main vorticity streamwise) were the main causes for the transverse forces

observed in the low aspect ratio cylinders. As indicated by the authors, this is confirmed by the low frequency registered in the vortex shedding phenomenon for the range of aspect ratio values considered.

2.1.2 Vortex shedding and flow regimes

The wake of bluff bodies (namely, circular cylinders) has been an important aspect in classical Fluid Mechanics since the early years of the 20th century. The work of von Kárman in 1912 [16], which essentially connected the vortex street structure observed in the cylinder wake and the resulting drag force on the body, was one of the primary roots of a great deal of subsequent papers focusing on the analysis of vortex dynamics. The Strouhal number (St) characterizes, in a non-dimensional way, the frequency of the vortex shedding phenomenon:

$$St = \frac{f_s D}{U} \tag{2.1}$$

in which f_s is the (dimensional) vortex shedding frequency, D is the cylinder diameter and U is the inflow velocity. Williamson [17] collected a very thorough historical perspective on the developments concerning the wake of bluff bodies. Namely, in his work [17], an overview of vortex shedding regimes across a wide range of Reynolds numbers is presented. According to this publication, the identification of instabilities (that differentiate the several flow regimes) can be performed through the monitoring of the base suction coefficient behaviour, with respect to the Reynolds number.

Naturally, it can be argued that the transitions between the aforementioned flow regimes can be affected by a handful of factors. In [17], turbulence levels, roughness, and cylinder aspect ratio are listed as common examples. However, it is still possible to identify the behavioural trends in the base suction coefficient, that allow an identification of flow regimes. The first experimental measurements that allowed this identification were performed by Roshko, and in his 1954 article [18] three different regimes were identified:

- For Re=40-150, a stable (that is, periodic) and laminar vortex shedding pattern was identified;
- For Re=150-300, a transition regime was found;
- For Re=300-10000+, an irregular regime (characterized by distinct irregularities in the velocity fluctuations) was observed.

Williamson [17] collected data from subsequent studies from Henderson (1995), Williamson and Roshko (1990), Norberg (1987), Bearman (1969), Flaschbart (1932), and Shih et al. (1992), which allowed a more complete definition than the one suggested by Roshko with his 1954 work. With the aforementioned contributions, it was possible to map the base suction coefficient trend up to a Reynolds number of 8×10^6 (Shih et al. 1992).

The identified regimes range from the **laminar steady regime**, with a steady recirculation region comprising two symmetrical vortices on each side of the wake (for $Re < 49$), followed by the **laminar vortex shedding**, and subsequent **wake transition**, **shear layer transition** and **boundary layer transition**. The sequence of regimes is mainly motivated by fundamental shear flow instabilities (thoroughly

detailed in [17]), whose description is beyond the scope of the current investigation. For $Re = 1 \times 10^4$ (Reynolds number of the present computations), the flow is in the **shear layer transition regime** (which, according to the data collected by Williamson in [17], comprises all Reynolds numbers ranging from 1×10^3 to 2×10^5). Over this range, there is an increase in the base suction coefficient, along with an increase in the 2-D Reynolds stresses and a decrease in the Strouhal number.

2.1.3 Vortex synchronization regions for imposed motion cases

The analysis of the behaviour of a cylinder when excited with an external frequency (that is, in a situation of periodic imposed motion) is a topic on its own that has also received significant attention over the years. Namely, the influence of the frequency and amplitude of the excitation on the natural vortex shedding patterns of the cylinder has been studied in detail by Williamson [19], who characterized the several vortex synchronization regions as a function of the period/amplitude of the imposed motion. Figure 2.1 displays the several regions identified, according to the relevant parameters, **amplitude** and **wavelength** ratio (most commonly referred to as **reduced velocity**), defined as follows:

$$Amplitude\,ratio = \frac{A}{D} \tag{2.2}$$

$$Wavelength\,ratio\,(Reduced\,velocity) = \frac{UT}{D} = \frac{\lambda}{D} \tag{2.3}$$

Figure 2.1 displays the several possible vortex synchronization regions as a function of the two aforementioned parameters. According to the definition chosen by Williamson his work [19], the possible vortical patterns are named as **P** (vortex pair) and **S** (single vortex). The number of single vortices and vortex pairs shed per cycle are also defined: for example, the pattern **2P+2S** corresponds to **two** pairs of vortices and **two** single vortices being shed in each cycle.

Additional patterns such as **C(2S)** and **C(P+S)** are present. In these cases, **2S** or **P+S** vortical structures are present right behind the cylinder, followed by an immediate coalescence of ”smaller vortices (...) into larger scale structures”. Finally, mode **2P*** is quite similar to mode **2P**, except that in the former ”vortex pairs in one of the half cycles convect away from in front of the body”. Figure 2.2 presents a summary of the previously described patterns.

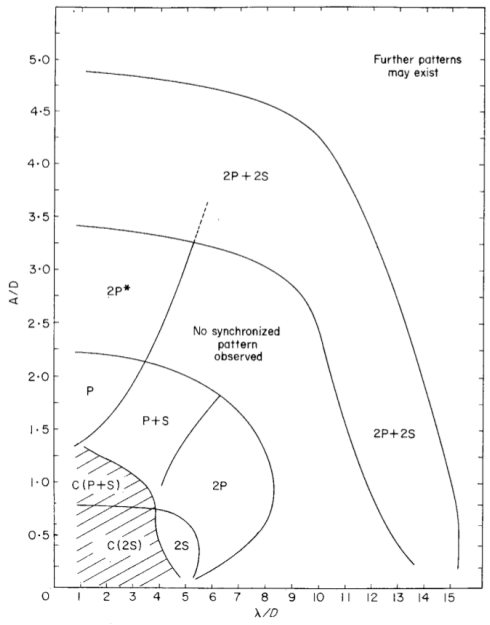

Figure 2.1: Vortex synchronization regions in the oscillating cylinder near wake, identified by Williamson [19].

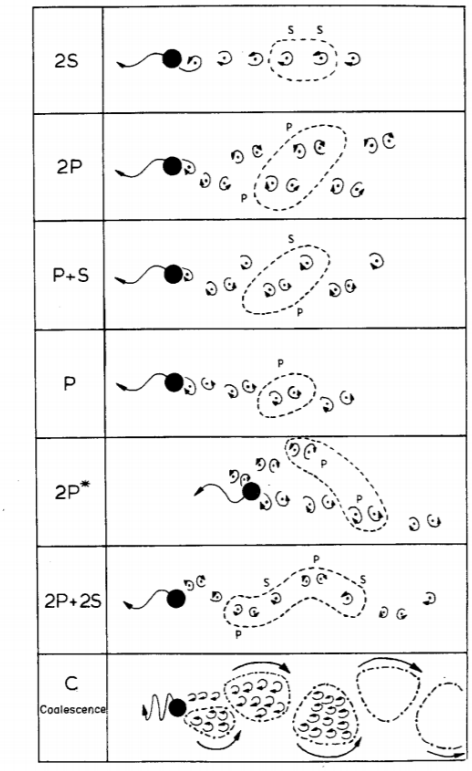

Figure 2.2: Illustration of the possible vortical patterns, as described by Williamson [19].

Chapter 3

Problem Formulation

3.1 The RANS formulation for unsteady flows

A full/direct solution of the Navier-Stokes equations is only manageable in very specific situations (for example, for small computational domains and low Reynolds numbers) and often does not represent a clear advantage [20] when only mean properties of the flow are sought (for example, the average forces on a cylinder's wall).

Consequently, when solving turbulent flows, it is often useful to adopt a Reynolds decomposition approach to deal with the intrinsically unsteady features of turbulence. The Reynolds decomposition can be applied to both steady and unsteady flows, being the only difference between the two the **definition of the mean value** of the decomposition:

- In **steady flows**, the mean value of the decomposition represents the **time average** of the quantity of interest;
- In **unsteady flows**, the mean value of the decomposition represents the **ensemble average** of the quantity of interest.

From this point onwards, the formulation will focus on the specific case of **unsteady flows**, since these are the relevant case for the present investigation. Introducing the Reynolds decomposition for unsteady flows in the Navier Stokes equations, and applying the same averaging to the mass and momentum balance, the obtained formulation is the so called *Unsteady Reynolds-Averaged Navier Stokes Equations*.

3.1.1 Reynolds decomposition

The Reynolds decomposition is a mathematical technique that allows a separation between the mean value of a certain quantity from the fluctuations with respect to the mean value. For a given quantity ϕ, and considering unsteady flow:

$$\phi(x_i, t) = \overline{\phi}(x_i, t) + \phi'(x_i, t) \tag{3.1}$$

It shall be noticed that, for an unsteady flow, the elimination of the time dependence for the mean value is not possible (which reflects the aforementioned need to adopt an ensemble averaging process). Consequently, the mean value for an unsteady flow (ensemble average) is computed as follows:

$$\overline{\phi}(x_i,t) = \lim_{N\to\infty} \frac{1}{N}\sum_{n=1}^{N} \phi(x_i,t) \tag{3.2}$$

This averaging procedure takes N as a number of realizations (that is, an "imagined set of flows in which all controllable factors are kept fixed", as stated by [20]). Being N the number of members of the ensemble, it should be as large as possible (ideally, infinite) in order to obtain statistical convergence.

3.1.2 Averaged continuity and momentum equations

From equation 3.2, it can be seen that the mean of any fluctuation is zero (that is, $\overline{\phi}' = 0$) [21]. Consequently, if a term is linear, averaging yields the term itself for the averaged quantity. However, averaging a product of two terms yields:

$$\overline{u_i\phi} = \overline{(\overline{u_i} + u_i')(\overline{\phi} + \phi')} = \overline{u_i}\,\overline{\phi} + \overline{u_i'\phi'} \tag{3.3}$$

Two additional terms would appear in equation 3.3: $\overline{\overline{u_i}\phi'}$ and $\overline{\overline{\phi}u_i'}$. However, these vanish precisely because the average of a fluctuating quantity is zero [22]. The last term present in 3.3, however ($\overline{u_i'\phi'}$), is usually non-zero because the quantities are correlated in turbulent flows; namely, terms such as $\rho\overline{u_i'u_j'}$ in the conservation equations are called the *Reynolds stresses*, and terms such as $\rho\overline{u_i'\phi'}$ are designated *turbulent scalar flux*.

Applying the averaging technique to the continuity and momentum equations, the following result is obtained (for incompressible flow), in tensor notation and Cartesian coordinates:

$$\frac{\partial(\rho\overline{u_i})}{\partial x_i} = 0 \tag{3.4}$$

$$\frac{\partial(\rho\overline{u_i})}{\partial t} + \frac{\partial}{\partial x_j}\left(\rho\overline{u_i}\,\overline{u_j} + \rho\overline{u_i'u_j'}\right) = -\frac{\partial\overline{p}}{\partial x_i} + \frac{\partial\overline{\tau_{ij}}}{\partial x_j} \tag{3.5}$$

In equation 3.5. $\overline{\tau_{ij}}$ are the components of the mean viscous stress tensor. For incompressible flow:

$$\overline{\tau_{ij}} = \mu\left(\frac{\partial\overline{u_i}}{\partial x_j} + \frac{\partial\overline{u_j}}{\partial x_i}\right) \tag{3.6}$$

The presence of the aforementioned *Reynolds stresses* is clear in the momentum equation. An additional equation for the mean of the scalar quantity, $\overline{\phi}$, could also be derived (which would yield the term corresponding to the *turbulent scalar flux*. Additional details on this derivation can be found on [20] and are herein ommited.

As expected, the additional terms (Reynolds stresses and turbulent scalar flux) produce a system of conservation equations that **requires closure**. Turbulence models are needed to prescribe values

to these additional terms, through modelling approximations that allow the computational treatment of these equations. The following section will further detail one of these possible models - the $k-\omega$ SST, used in the present study.

3.2 The $\mathrm{k}-\omega$ SST turbulence model

The $k-\omega$ SST (Shear Stress Transport) model was first presented by Menter in [23]. This model was based on the original $k-\omega$ Wilcox model [24], presenting however further capacities to account for the transport of the principal turbulent shear stress in adverse pressure gradient boundary layers [23].

3.2.1 Motivation for development of the $k-\omega$ SST

The $k-\omega$ SST turbulence model fits in the category of two-equation eddy viscosity models (which are considered to be the most popular non-algebraic turbulence models), comprising therefore two transport equations: one for the turbulence kinetic energy, related to the velocity scale, and another related to the turbulence length (or time) scale. It shall be mentioned that the development and growth of non-algebraic models mainly rooted in the reasons listed below:[23].

- The need for independence from the specification of an algebraic length scale;
- The need for a compromise between numerical robustness and computation time/efforts;
- The need for independence from ambiguous and often variable quantities, such as specified free-stream values.

The $k-\epsilon$ model - an extremely popular two-equation model - remains quite successful in a wide range of flow simulations; however, one of its most significant shortcomings resided in a severe lack of sensitivity to adverse pressure gradients. In fact, the model displayed a tendency to overestimate the shear stress values, consequently leading to an erroneous delay or prevention of flow separation. Concerning this aspect, the original $k-\omega$ model and the BSL $k-\omega$ model [23] (a blending between the original $k-\omega$ and a transformed formulation of the $k-\epsilon$) granted better performance than the standard $k-\epsilon$. Nevertheless, in severe adverse pressure gradients, an underprediction of flow separation was still clear.

In order to mitigate this fragility of the models, Menter [23] developed the $k-\omega$ SST model, modifying the eddy viscosity formulation of the BSL, thus accounting for the transport effects of the principal turbulent shear stress. This modification rooted on the **Johnson-King** model [25], which assumed the turbulent shear stress to be proportional to the turbulence kinetic energy in the logarithmic and wake regions of a turbulent boundary layer [26]. Furthermore, the Johnson-King formulation exhibited a very successful behaviour in adverse pressure gradient situations.

3.2.2 The formulation of the baseline (BSL) model

The $k-\omega$ SST derives from the BSL model (two zone model, comprising the original $k-\omega$ formulation exclusively in the near wall region and a transformed $k-\epsilon$, applied for free shear layers). The BSL model equations (for the two zones) are presented below.

Original $k-\omega$ model

$$\frac{D(\rho k)}{Dt} = \tau_{ij}\frac{\partial \overline{u_i}}{\partial x_j} - \beta^*\rho\omega k + \frac{\partial}{\partial x_j}\left[(\mu + \sigma_{k1}\mu_t)\frac{\partial k}{\partial x_j}\right] \tag{3.7}$$

$$\frac{D(\rho\omega)}{Dt} = \frac{\gamma_1}{\nu_t}\tau_{ij}\frac{\partial \overline{u_i}}{\partial x_j} - \beta_1\rho\omega^2 + \frac{\partial}{\partial x_j}\left[(\mu + \sigma_{\omega 1}\mu_t)\frac{\partial \omega}{\partial x_j}\right] \tag{3.8}$$

Transformed $k-\epsilon$ model

$$\frac{D(\rho k)}{Dt} = \tau_{ij}\frac{\partial \overline{u_i}}{\partial x_j} - \beta^*\rho\omega k + \frac{\partial}{\partial x_j}\left[(\mu + \sigma_{k2}\mu_t)\frac{\partial k}{\partial x_j}\right] \tag{3.9}$$

$$\frac{D(\rho\omega)}{Dt} = \frac{\gamma_2}{\nu_t}\tau_{ij}\frac{\partial \overline{u_i}}{\partial x_j} - \beta_2\rho\omega^2 + \frac{\partial}{\partial x_j}\left[(\mu + \sigma_{\omega 2}\mu_t)\frac{\partial \omega}{\partial x_j}\right] + 2\rho\sigma_{\omega 2}\frac{1}{\omega}\frac{\partial k}{\partial x_j}\frac{\partial \omega}{\partial x_j} \tag{3.10}$$

$$\tau = -\rho\overline{u'v'} \tag{3.11}$$

The BSL model is achieved through a blending of both sets of equations, using a function (F_1) which is **one** in the near wall region (and therefore activates the $k-\omega$ model) and **zero** away from the surface. Consequently, equations 3.7 and 3.8 are multiplied by F_1 and equations 3.9 and 3.10 are multiplied by $(1-F_1)$. Corresponding equations are then added together, yielding:

$$\frac{D(\rho k)}{Dt} = \tau_{ij}\frac{\partial \overline{u_i}}{\partial x_j} - \beta^*\rho\omega k + \frac{\partial}{\partial x_j}\left[(\mu + \sigma_k\mu_t)\frac{\partial k}{\partial x_j}\right] \tag{3.12}$$

$$\frac{D(\rho\omega)}{Dt} = \frac{\gamma}{\nu_t}\tau_{ij}\frac{\partial \overline{u_i}}{\partial x_j} - \beta\rho\omega^2 + \frac{\partial}{\partial x_j}\left[(\mu + \sigma_\omega\mu_t)\frac{\partial \omega}{\partial x_j}\right] + 2\rho(1-F_1)\sigma_{\omega 2}\frac{1}{\omega}\frac{\partial k}{\partial x_j}\frac{\partial \omega}{\partial x_j} \tag{3.13}$$

The constants in the resulting equations are computed using the constants from the original equations and the blending functions. Therefore, for any constant ϕ:

$$\phi = F_1\phi_1 + (1-F_1)\phi_2 \tag{3.14}$$

being ϕ_1 any constant corresponding to the original $k-\omega$ model and ϕ_2 any constant corresponding to the transformed $k-\epsilon$ model. The two sets of constants are listed below:

Set 1: Constants for the original $k-\omega$ (ϕ_1)

$$\sigma_{k1} = 0.5,\ \sigma_{\omega 1} = 0.5,\ \beta_1 = 0.0750 \tag{3.15}$$
$$\beta^* = 0.09,\ k = 0.41,\ \gamma_1 = \beta_1/\beta^* - \sigma_{\omega 1}k^2/\sqrt{\beta^*}$$

Set 2: Constants for the transformed $k-\epsilon$ (ϕ_2)

$$\sigma_{k2} = 1.0,\ \sigma_{\omega 2} = 0.856,\ \beta_2 = 0.0828 \tag{3.16}$$
$$\beta^* = 0.09,\ k = 0.41,\ \gamma_2 = \beta_2/\beta^* - \sigma_{\omega 2}k^2/\sqrt{\beta^*}$$

The eddy viscosity is defined as:

$$\nu_t = \frac{\mu_t}{\rho} = \frac{k}{\omega} \tag{3.17}$$

and the turbulent stress tensor $\tau_{ij} = -\rho\overline{u_i' u_j'}$ is expressed as:

$$\tau_{ij} = \mu_t \left[\frac{\partial \overline{u_i}}{\partial x_j} + \frac{\partial \overline{u_j}}{\partial x_i} - \frac{2}{3}\frac{\partial \overline{u_k}}{\partial x_k}\delta_{ij} \right] - \frac{2}{3}\rho k \delta_{ij} \tag{3.18}$$

The aforementioned blending function, F_1, is defined as [23]:

$$F_1 = \tanh\left(\arg_1^4\right) \tag{3.19}$$

with

$$\arg_1 = \min\left[\max\left(\frac{\sqrt{k}}{0.09\omega y}, \frac{500\nu}{y^2\omega} \right), \frac{4\rho\sigma_{\omega 2}k}{\mathrm{CD}_{k\omega}y^2} \right] \tag{3.20}$$

and

$$\mathrm{CD}_{k\omega} = \max\left(2\rho\sigma_{\omega 2}\frac{1}{\omega}\frac{\partial k}{\partial x_j}\frac{\partial \omega}{\partial x_j}, 10^{-20} \right) \tag{3.21}$$

the cross-diffusion term already present in equation 3.10.

3.2.3 The formulation of the Shear-Stress Transport (SST) model

As previously mentioned, one of the main novelties in the $k-\omega SST$ model roots on the work developed by Johnson and King [25], by accounting for the relevant effect of the transport of the principal turbulent shear stress, τ:

$$\frac{D\tau}{Dt} = \frac{\partial \tau}{\partial t} + \overline{u_k}\frac{\partial \tau}{\partial x_k} \tag{3.22}$$

As stated by Menter in [23], "The JK model features a transport equation for the turbulent shear-stress τ that is based on Bradshaw's assumption that the shear-stress in a boundary layer is proportional to the turbulence kinetic energy, k,:"

$$\tau = \rho a_1 k \tag{3.23}$$

a_1 a constant. However, in two-equation models, the shear-stress τ is obtained from

$$\tau = \mu_t \Omega \tag{3.24}$$

being $\Omega = \frac{\partial u}{\partial y}$ (for general flows, Ω is taken to be the absolute value of the vorticity). This relation can be rewritten for conventional two-equation models:

$$\tau = \rho \sqrt{\frac{Production_k}{Dissipation_k}} a_1 k \tag{3.25}$$

Menter also stated [23] that equation 3.25 can lead to an overprediction of τ, since in adverse pressure gradient flows "the ratio of production to dissipation can be significantly larger than 1." Moreover, in order for equation 3.23 to be satisfied in an "eddy-viscosity model sense", the eddy viscosity would have to be redefined as:

$$\nu_t = \frac{a_1 k}{\Omega} \tag{3.26}$$

Essentially, equation 3.26 ensures, as stated by Menter [23], that "τ does not change more rapidly than $\rho a_1 k$", whereas in conventional two-equation models "the turbulent shear-stress responds instantaneously to changes in the vorticity Ω, much like an algebraic eddy-viscosity model".

Equation 3.26 requires modification to account for the regions in which Ω goes to zero, thus producing infinitely high eddy-viscosities. Nevertheless, for adverse pressure gradient flows, "production is larger than dissipation for the largest part of the layer ($\Omega > a_1 \omega$). Therefore,

$$\nu_t = \frac{a_1 k}{max(a_1 \omega; \Omega)} \tag{3.27}$$

ensures that in most regions with an adverse pressure gradient, the maximum selected value in the denominator will be Ω, retrieving equation 3.26.

Last, but not least, it is necessary to limit the modification made to the SST model to wall bounded flows, in order to "recover the original formulation of the eddy-viscosity for free shear-layers". Similarly to the baseline (BSL) model, a blending function F_2 is applied:

$$\nu_t = \frac{a_1 k}{max(a_1 \omega; \Omega F_2)} \tag{3.28}$$

with F_2 being

$$F_2 = \tanh\left(\arg_2^2\right) \tag{3.29}$$

$$\arg_2 = \max\left(2\frac{\sqrt{k}}{0.09\omega y}, \frac{500\nu}{y^2\omega}\right) \tag{3.30}$$

In order to use this modification to the eddy viscosity along with the previously defined BSL model, it is necessary to adjust the first set of constants in order to correctly reproduce the behaviour for a flat plate boundary layer (namely, the diffusion constant σ_{k1}):

Set 1:

$$\sigma_{k1} = 0.85,\ \sigma_{\omega 1} = 0.5,\ \beta_1 = 0.0750,\ a_1 = 0.31 \tag{3.31}$$
$$\beta^* = 0.09,\ k = 0.41,\ \gamma_1 = \beta_1/\beta^* - \sigma_{\omega 1}k^2/\sqrt{\beta^*}$$

The second set of constants that was previously defined, set 2, remains unchanged.

3.2.4 The $k-\omega$ SST 2003

Some modifications were later performed to the SST model [27], [28]. The 2003 version was the one used in the software *ReFRESCO*, for all the simulations performed in the present work. The modifications in the formulation, relatively to the original (1993) version, are the following ones:

$$\nu_t = \frac{a_1 k}{max(a_1\omega; SF_2)} \tag{3.32}$$

in which the vorticity, Ω (present in the original description), is replaced by the use of the strain rate, S. Furthermore, the production term in the k equation

$$P_k = \tau_{ij}\frac{\partial u_i}{\partial x_j} \tag{3.33}$$

is complemented with the use of a limiter, being replaced in the k equation by:

$$P_k = min(P_k; 10\beta^*\rho k\omega) \tag{3.34}$$

It is worth outlining that the $k-\omega$ SST 2003 model implemented in *ReFRESCO* features a factor of 15, instead of 10 (as stated in equation 3.34) in the limiter. [29]

3.3 Computational Domain

The choice of an appropriate computational domain represented one of the first important decisions to be made regarding the simulations to be performed. The work developed in [6] and [12] was carefully analysed in order to identify possibly valid standpoints for the choice of boundary conditions. However, bearing in mind a final, important goal of validating the numerical work developed in the present project, the experimental work of Gopalkrishnan [30] was taken as a reference for the choice of computational

domain. This was found to be an appropriate selection since it would allow an accurate representation of the experimental conditions used in the aforementioned work.

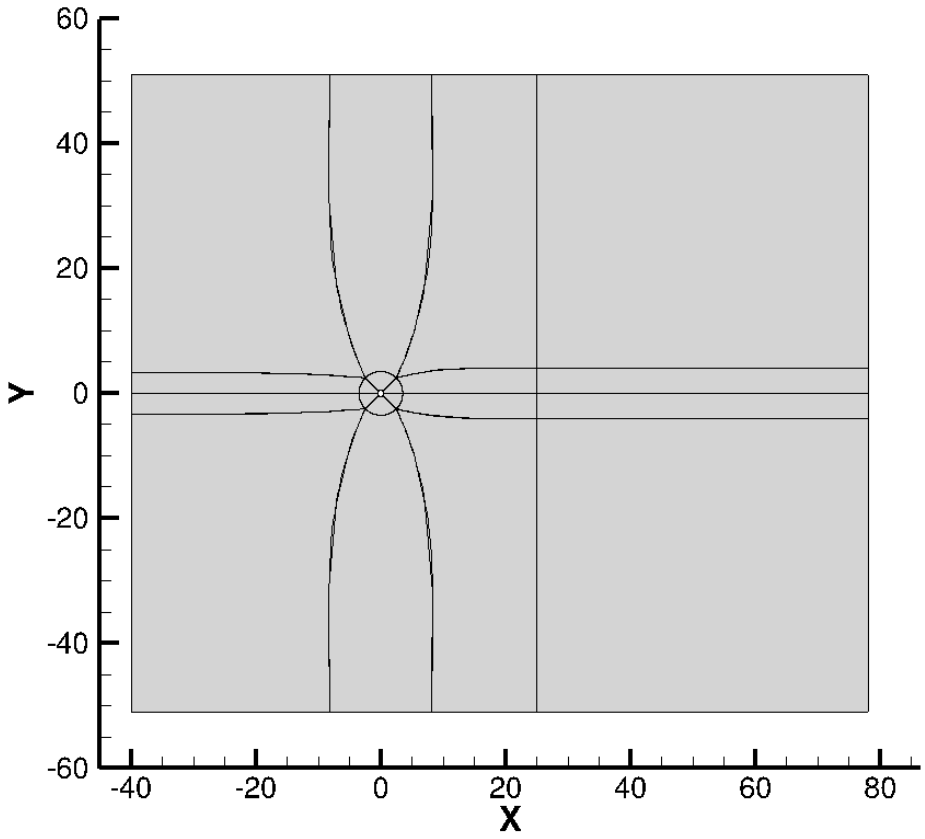

Figure 3.1: Computational domain dimensions.

As displayed in figure 3.1 (and taking the origin of the $x - y$ coordinate system to be placed at the center of the cylinder) the inlet of the rectangular domain was placed at $x = -40D$, the outlet at $x = +78D$ and the side walls at $y = +51D$ and $y = -51D$ (only half of the computational domain is displayed in the figure due to the obvious symmetry with respect to the x axis). The depth of the computational domain (along the z direction) was later adjusted according to the cylinder length used in the 3D test cases.

3.4 Boundary Conditions

The need to select appropriate boundary conditions to be employed in the chosen computational domain brought additional challenges. On the one hand, the first main goal was to select physically accurate BC in order to mimic the experimental conditions; on the other hand, it was fundamental to ensure compatibility between the chosen boundary conditions and the deforming/moving grids methods employed in the moving cylinder test cases. It shall be outlined that this second goal was found to be relevant

after performing some tests with the software and empirically verifying that an additional set of boundary conditions should be tested in order to seek a solution for the identified problem. This aspect is further explored in section 3.4.2 and also in appropriate subsequent chapters of the present work.

The work of Rosetti et al. [12] was found to be a valuable reference for the selection of boundary conditions. In [12] the authors delved on some of the shortcomings of selecting a rectangular domain for the analysis of a forced-motion cylinder, thus justifying the choice of a circular domain for this case in their analysis. Regarding the choice of boundary conditions, an interesting approach was taken in [12] with respect to the fixed and moving cylinder cases, for which different outlet BC were enforced in both cases.

The next subsections (3.4.1 and 3.4.2) present a detailed analysis of the two sets of boundary conditions selected for application in the test cases.

3.4.1 First set of boundary conditions: BC-DEF

For this case, the specifications found in [6] were found to be a useful reference for the test cases. Therefore, the following set of boundary conditions was selected (the corresponding names used in figure 3.2 are also presented):

- **Inlet:** uniform flow, with specified streamwise velocity vector ($\tilde{\mathbf{V}} = (\mathbf{1}, \mathbf{0}, \mathbf{0})[\mathbf{m/s}]$), specified k and ω, and pressure (p) extrapolated; ***(BCInflow)***

  From an inlet turbulence intensity $I = 1 \times 10^{-2}$, $k = 1.5 \times 10^{-4} U_\infty^2 \; [m^2/s^2]$ is obtained. Furthermore, using $\frac{\nu_t}{\nu} = 1 \times 10^{-4}$, ω can be obtained from $\omega = \frac{k}{\nu_t} \; [1/s]$.

- **Outlet:** specified pressure ($p = 0$), and null streamwise derivatives for the remaining quantities ($\frac{\partial \phi}{\partial x} = 0$); ***(BCPressure)***

- **Top and bottom walls:** specified normal velocity component ($V_y = 0$) and null normal derivatives for the remaining quantities ($\frac{\partial \phi}{\partial y} = 0$); ***(BCSlipwall)***

- **Side walls:** symmetry condition, $V_z = 0$; ***(BCSymmetryPlane)***

- **Cylinder wall:** no-slip and impermeability boundary condition, with all velocity components set to be equal to the wall velocity, and the normal pressure derivative equal to zero. No wall functions were used. ***(BCWall)***

3.4.2 Second set of boundary conditions: BC-MVG

In the simulations concerning the use of a moving grid setup, the same choice of boundary conditions specified for the deforming grid were originally applied. Nevertheless, after performing the simulations according to this setup, artificial pressure oscillations were observed, which motivated a second choice of boundary conditions. Namely, at the outlet surface, the streamwise derivatives of all dependent variables were set to zero ($\frac{\partial \phi}{\partial x} = 0$), corresponding to the ***BCOutflow*** designation in figure 3.3. At the top and bottom walls the pressure was specified to be zero (in order to avoid free pressure values in the

direction of motion of the cylinder), with null normal derivatives for the remaining quantities ($\frac{\partial \phi}{\partial y} = 0$), corresponding to the ***BCPressure*** designation in figure 3.3. The remaining boundary conditions were maintained with respect to the BC-DEF setup.

Figures 3.2 and 3.3 illustrate both the computational domain dimensions and the two sets of boundary conditions analysed.

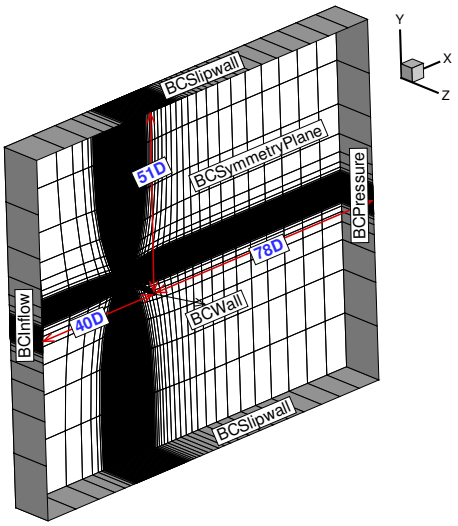

Figure 3.2: **BC-DEF** set of boundary conditions and computational domain dimensions.

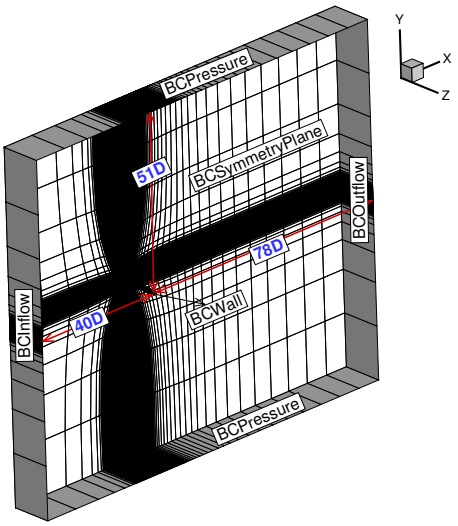

Figure 3.3: **BC-MVG** set of boundary conditions and computational domain dimensions.

3.5 Modelling error assessment

In order to appropriately assess the modelling error in the obtained numerical results, a reference publication [30] that extensively analysed the behaviour of cylinders when subjected to external excitation (imposed motion) was selected. Gopalkrishnan [30] focused on the measurement of the vortex-induced lift and drag forces acting on circular cylinders, when subjected to sinusoidal and amplitude-modulated oscillations. Additionally, the research work of Gopalkrishnan [30] was also used for validation of the results obtained by Rosetti et al. [12], which allowed a better coherence in the comparison of the results of this investigation with the two aforementioned sources.

Chapter 4

Solution Procedure

4.1 Software *ReFRESCO*

The 2.5 version of the *ReFRESCO* software was used in all the computations performed in the present work. As defined in the official website [31], "*ReFRESCO* is a viscous-flow CFD code that solves multiphase (unsteady) incompressible flows using the Navier-Stokes equations, complemented with turbulence models, cavitation models and volume-fraction transport equations for different phases. The equations are discretised using a finite-volume approach with cell-centered collocated variables, in strong-conservation form, and a pressure-correction equation based on the SIMPLE algorithm is used to ensure mass conservation. Time integration is performed implicitly with first or second-order backward schemes. At each implicit time step, the non-linear system for velocity and pressure is linearised with Picard's method and either a segregated or coupled approach is used. In the latter, the coupled linear system is solved with a matrix-free Krylov subspace method using a SIMPLE-type preconditioner. A segregated approach is always adopted for the solution of all other transport equations. The implementation is face-based, which permits grids with elements consisting of an arbitrary number of faces (hexahedrals, tetrahedrals, prisms, pyramids, etc.), and if needed h-refinement (hanging nodes)".

4.2 Numerical Model

When performing a CFD calculation using a general software, a fundamental aspect that should be dealt with at the earliest stages of the study concerns the numerical setup used for the transport equations (in the present case, momentum, pressure, and turbulence, since there is no modelling of transition - that is, the turbulence model is supposed to handle transition). Some of the details that should be carefully analysed when performing the implementation include: [8].

- **The linear equation solver and the mass-momentum coupling solver.** As previously mentioned, all three transport equations in every simulation (momentum, pressure and turbulence) are solved in the form $A\phi = RHS$, being A the left-hand side matrix, ϕ the solved variable (or vector) and RHS the right-hand side vector of the equation. Consequently, a systematic procedure needs

to be selected to compute the solution of each linear equation: the *REFRESCO* software employs a PETSc (*Portable Extensible Toolkit for Scientific Computation*) solver [32], which is a set of routines used for the numerical solution of partial differential equations on high-performance computers. Namely, PETSc provides routines for parallel matrix and vector assembly, which are highly desirable mechanisms in parallel application codes. Furthermore, another procedure is needed to perform the coupling between the linear systems corresponding to the momentum and the mass (pressure) equation.

- **The convergence tolerance.** In each timestep, the solution to each one of the linear equations needs to be computed to a certain precision, which is specified in this parameter.

- **The relaxation procedure.** The equations being solved all have an initial guess for the solution, which is updated as the simulation proceeds. It is possible to change the amount by which the solution is updated **(explicit under relaxation procedure)**. Additionally, each of the linear equations being solved has a certain "stiffness" associated with matrix A, which needs to be controlled (by increasing the matrix diagonal and the RHS) to ensure that the numerical scheme implemented is capable of yielding a solution **(implicit under relaxation procedure)**.

Essentially, the **explicit** under relaxation factor, α_{exp} is used to weigh the contribution of the solution at a previous point, meaning:

$$\phi^{n+1} = \phi^n + \alpha_{exp}(\phi^{n+1^*} - \phi^n) \tag{4.1}$$

in which ϕ^{n+1^*} is the predicted solution at the new non-linear iteration, ϕ^{n+1} is the used solution at the new non-linear iteration, and ϕ^n is the old solution at the previous iteration. Ideally, the explicit under relaxation factor should be as high as possible for faster convergence (provided that the scheme is still stable). It was empirically determined that a factor of **0.8** was appropriate for the momentum equation and a factor of **0.75** was suitable for the turbulence equation. Finally, an explicit under relaxation factor of **0.4** was selected for the pressure (Poisson) equation.

Concerning the **implicit** under relaxation factor, α_{imp}, the left-hand side matrix's (A) diagonal and the RHS of each linear equation being solved are modified (increased) according to:

$$\left(A_{ij} + \left(\frac{A_{ii}}{\alpha_{imp}} - A_{ii}\right)\right)\phi_j^n = RHS_i + \left(\frac{A_{ii}}{\alpha_{imp}} - A_{ii}\right)\phi_j^{n-1} \tag{4.2}$$

Equation 4.2 applies to the non linear problem at each timestep. The software *ReFRESCO* offers the possibility to select a minimum and maximum implicit relaxation factor, along with the number of iterations over which the minimum factor should be increased until it reaches the maximum selected values. Convergence is known to be quicker for high implicit relaxation factors (in the limit, a relaxation factor of 1 would be ideal). Lower implicit relaxation factors yield slower convergence,

but presumably more stable. After a few attempts, it was empirically determined that a value of **0.9** would be appropriate for both the minimum and maximum implicit relaxation factors, for both momentum and turbulence equations.

- **The convective fluxes' discretisation**. Both the momentum and turbulence equations comprise convective terms, and the discretisation scheme employed should also be carefully analysed at early stages. *ReFRESCO* offers several schemes for this purpose. In the present case, the **LIMITED QUICK** scheme (QUICK scheme with a flux limiter) was employed for the convective flux discretisation in the momentum equation, and a **first order upwind** scheme was employed for the same purpose in the turbulence equation.

- **The time integration scheme**. The time integration was performed using an implicit three-time level (2nd order) scheme for all equations, except for turbulence. In this case a first order scheme had to be employed, for robustness purposes.

4.3 Grids

The grids used in this investigation were obtained using the *Grid Generation Tools for Structured Grids* [33]. Taking into account the simplicity of the cylindrical body being analysed, a 2D grid was first generated (to be used in the 2D cases), followed by an extrusion with a given number of cells in the z direction of the domain, in order to produce the 3D grids.

The structured grids generated for the simulations followed a multi-block approach, with different regions in the computational domain, in order to better capture the features of the flow. As displayed in figure 4.1, the grid is symmetric with respect to the x axis and therefore only the part of the grid with positive y coordinates is presented.

The grid blocks were designed in order to appropriately capture the near wall and near wake region of the cylinder. Consequently, a near-wall circular region (with a **3.5D** radius) was used, and the near wake region was extended to a length of **25D**. This strategy allowed a good capturing of the flow features in these zones (which comprised a greater number of grid points), without unnecessarily overloading the remaining blocks with a significant number of cells.

In order to be able to later provide an estimation of the discretisation error (through a grid refinement study), several geometrically similar grids were generated, with a different number of points placed on the surface of the cylinder. Table 4.1 displays this information for all the used grids, along with the grid refinement ratio (h_i/h_1) and the total number of cells. The values indicated under the column "grid name" specify the number of points placed per each sector of 45° on the surface of the cylinder; therefore, the total number of points on the whole surface is obtained through a multiplication by 8.

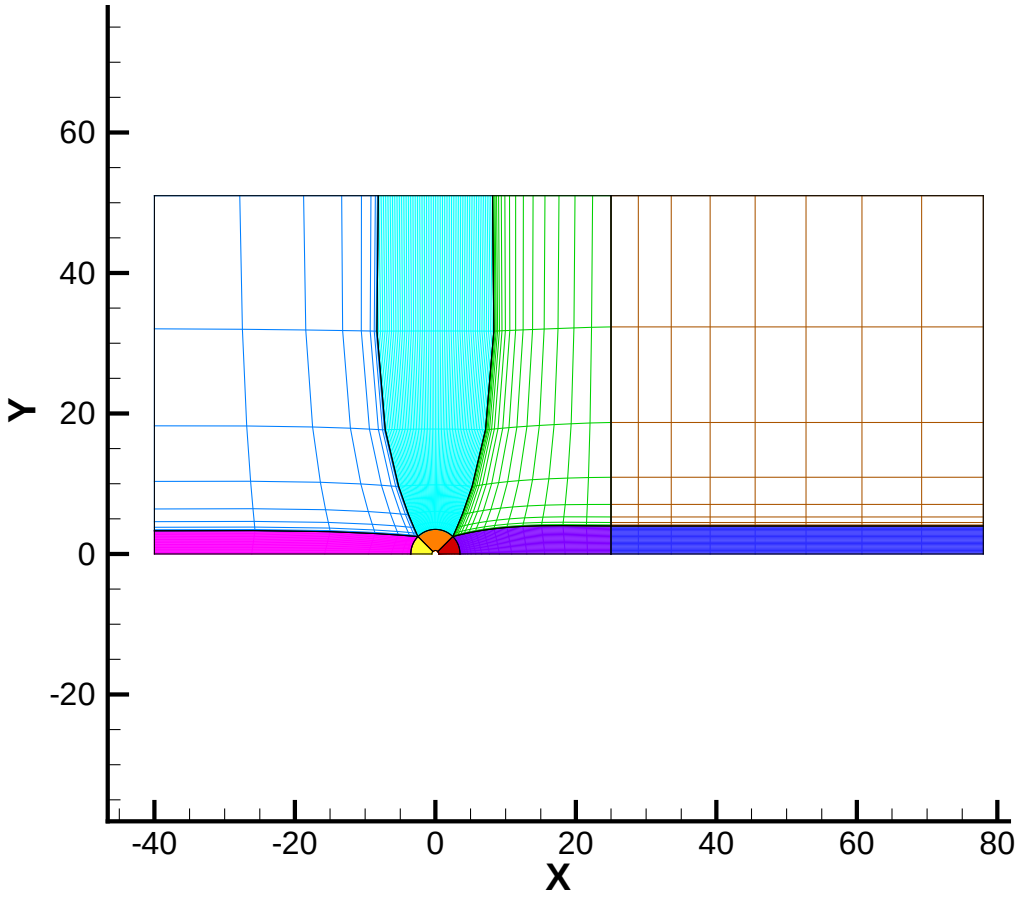

Figure 4.1: Details of the blocks used in the structured grid. Due to symmetry with respect to the x axis, only half of the whole computational domain (figure 3.1) is presented.

Grid name	(h_i/h_1)	Number of points on the surface of the cylinder	Total number of elements
Grid 40	1.6	$40 \times 8 = 320$	18400
Grid 48	$1.(3)$	$48 \times 8 = 384$	26496
Grid 56	$1.14(285714)$	$56 \times 8 = 448$	36064
Grid 64	1	$64 \times 8 = 512$	47104
Grid 80	0.8	$80 \times 8 = 640$	73600
Grid 96	$0.(6)$	$96 \times 8 = 768$	105984
Grid 112	$0.(571428)$	$112 \times 8 = 896$	144256

Table 4.1: Grid refinement ratios, number of points used on the surface of the cylinder for each of the generated grids, and total number of elements in each of the grids.

It shall be recalled that, whenever a RANS approach is used, there are essentially two possibilities for determining the shear stress at a wall. [34] The first option is the use of empirically determined wall functions, which model the near wall behaviour. When adopting this approach, the first cell center needs to be placed in the log-law region of the boundary layer in order to ensure the accuracy of the results.

The use of wall functions is mostly appropriate for applications involving high Reynolds numbers, and when there is no flow separation.

The second possible approach (used in the present study) consists in resolving all the viscosity affected region down to the wall (using the selected turbulence model). This option is usually suitable for low Reynolds numbers applications (as is the present case), and naturally requires the placement of the first cell center in the viscous sublayer. This region is defined with the non-dimensional wall distance y^+ being lower than 5, and in practical CFD applications this value is commonly required to be lower than 1 ($y^+ < 1$).

After generating the grids, it was necessary to run a preliminary simulation in order to appropriately tune the y^+ parameter at the cylinder wall. Grid 64 was chosen as a reference grid for this test (the y^+ maximum value ranged between 0.5 and 0.6, whereas the average value was comprised between 0.2 and 0.3, depending on the test case). Finally, a verification was performed for the remaining generated grids in order to ensure $y^+ < 1$ in all cases.

Figure 4.2 displays in detail the sectors in the surface and the connection between the grid blocks in the region closer to the cylinder.

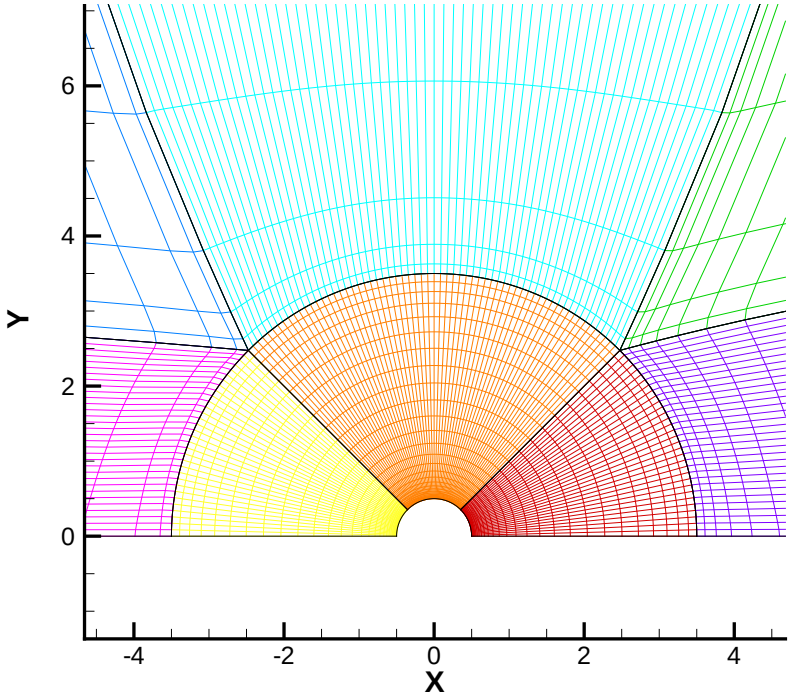

Figure 4.2: Details of the blocks used in the structured grid.

4.4 Mesh deformation and moving mesh algorithms

A fundamental part of the present study focused on the use of two distinct deforming grid methods when performing the moving cylinder calculations. It shall be outlined that, in spite of a widespread use of mesh deformation algorithms for scientific computation purposes, the canonical case of the cylinder flow

justifies a clear, direct comparison between the results yielded by the two selected methods (available on the software *ReFRESCO*).

Analysing the group of mesh deformation methods, point-by-point schemes [35] form a category of methods which rely solely on the interpolation of the imposed boundary displacements and do not require any mesh connectivity information. The Delaunay Graph Mapping (DGM) method, [35] the Radial Basis Function (RBF) interpolation method and the Inverse Distance Weighting (IDW) interpolation method are examples of techniques that fall into this category.

Using a moving grid method is an alternative approach that can be used for the moving cylinder test case. It essentially consists in displacing the grid cells according to the imposed motion on the object, without enforcing fixed boundaries on the computational domain. This procedure was also employed in the present work, in order to provide additional data to be compared with the results obtained through the use of the two mesh deformation algorithms. It shall be recalled that the use of a moving grid approach implied/motivated the definition of a new set of boundary conditions, as previously explained in subsection 3.4.2.

4.5 Deforming grids: Radial Basis Functions

This dynamic method relies on the application of radial basis functions (functions whose value depends solely on the distance from the origin or from a predefined reference point) to update the mesh as the numerical simulation proceeds. Therefore, the displacements at the domain points are computed through a weighted sum of radial basis functions. A system of equations only involving the boundary nodes is solved in order to obtain the RBF weights, and at a later stage, the displacements corresponding to internal nodes are assessed [35].

The RBF method has a high computational cost: solution time scales with $O(N_b^3)$, being N_b the number of nodes on the boundary of the domain. However, it is a robust algorithm resulting in high quality deformed meshes [35].

Radial Basis Functions are often employed in fluid-structure interaction problems, in order to transfer the displacements known at the boundary of the structural/solid body mesh to the aerodynamic/fluid mesh [36]. The interpolation function - which gives the displacements of the nodes in the whole domain - can be stated as a sum of basis functions: [36]

$$s(\mathbf{x}) = \sum_{j=1}^{n_b} \alpha_j \phi(\left\| \mathbf{x} - \mathbf{x_{b_j}} \right\|) + p(\mathbf{x}) \tag{4.3}$$

In equation 4.3, $\mathbf{x_{b_j}}$ is the vector of coordinates of the cell centers in which the displacements are known (at the fluid-structure interface/boundary), $\mathbf{p}$ is a polynomial and $\mathbf{n_b}$ is the number of boundary nodes, and ϕ is a given basis function whose argument concerns the Euclidean distance between any given node and a boundary node. The coefficients $\alpha_\mathbf{j}$ and the polynomial $\mathbf{p}$ can be found with two additional conditions:

- The interpolation function evaluated at the boundary points needs to yield the boundary nodes'

displacement;

$$s(\mathbf{x_{b_j}}) = \mathbf{d_{b_j}} \tag{4.4}$$

- The following condition

$$\sum_{j=1}^{n_b} \alpha_j q(\mathbf{x_{b_j}}) = 0 \tag{4.5}$$

needs to be verified for all polynomials $\mathbf{q}$ with a degree less or equal than that of polynomial $\mathbf{p}$. However, the implementation of the interpolation function in *ReFRESCO* [37] follows the guidelines found in [38], in which the polynomial term $\mathbf{p}$ is suppressed. In this publication it was found that appending polynomial terms to the interpolation function resulted in undesirable motion of the far-field boundary (in spite of the advantage of allowing exact recovery of rotations - which are not considered in the present study). Consequently, the system underlying in equation 4.3 suffices to determine the unknown coefficients $\alpha_\mathbf{j}$. The computational details of this implementation can be found in [38].

Once the aforementioned coefficients are determined, the displacements at the interior nodes can be found through the evaluation of the interpolation function at those points:

$$\mathbf{d_{in_j}} = s(\mathbf{x_{in_j}}) \tag{4.6}$$

This formulation outlines the fact that within the computational domain, each grid point can be individually moved (requiring only its coordinates and the use of the interpolation function) without the need of any mesh connectivity information. Furthermore, the system of equations in mesh-connectivity schemes has dimension of $O(n_{in})^2$, (being n_{in} the total number of mesh points) whereas the system to be solved in this case (using only the information concerning the nodes individually) has dimension of $O(n_b)^2$, (being n_b the number of boundary points). Since the total number of grid points is usually a dimension higher than the number of boundary points, this approach represents considerable computation savings and simplifies the implementation in 3D cases because no spatial connectivity information is required [36].

The choice of the basis function ϕ to be used in the interpolation strongly depends on the desired goals regarding the problem being numerically analysed. Mainly, radial basis functions can have either **compact, global or local support:**

- Functions with **compact support** have a non-zero value in a limited region within the computational domain (usually defined as a **support radius)**) and are zero outside this region. Therefore, the compact support implies that mainly the grid nodes inside the support radius will be affected by the movement of this region. As expected, higher values of the support radius generally yield less distorted grids, and, according to [36], more accurate solutions (at a natural cost of matrix systems which are more dense), whereas low values of the support radius triumph in computational

efficiency at a cost of lower quality grids. The implementation of RBF interpolation in the software *ReFRESCO* comprises compact basis functions and therefore a support radius is required in the input file in order to run the simulation. Considerations concerning the relevance of this parameter are further explored in appendix A.

- Functions with **global support** do not have a precisely defined region of influence, and consequently never reach a null value anywhere in the domain (thus covering the whole interpolation space). Additionally, according to [38], their value increases with increasing distance to the origin.

- Functions with **local support** share the same properties mentioned for the global support function, nevertheless with a decrease in their value with increasing distance from the origin. [38]

4.5.1 Implementation

As previously mentioned, the solution of the system of equations expressed in equation 4.3 allows the determination of the unknown coefficients $\alpha_{\mathbf{j}}$, which are then used to compute the value of the interpolation function at the remaining points of the domain, yielding the displacement at these points. According to the information found in [37], the solution of the system is found using PETSc' (*Portable Extensible Toolkit for Scientific Computation*) [32] preconditioned conjugate gradient iterative method, using block Jacobi preconditioning. The details of this implementation are omitted as they were found to be beyond the scope of the present work.

Nevertheless, the information found in [38] clearly exposes some of the cumbersome computational costs of the RBF method: the time and memory needed to solve the interpolation scale with N_{sp}^3 and N_{sp}^2 respectively, whereas the mesh update scales with $N_{sp} \times N_{vp}$, being N_{sp} the number of surface points and N_{vp} the number of volume points.

One of the options to reduce this cost consists in selecting a subset of the boundary points (the points on the surface of the moving body) that accurately represents the motion, and then correcting the remaining surface points while ensuring a good mesh quality in the first layer of cells away from the surface. This then allows a smooth propagation of the correction for the remaining volume points (cell layers away from the surface), which also preserves mesh quality. The underlying ideas in this procedure point to the use of a **greedy algorithm**, which brings considerable advantages when coupled with an RBF interpolation approach. [38]

4.5.2 Greedy algorithms

When applied to a set of data points, and controlled by a previously defined error signal, a greedy algorithm locates the largest existing error and selects it for correction, no matter the cost implicated in this decision [38]. In the context of RBF interpolation, a greedy algorithm limits the number of boundary points included in the system to be solved. According to the implementation details found in [39], the selection of the limited set of boundary points is done in an iterative manner:

- The boundary point with the largest displacement is selected and the interpolation coefficient is set to zero for this specific point;
- A hybrid version of the **greedy one point algorithm** and **greedy full point algorithm** is applied;
- The iterative process is interrupted when the interpolation error drops below a certain threshold.

The **greedy one point algorithm** [38] scans all the boundary points and identifies the one with the largest interpolation error (that is, the largest difference between the interpolation value and the prescribed displacement). This point is then added to the set (if it has not been used yet), and a correction to the interpolation coefficient in this point is computed. Lastly, the interpolation is corrected for all boundary nodes. [39]

The **greedy full point algorithm** [38] is partially similar to the greedy one point algorithm; however, after selection and addition of the largest error point to the data set, the interpolation coefficients are computed for **all** the points present in the data set, and then the displacement at all boundary nodes is computed by interpolation. [39]

The **hybrid version** of the two aforementioned algorithms is known to yield the most efficient performance [39]. In this scenario, a new point is added at each iteration, using one of the two algorithms, and the process ends with the second algorithm (greedy full point). Once every *n* cycles, the one point algorithm is used; in the remaining cycles, the full point algorithm is chosen. This hybrid method combines the advantages of both algorithms: while with the second algorithm the interpolation error at the boundary reduces faster (which comes at a higher computational cost since in each iteration a system of equations has to be solved), the first algorithm can be used every *n-th* cycle to increase speed.

4.5.3 RBF method and structured grids

Previous authors [36] [40] [41] claimed that the use of RBFs for displacement interpolation was found to be computationally very expensive for structured grids, and therefore suggested the use of more efficient methods for the structured part of multi-block grids, complemented with the use of RBFs for the computation of block boundaries' displacements. However, the software *ReFRESCO* solely has two deforming techniques (IDW and RBF), which were therefore applied to the present problem (even though the domain was discretised using a multi-block structured grid).

4.6 Deforming grids: Inverse Distance Weighting

This grid-deforming algorithm roots on the use of the inverse distance weighting method (which allows interpolation on functions of more than one variable) to create translation matrices between the points of the original mesh and the deformed mesh. This deforming method is widely used in CFD simulations and several publications (whose focus falls beyond the scope of the present work) have sought to present modifications in order to improve both efficiency (since during the deformation process the mesh needs

to be recomputed several times) and mesh quality (since poor mesh quality can significantly affect the accuracy of the solution). [42]

The implementation of the IDW technique on the software *ReFRESCO* follows the underlying theory present in [43]. When using the IDW method, there is no need to solve a system of equations (contrarily to the RBF technique), and therefore the displacements at the internal grid points are computed using the displacements at the boundary nodes, through an interpolation surface, $w(\mathbf{x})$:

$$w(\mathbf{x}) = \frac{\sum_{i=1}^{n_b} v_i \phi(r_i)}{\sum_{i=1}^{n_b} \phi(r_i)} \tag{4.7}$$

In equation 4.7, $\mathbf{v_i}$ represents the displacement at each boundary node i, and ϕ is a weighting function evaluated at $\mathbf{r_i} = \left\| \mathbf{x} - \mathbf{x_{b_i}} \right\|$, that is, the distance between $\mathbf{x}$ and boundary node $\mathbf{x_{b_i}}$ [37]. The weighting function ϕ is defined as:

$$\phi(r) = r^{-c} \tag{4.8}$$

with $c > 1$ being a power parameter in order for the weighting function to be smooth (and therefore differentiable). In [43] the mesh deformation algorithm separated the treatment of this parameter both for dynamic and static boundary nodes, as well as for translations and rotations. The the details of this implementation are herein omitted.

Figures 4.3 and 4.4 display the deformed grids with each of the two methods (RBF and IDW) when compared to the undeformed/original grid (used in the moving grid approach). A clear difference between the deformed grid with RBF and the original grid is visible in the cylinder vicinity (figure 4.3) whereas the difference between the grid deformed with the IDW method and the original one is almost imperceptible near the cylinder wall (figure 4.4), becoming only evident at a greater distance from the cylinder.

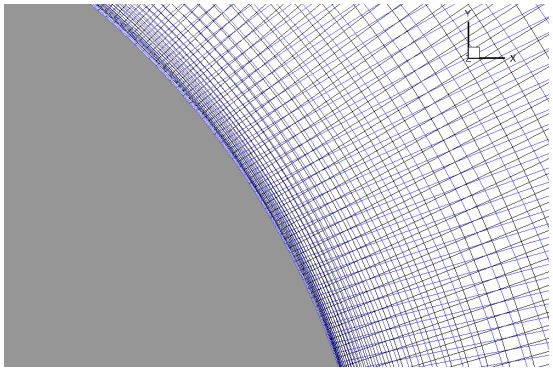

Figure 4.3: Deformed grid at the point of maximum C_L, for the RBF (blue) MVG (black) methods.

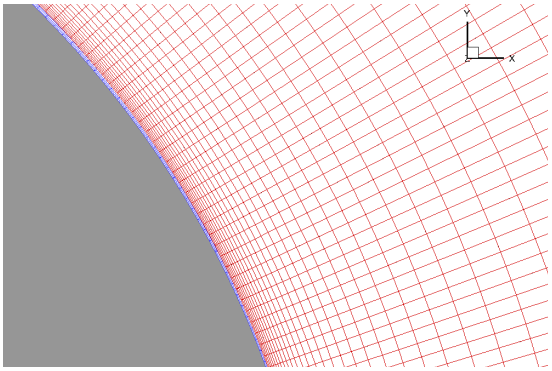

Figure 4.4: Deformed grid at the point of maximum C_L, for the IDW (red) MVG (black) methods.

The total computational time associated with each of the methods was also analysed. Taking as an example a (2D) simulation for the IDW, RBF and MVG setups (using reference grid 64), it was identified that the moving grid case (MVG) required the largest amount of CPU time (approximately 15h), followed by the RBF method (with 97% of that reference time) and by the IDW method (with approximately 96% of

the moving grid reference time). However, for the two deforming grid techniques, the deformation was only computed in the first cycle with the desired amplitude, and the grids were stored. Therefore, the deforming grid techniques present the disadvantage of requiring larger amounts of disk space to store the grid deformation at each timestep of the initial cycle.

4.7 Test Cases

All the cases evaluated in the course of the present investigation comprised **one** cylinder placed in a computational domain (whose characteristics were previously described in section 3.3) with two different sets of boundary conditions (stated in subsections 3.4.1 and 3.4.2), at a Reynolds number of $Re = 10,000$. The choice of this parameter followed the aim of backing up the numerical results obtained having as a reference the work of Rosetti et al. [12] and later performing a validation exercise following the experimental results available in [30].

4.7.1 2D Fixed Cylinder

Regarding the first test case (2D fixed cylinder), the simulations were performed for the two sets of boundary conditions imposed on the selected domain. This test case allowed an analysis of the isolated effect of the choice of boundary conditions on the obtained results and a valuable standpoint for a later comparison between the numerical and modelling performance of RANS for fixed and moving cylinders.

4.7.2 2D Moving Cylinder

The two-dimensional moving cylinder cases aimed at further deepening the analysis carried out in the present work. In this part the effect of **imposed motion** (sinusoidal excitation) in the transverse direction was evaluated. As previously stated, the 2D driven motion test cases followed literature data found in [12] [30], and therefore a sinusoidal motion was imposed to the cylinder:

$$y(t) = Asin(\omega_i t) \tag{4.9}$$

being $y(t)$ the transverse coordinate of the cylinder center over time, A the amplitude of the prescribed periodic motion and ω_i the dimensional frequency of the movement. In order to allow comparison with previously obtained data [12] [30], the non-dimensional amplitude $\mathbf{A/D = 0.3}$ was selected, and a range of reduced velocities (which specify the non-dimensional motion period) $\mathbf{U_R = UT_i/D}$ from 3 to 10 was chosen. Following the study of the boundary conditions' effect (on the fixed case), the 2D moving test case also focused on the effect of the boundary conditions, complemented with a study of the influence of several moving/deforming grid techniques on the results. Following the previous numerical work found in [12] and the experimental data available in [30], the following approach was adopted:

- Analysis of the test cases using a **moving grid** method, in order to reproduce the work carried out by [12] and analyse potential differences found, and analysis of the test cases using two different

deforming grid methods, in order to assess the validity of using moving grid methods in numerical setups [12] reproducing experimental results [30] in finite tanks;

- Analysis of the numerical convergence properties of the aforementioned methods, through an assessment of the statistical, iterative and discretisation components of the error.

4.7.3 3D Moving Cylinder

Additional three dimensional test cases were studied (imposed motion) in order to perform a comparison with the corresponding 2D results, and therefore these test cases followed the same principles used in the 2D analysis (same sets of boundary conditions and domain size, same non-dimensional amplitude of motion and range of reduced velocities). Naturally, these exercises were restricted to a smaller number of flow conditions than the 2D study; nonetheless, one example of the influence of the cylinder aspect ratio (L/D) is presented.

4.8 Quantities of interest

After running the simulations for any of the selected test cases, it was necessary to design a few post-processing routines in order to extract the desired quantities of interest. The routines were written in *FORTRAN 90* and essentially allowed:

- Obtaining the force coefficients (C_L and C_D) time history from the total forces time history in the x and y directions (which is an output of the simulations) and computing statistical quantities of interest, such as the minimum, maximum, average and *rms* values of the previously obtained force coefficients;

- Performing a FFT (*Fast Fourier Transform*) of the time series in order to evaluate the frequency content of the obtained signals (this was later used for the statistical convergence study, which will be further explored in chapter 5).

The drag and lift coefficient were computed from the total forces in the x and y directions, respectively, according to:

$$C_D = \frac{F_x}{\frac{1}{2}\rho U_\infty^2 DL} \quad , \quad C_L = \frac{F_y}{\frac{1}{2}\rho U_\infty^2 DL} \tag{4.10}$$

where L, the cylinder length, is irrelevant for the 2D situations. The quantities of interest analysed in the several test cases comprised the minimum, maximum, average and *rms* values of the force coefficients in both x and y directions. For the sake of brevity, only the results concerning the CD_{avg} and the CL_{rms} will be detailed in the present document, since they were considered to be representative of the overall trends observed for the remaining computed quantities.

Chapter 5

Numerical Convergence

5.1 General considerations

The main objective of the numerical convergence studies (developed in detail for the 2D cases) was the comparison of the fixed and forced motion test cases with respect to the behaviour of the numerical error. Naturally, as in every simulation of an unsteady problem, there are essentially three components of the numerical error which need to be properly assessed and accounted for:

- Statistical error;
- Iterative error;
- Discretisation error (in space and time).

The first two components mentioned are usually addressed first, since the discretisation error is considered to be dominant. Thus, the iterative and statistical error should be reduced to a level of "two to three orders of magnitude lower than the discretisation error in order not to disturb the estimation of the numerical error" [44].

A fundamental aspect that had to be taken into account when performing the statistical and iterative convergence studies was the range of grids selected for each of the fixed and imposed motion cases. In fact, it was found that, in the imposed motion cases, the frequency content revealed by the time history of the forces was not as expected for all the generated grids. Therefore, before quantifying the statistical and iterative components of the error, an aspect that was found to deserve attention at an early stage was the analysis of the frequency content displayed by the time traces of the force coefficients. As a result, it was found relevant to perform a **FFT** *(Fast Fourier Transform)* analysis, for the solutions obtained with all the grids generated in the course of this study, in order to evaluate if significant differences were found in the frequency spectrum.

Figures 5.1 and 5.2 display the obtained FFT for the reference grid **(grid 64)**, for the fixed case (using the BC-MVG set of boundary conditions) and for one of the imposed motion cases ($U_R = 3.0$, using the RBF technique, also with the BC-MVG set of boundary conditions). A clear peak is identified in the fixed case, corresponding to the natural frequency associated with the vortex shedding phenomenon. In the

imposed motion case the first peak - in spite of also being associated with the natural vortex shedding - displays a slight shift in frequency, with respect to the fixed case. The second peak (with greater intensity) clearly represents the excitation frequency of the imposed motion ($f = 1/U_R$).

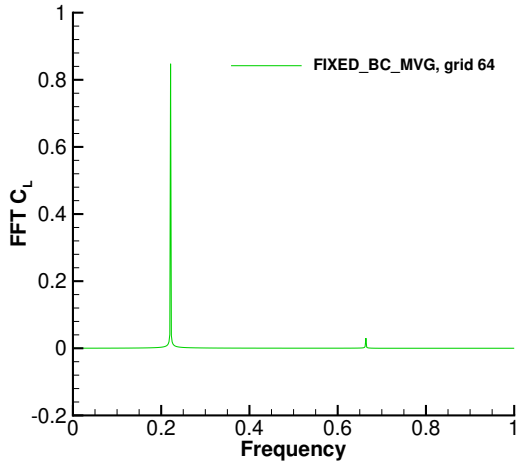

Figure 5.1: Frequency content of the C_L signal, for the fixed case, (FIXED-BC-MVG setup), using an iterative tolerance of 5×10^{-6}. Result obtained for **grid 64**.

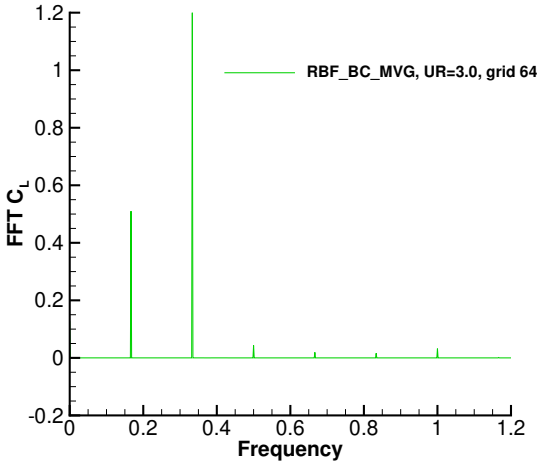

Figure 5.2: Frequency content of the C_L signal, for the reduced velocity $U_R = 3.0$, (RBF-BC-MVG setup), using an iterative tolerance of 5×10^{-6}. Result obtained for **grid 64**.

When refining the grid - from **grid 64** to **grid 80** - it was observed that the frequency content displayed by the FFT changed. While for the fixed the case the difference was minimal (slight broadening of the peak corresponding to the natural vortex shedding phenomenon, figure 5.3), the imposed motion case revealed the appearance of low frequency content in the signal (figure 5.4). This was confirmed by an analysis of the time history of the force coefficients, which showed the appearance of additional low frequencies, both in moving and deforming grid setups (figures 5.5 to 5.8).

Furthermore, in order to analyse if the selected timestep for the simulations was appropriate, a brief test was performed for $U_R = 3.0$, in **grid 80**, using a timestep three times smaller than the originally chosen one. Figure 5.9 displays this comparison, outlining the appearance of additional low frequency content. This discussion will be further detailed in chapter 6.

Figures 5.10 to 5.12 represent the study that was carried out for all the grids used (for the $U_R = 5.0$ test cases), using both a constant $\Delta t_i/\Delta t_1$ and a constant h_i/h_1. It is clear that the influence of changing the grid refinement ratio is preponderant over the influence of changing $\Delta t_i/\Delta t_1$, which justifies the use of a constant Courant number for the grid/time refinement studies. This aspect will also be further detailed in section 5.5.

Naturally, the appearance of the low frequency fluctuations with grid/time refinement questions if the mean flow properties - according to the selected RANS formulation - are correctly being captured. Thus, only the cases that displayed well defined peaks - predictably representing in fact the mean flow frequency content - in the corresponding FFT were selected for the statistical and iterative convergence studies. Table 5.1 identifies the grids for which the obtained frequency spectrum was as expected, both

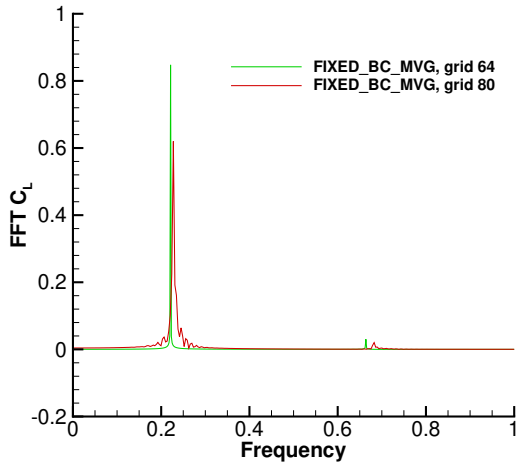

Figure 5.3: Frequency content of the C_L signal, for the fixed case, (FIXED-BC-MVG setup), using an iterative tolerance of 5×10^{-6}. Result obtained for **grid 64** and **grid 80**.

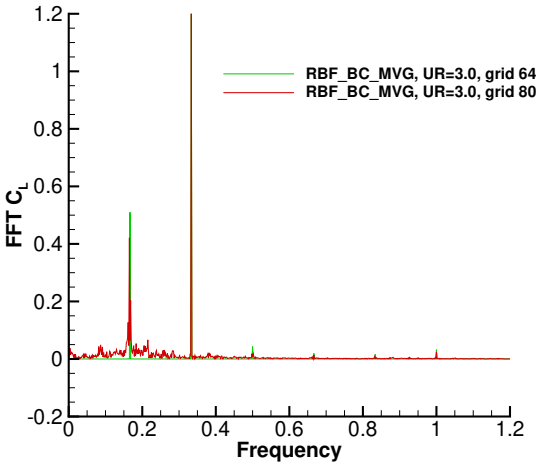

Figure 5.4: Frequency content of the C_L signal, for the reduced velocity $U_R = 3.0$, (RBF-BC-MVG setup), using an iterative tolerance of 5×10^{-6}. Result obtained for **grid 64** and **grid 80**.

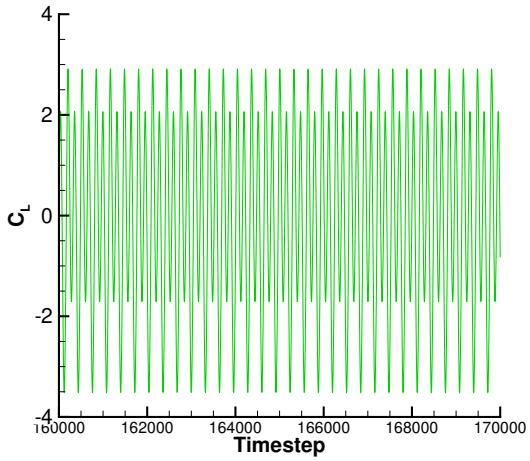

Figure 5.5: Time history of the C_L signal, for the imposed motion case, (RBF-BC-MVG setup), $U_R = 3.0$, using an iterative tolerance of 5×10^{-6}. Result obtained for **grid 64**.

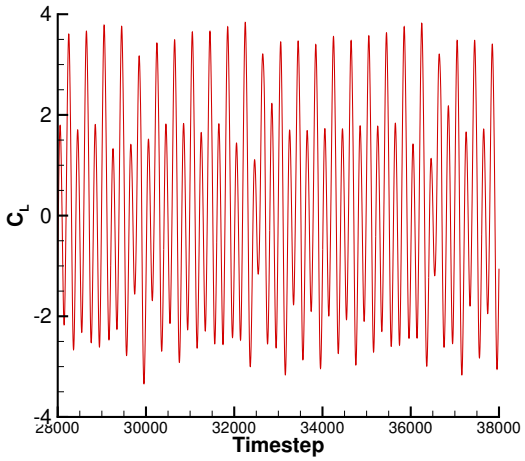

Figure 5.6: Time history of the C_L signal, for the imposed motion case, (RBF-BC-MVG setup), $U_R = 3.0$, using an iterative tolerance of 5×10^{-6}. Result obtained for **grid 80**.

for the fixed and imposed motion setups.

Reduced velocity (U_R)	Grids displaying a solution with frequency content as expected
< 3	None
3	40, 48, 56, 64
5	40, 48, 56, 64
10	40, 48, 56, 64, 80
∞ (Fixed case)	40, 48, 56, 64, 80, 96

Table 5.1: Grids used for the numerical error estimation in the fixed and imposed motion test cases.

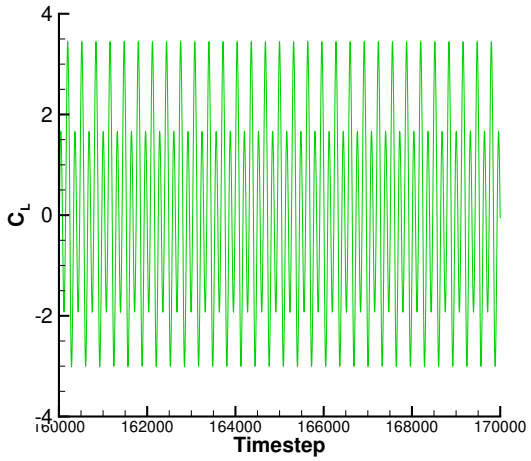

Figure 5.7: Time history of the C_L signal, for the imposed motion case, (MVG-BC-MVG setup), $U_R = 3.0$, using an iterative tolerance of 5×10^{-6}. Result obtained for **grid 64**.

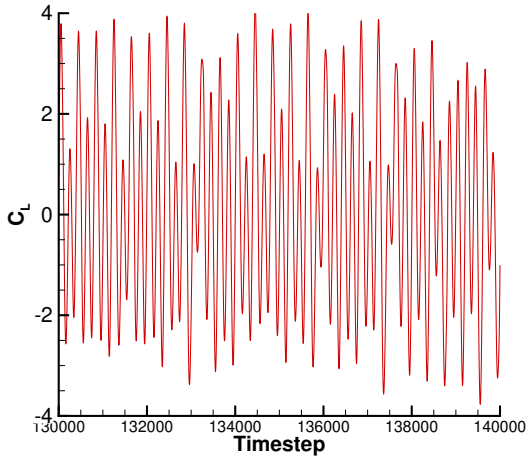

Figure 5.8: Time history of the C_L signal, for the imposed motion case, (MVG-BC-MVG setup), $U_R = 3.0$, using an iterative tolerance of 5×10^{-6}. Result obtained for **grid 80**.

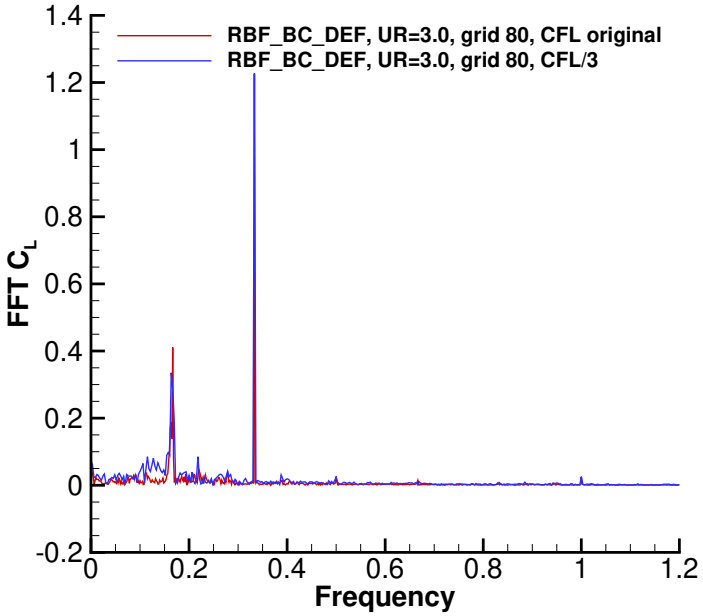

Figure 5.9: Frequency content of the C_L signal, for the RBF-BC-DEF setup, $U_R = 3.0$, in **grid 80**, both for the case with the originally selected timestep and for the case with the timestep reduced to one third of the original value.

Another aspect that had to be taken into account at an early stage - in spite of being further analysed later on, together with an appropriate quantification of the iterative error - was the influence of the iterative tolerance chosen for each simulation in the displayed frequency content of the signals. In fact, it was found that for an iterative tolerance of 5×10^{-3}, in the reference grid (grid 64), the influence of the iterative error had not been eliminated, also leading to the appearance of low frequency content in the signal. However, this behaviour disappeared when lowering the iterative tolerance to 5×10^{-6}. Figure

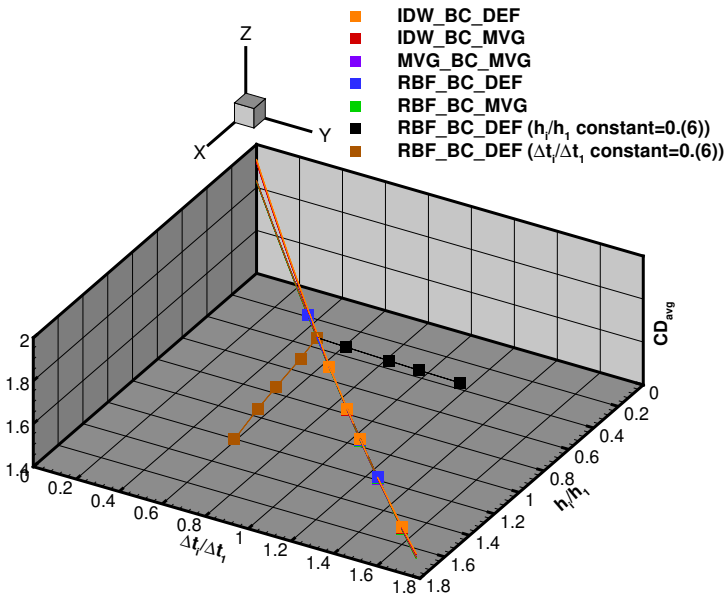

Figure 5.10: CD_{avg} for all the imposed motion setups, $U_R = 5.0$, with $\Delta t_i/\Delta t_1 = h_i/h_1$, with constant $\Delta t_i/\Delta t_1 = 0.(6)$ and constant $h_i/h_1 = 0.(6)$.

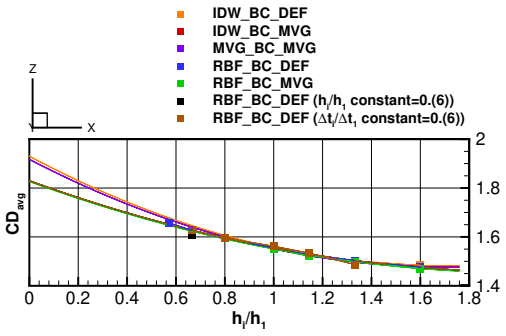

Figure 5.11: CD_{avg} vs. h_i/h_1 view from figure 5.10.

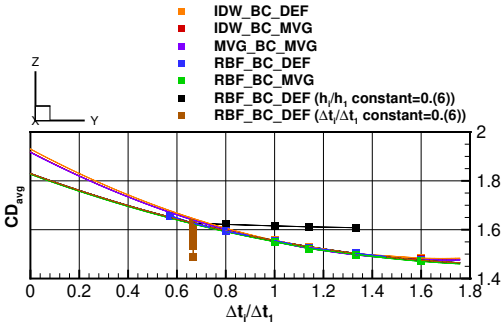

Figure 5.12: CD_{avg} vs. $\Delta t_i/\Delta t_1$ view from figure 5.10.

5.13 displays this behaviour. One could argue that the low frequency peaks displayed when refining the grid (result for grid 80, displayed in figure 5.4) were also caused by an influence of the iterative error. However, simulations using an iterative tolerance as low as 1×10^{-8} were performed for grid 80 without successfully eliminating the aforementioned oscillations, which allowed discarding the influence of the iterative error in this case.

Figure 5.14 displays another aspect that was taken into account at this point of the analysis. In order to verify the influence of the number of cycles used to compute the FFT, three tests were performed using only the last 40, 80 and 200 cycles in the time history of the force coefficients. The tests were performed for $U_R = 10.0$, using the MVG-BC-MVG setup, in the coarsest grid (grid 40). Observing figure 5.14, it can be seen that the only influence in using a larger number of cycles for the computation is the narrowing of the width of the peaks captured, and that no additional peaks are captured when changing

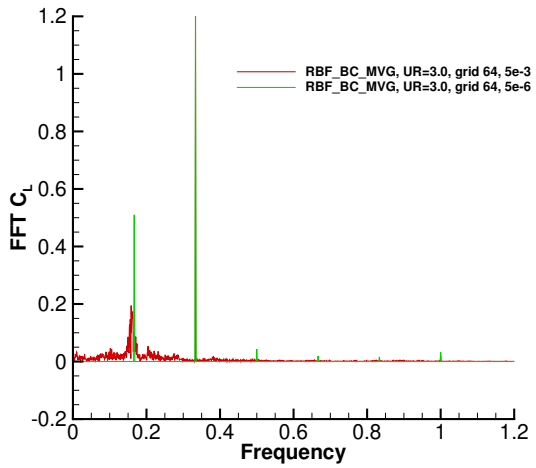

Figure 5.13: Frequency content of the C_L signal, for the reduced velocity $U_R = 3.0$, (RBF-BC-MVG setup), using an iterative tolerance of 5×10^{-3} vs. using an iterative tolerance of 5×10^{-6}. Result obtained for **grid 64**.

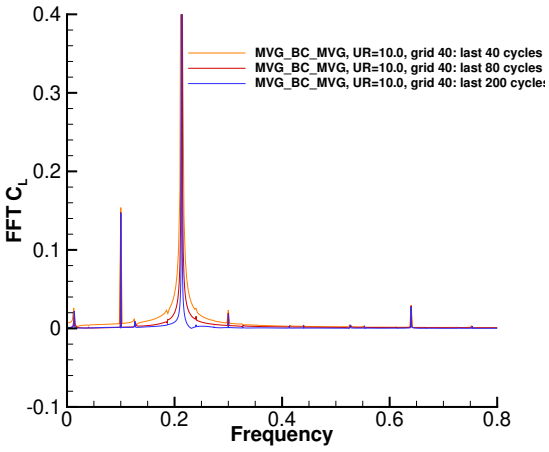

Figure 5.14: Frequency content of the C_L signal, for the reduced velocity $U_R = 10.0$, (MVG-BC-MVG setup), using an iterative tolerance of 5×10^{-6}. Result obtained using the last 40, 80, and 200 cycles when computing the FFT, for **grid 40**.

the number of cycles used. This indicates that the simulations have been run over a sufficient number of cycles (in all three cases) in order to appropriately eliminate potential low frequency content due to the influence of the initial conditions in the first cycles.

5.2 Statistical convergence studies

An important parameter to be verified is the **statistical convergence** of the signal. Taking a broader look at this concept - and overlooking a more mathematical definition [45] - it can be seen as a convergence of some statistical variables of interest (namely, the mean value, the rms value, the maximum or the minimum) over a sufficiently large number of cycles (in a periodic signal).

Concerning a practical approach to the present problem (a supposedly periodic signal with a non-unique frequency content), a possible path to evaluate statistical convergence consists in using **FFT** (*Fast Fourier Transform*) information of the recorded signal in order to compute the statistical variables of interest over a relevant number of cycles, in which the signal is already periodic.

5.2.1 Preliminary analysis

One of the first goals of this investigation consisted in analysing the force coefficients response (both in the flow direction, C_D, and in the transverse direction, C_L) over time, in order to gain some insight regarding the frequency content of the signal.

Regarding the imposed motion cases, it was predictable that the lift and drag force would display more than one frequency in the response, due to the difference between the excitation frequency of the system, related to the reduced velocity, and the vortex shedding frequency, related to the Strouhal

number. In order to better assess the frequency content of the drag and lift forces time traces, a FFT (*Fast Fourier Transform*) was performed for the test case corresponding to the lowest reduced velocity, $U_R = 3.0$.

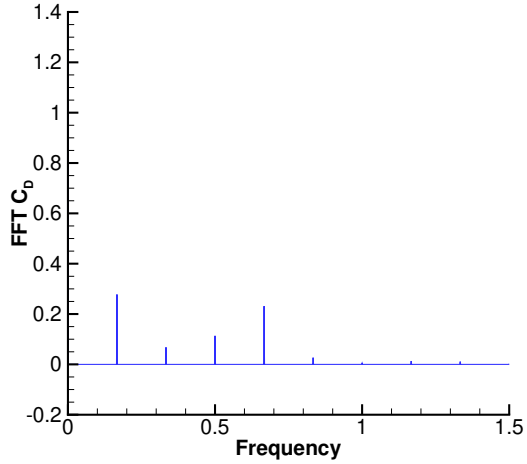

Figure 5.15: Frequency content of the C_D signal, for the reduced velocity $U_R = 3.0$, using an iterative tolerance of 5×10^{-6}.

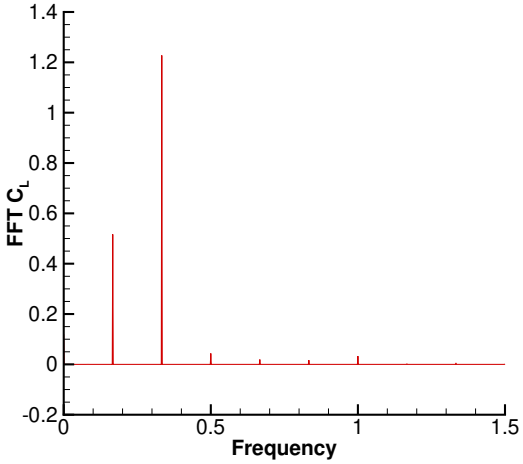

Figure 5.16: Frequency content of the C_L signal, for the reduced velocity $U_R = 3.0$, using an iterative tolerance of 5×10^{-6}.

Analysing figures 5.15 and 5.16, it is clear that a peak is present at a non-dimensional frequency equal to $0.(3)$, for both the C_D and the C_L (second bar counting from the left on the plots). As previously stated, this corresponds to the contribution of the excitation frequency (the reduced velocity $U_R = 3.0$ corresponds precisely to a frequency of $0.(3)$).

Additionally, a frequency corresponding to approximately **half** this value is also present ($f = 0.1(6)$, first bar counting from the left), appearing due to the vortex shedding phenomenon. Since this was the lowest frequency present in both responses, corresponding to half of the external excitation frequency, it was found relevant to compute the quantities of interest over **multiples of two periods of excitation**, in order to qualitatively evaluate the statistical convergence of the signals at an early stage. Therefore, designating as N_{total} the total number of iterations and T the period of excitation, the quantities of interest were computed for the last two periods, four periods, six periods...until a total of sixteen periods, as summarised in the table below (5.2) for the quantities CD_{avg} and CL_{rms}.

Number of cycles considered	CD_{avg}	CL_{rms}
$N_{total} - 2T$	1.4646672167	1.8894659350
$N_{total} - 4T$	1.4646672961	1.8894660093
$N_{total} - 6T$	1.4646671384	1.8894662642
$N_{total} - 8T$	1.4646671323	1.8894661639
$N_{total} - 10T$	1.4646671999	1.8894660979
$N_{total} - 12T$	1.4646672496	1.8894660526
$N_{total} - 14T$	1.4646673001	1.8894659787
$N_{total} - 16T$	1.4646673483	1.8894659604

Table 5.2: CD_{avg} and CL_{rms} computed over a given number of cycles, for $U_R = 3.0$, RBF-BC-DEF setup, using an iterative tolerance of 5×10^{-6}.

Table 5.2 displays (qualitatively) the expected behaviour: in fact, over the selected cycles, the variation in the computed quantities are of the order of magnitude of the chosen iterative tolerance (5×10^{-6}), which indicates that statistical convergence has been achieved.

5.2.2 Statistical uncertainty estimation

In spite of the strategy described in the previous subsection, it is clear that a systematic and reliable procedure is necessary to provide an estimation of the statistical uncertainty associated with the results. In general terms, this uncertainty can be measured as a deviation of the quantities of interest in N samples (cycles) selected from the signal. Consequently, a signal that has become **statistically steady** over a certain number of cycles will necessarily have a lower statistical uncertainty associated. It can therefore be argued that, with this in mind, it is a good practice to ensure that the measured variables of interest have reached a statistically steady state in all the simulations performed. Thus, all simulations (in all test cases) were run for a total of $\mathbf{200}$ **full cycles** in order to ensure this aspect.

After ensuring that the simulations had been run for a sufficient number of timesteps, it was then imperative to implement the aforementioned systematic procedure to estimate the statistical uncertainty. A practical approach to tackle this aspect can be found in [46], which consists on the division of a signal (namely, the time response of the forces acting in the cylinder) into equally-sized segments. This method proved to be quite useful for the present application, since it is possible to record a finite number of full oscillations/cycles of the cylinder in each simulation, being those available for further post-processing.

The first aspect to be settled was the number of samples (N) to be used for the error estimation. Ideally, this number should represent a compromise between low computation time and sufficient accuracy. Furthermore, each of the N samples should contain more than just a single cycle/oscillation of the cylinder movement. Bearing these two requirements in mind, two distinct possibilities were therefore analysed:

- Selecting 10 segments of 4 cycles each, comprising a total of 40 cycles, taken at the end of the simulation **(N=10)**;

- Selecting 25 segments of 4 cycles each, comprising a total of 100 cycles, taken at the end of the simulation **(N=25)**.

A test was performed to timely verify the differences found when selecting each of the two procedures. It was found that the results did not display significant differences (that is, the estimated uncertainty was within the same order of magnitude in corresponding variables, when compared for the two methods), which motivated the selection of the **first option**, due to a better compromise between computation time and accuracy. As a result, for the statistical uncertainty estimation, only the last 40 cycles out of the 200 available from each simulation were used.

The statistical uncertainty can be estimated through the variance (or correspondingly, standard deviation) for each of the variables of interest:

$$s = \sqrt{\frac{\sum_{i=1}^{N}(x_i - m_x)^2}{N-1}} \tag{5.1}$$

Taking into account that equation 5.1 is applied to the previously defined number of segments N, x_i represents the quantity of interest for each one of the N segments, and m_x represents that same quantity for the ensemble of the N segments. For instance, if one is analysing the average value of the drag coefficient (CD_{avg}), then x_i is the average drag coefficient for each segment i out of a total of N, and m_x is the average drag coefficient for all N segments.

The computed value, s, represents the standard deviation of all individual mean values. According to [46], the **uncertainty** associated to each variable of interest is computed as:

$$u_{segment} = \frac{s}{N} \tag{5.2}$$

with N again representing the selected number of segments.

Following this approach, it was found appropriate to select two variables of interest, among all the monitored ones, in order to study the evolution of the statistical error along with the iterative tolerance chosen for each simulation. Consequently, the average drag coefficient (CD_{avg}) was chosen as a representative force coefficient for the x direction, while the root-mean-square (rms) lift coefficient (CL_{rms}) was selected to be the most representative parameter for the y direction (the direction along which the motion was imposed to the cylinder).

The plots presented in figures 5.17 to 5.20 display the evolution of the percentage statistical error (computed according to the methodology that was previously described), for both of the chosen variables, and for both the 2D fixed cases and 2D imposed motion cases (with $U_R = 3.0$).

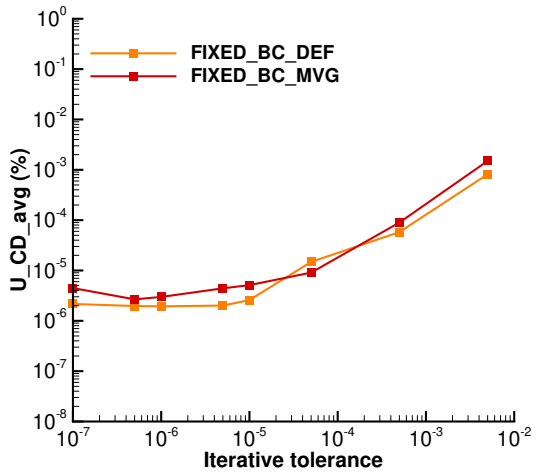

Figure 5.17: Statistical uncertainty for CD_{avg} as a function of iterative tolerance, for the **fixed case**.

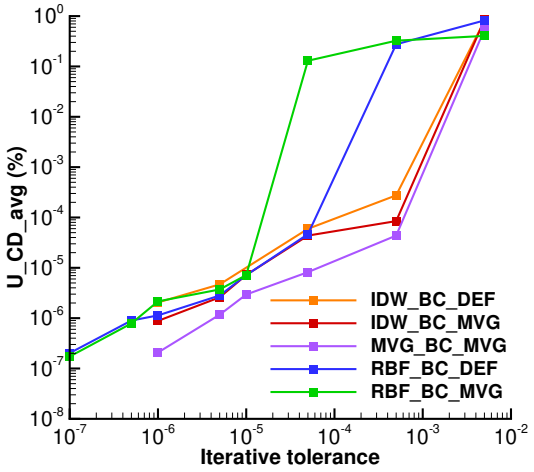

Figure 5.18: Statistical uncertainty for CD_{avg} as a function of iterative tolerance, for the **imposed motion** case with $U_R = 3.0$.

The first aspect that stands out when analysing the previous figures is the difference in the evolution of the statistical error in the fixed vs. imposed motion case (for any of the two selected variables, either

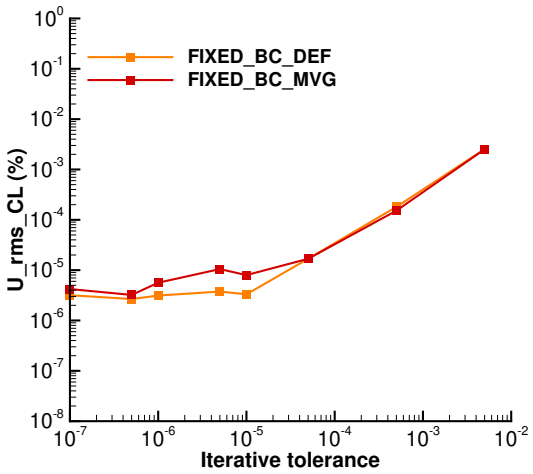

Figure 5.19: Statistical uncertainty for CL_{rms} as a function of iterative tolerance, for the **fixed case**.

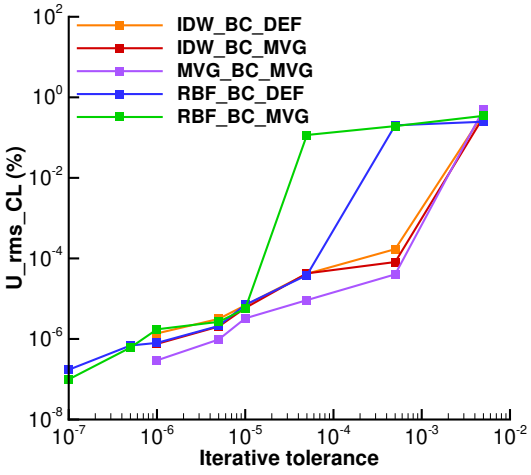

Figure 5.20: Statistical uncertainty for CL_{rms} as a function of iterative tolerance, for the **imposed motion** case with $U_R = 3.0$.

CD_{avg} or CL_{rms}). On the one hand, it is clear that in the fixed case, the statistical error reaches a *plateau* for values of iterative tolerance lower than 1×10^{-5} (approximately). On the other hand, for the imposed motion scenario, the statistical error displays a steady decreasing trend as the iterative tolerance is lowered. Furthermore, it is relevant to compare the order of magnitude of the statistical error for both cases, for typical values chosen for the iterative tolerance; establishing this comparison for 5×10^{-4}, it is clear that the statistical error is unacceptably large in the imposed motion scenario ($\approx 1 \times 10^{-1}$ to 1×10^{0} for the RBF method), while low enough in the fixed cases (lower than 1×10^{-3} for both selected variables). The differences found in the statistical error for the fixed and imposed motion cases are further discussed within the summary presented in section 5.4.

5.3 Iterative error estimation

After analysing the statistical error in the aforementioned cases, the iterative error associated to the selected variables (for the same test cases) was evaluated. The procedure referenced in [47] was used to perform error estimation. Therefore, the CD_{avg} and CL_{rms} values were computed for each simulation (run with a given iterative tolerance, for the reference grid, **grid 64**), and then the obtained values (for each iterative tolerance) were used to evaluate the iterative convergence of the selected parameters.

In other words, the simulation was run for all the selected test cases (fixed and imposed motion), progressively lowering the convergence tolerance value, until the iterative error and the statistical error had approximately the same order of magnitude. It should be mentioned that the importance of this step lies in ensuring that both these uncertainties - statistical and iterative - are controlled and expected to be significantly lower than the discretisation error (analysed in section 5.5).

The iterative convergence study was performed for the reference grid (grid64), and it was found that even for extremely low iterative tolerance values (for example, 1×10^{-7}, for the RBF method), the

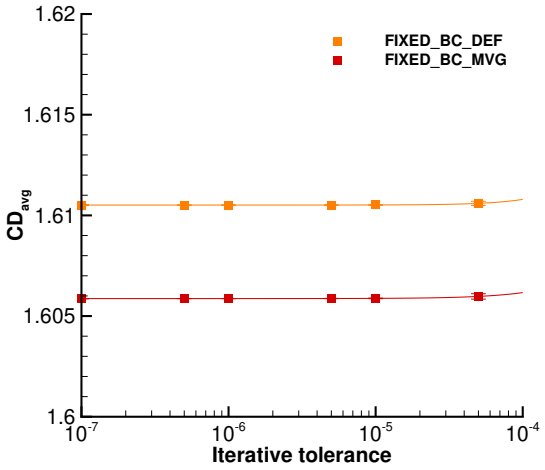

Figure 5.21: Iterative convergence for CD_{avg} for the **fixed case**.

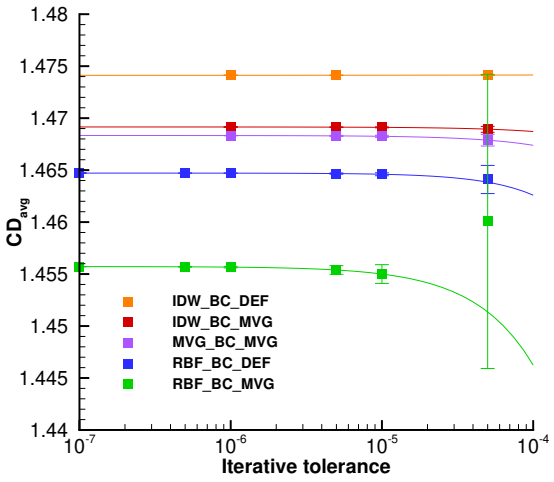

Figure 5.22: Iterative convergence for CD_{avg} for the **imposed motion** case with $U_R = 3.0$.

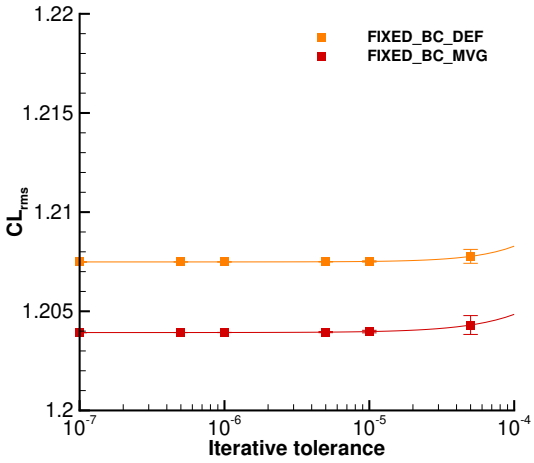

Figure 5.23: Iterative convergence for CL_{rms} for the **fixed case**.

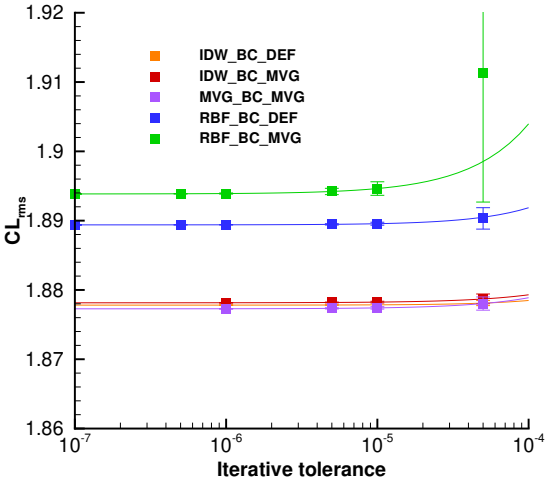

Figure 5.24: Iterative convergence for CL_{rms} for the **imposed motion** case with $U_R = 3.0$.

iterative error was still approximately two orders of magnitude larger than the statistical error (which was expectable, since the variance of the values of interest computed for the last cycles of the statistically steady signal was quite low - and therefore the iterative error was expected to be dominant with respect to the statistical error).

Lowering the iterative tolerance of the computations to 1×10^{-6} (for the MVG and IDW methods) and to an even lower value of 1×10^{-7} allowed however a deeper understanding of the behaviour of the iterative error. In fact, analysing the tables presented in section 5.4, it is visible that the variation in the error is quite small, which ensures that both the statistical and iterative part of the error are appropriately controlled and will not affect the estimation of the discretisation error.

Figures 5.25 and 5.26 display the differences found in the time traces of the lift coefficient, for $U_R = 3.0$, when using the deforming grid setup (RBF method) combined with the two sets of bound-

ary conditions. It is clear that for an iterative tolerance of 5×10^{-5} (figure 5.25) a slight difference in the peaks of RBF-BC-DEF and RBF-BC-MVG is noticed; however, this difference is significantly lower when the iterative tolerance criteria is set to 5×10^{-6} (figure 5.26). These figures once again present a good example of the need of choosing a sufficiently low iterative tolerance criteria for all simulations, in order to lower (to the best possible extent) the influence of the iterative error in the obtained solution.

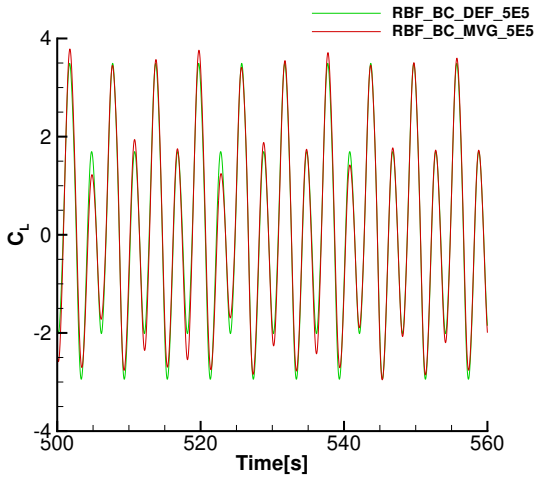

Figure 5.25: Comparison of the time traces of the lift coefficient, using the RBF method with both sets of BC, for an iterative tolerance of 5×10^{-5}.

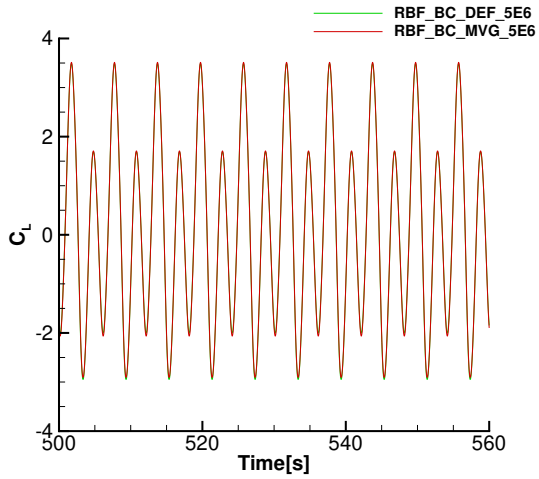

Figure 5.26: Comparison of the time traces of the lift coefficient, using the RBF method with both sets of BC, for an iterative tolerance of 5×10^{-6}.

It is also important to check the computational cost associated with the choice of the iterative tolerance value used in the simulations. Consequently, the required number of iterations per timestep (for both the fixed and imposed motion cases) was evaluated for each chosen iterative tolerance value. The previous paragraph explored the need for an accurate selection of an iterative tolerance; nevertheless, it is also quite important to have a practical measure of the computational cost of the choice. In order to have an approximate measure for this parameter, the number of iterations per timestep was averaged over a determined number of timesteps, for all the cases being analysed. Figures 5.27 and 5.28 display the general trend for both the fixed and imposed motion setups.

Analysing figures 5.27 and 5.28, an approximately linear trend (in the selected logarithmic scale) is identified (for the growth of the number of iterations with the decrease in the iterative tolerance value). Furthermore, it is clear that even for the lowest value analysed (1×10^{-7}), the number of iterations for both the fixed and imposed motion cases is still quite acceptable, which would allow (computation-cost wise) the choice of a value for the iterative tolerance as low as 1×10^{-7}, if deemed necessary.

All in all, the previous analysis was therefore essential to ensure an appropriate choice of iterative tolerance to be used in the simulations with the remaining grids, avoiding the possible mistake of assuming comparable statistical and iterative error behaviour for fixed/imposed motion cases. Additionally, the evaluation of the number of iterations per timestep for all cases granted some confidence in the "computational affordability" of the selected range of iterative tolerances, ensuring that any choice made within that range was suitable (computation-cost wise). Thus, a value of $\mathbf{5 \times 10^{-6}}$ was chosen to perform the

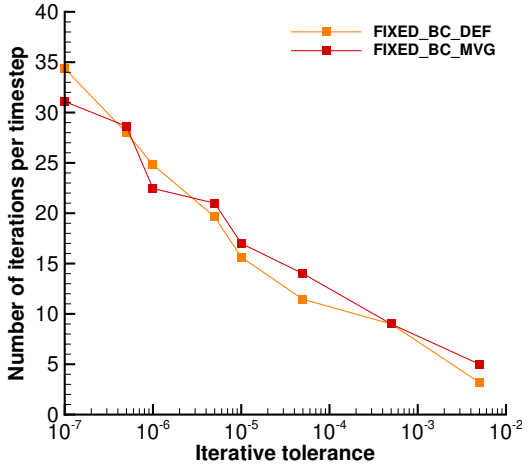

Figure 5.27: Number of iterations required per timestep, for the **fixed** case (with both sets of BC).

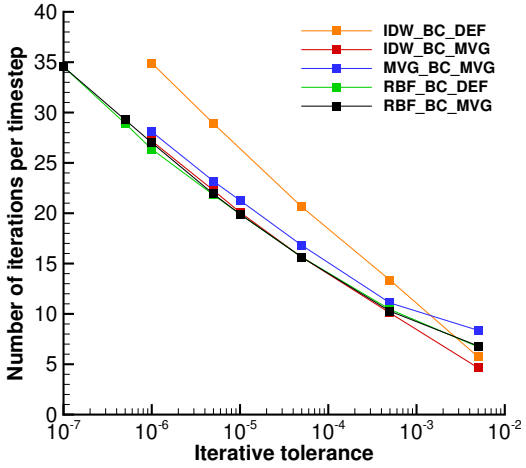

Figure 5.28: Number of iterations required per timestep, for the **imposed motion** case (all methods with both sets of BC), for $U_R = 3.0$.

remaining simulations (which were run, as previously mentioned, over a total of $\mathbf{200}$ cycles in all cases).

5.4 Statistical and iterative error: summary

5.4.1 2D Fixed Case: BC-DEF

$\mathbf{CD_{avg}}$

Iterative tolerance	Statistical error (%)	Iterative error (%)
1×10^{-5}	2.58E-06	3.98E-04
5×10^{-6}	2.01E-06	1.27E-04
1×10^{-7}	2.16E-06	1.72E-05

Table 5.3: Statistical and iterative error for the FIXED-BC-DEF case. Variable: CD_{avg}.

$\mathbf{CL_{rms}}$

Iterative tolerance	Statistical error (%)	Iterative error (%)
1×10^{-5}	3.31E-06	2.63E-03
5×10^{-6}	3.76E-06	9.54E-04
1×10^{-7}	3.18E-06	3.86E-05

Table 5.4: Statistical and iterative error for the FIXED-BC-DEF case. Variable: CL_{rms}.

Analysing tables 5.3 and 5.4, it is clear that the statistical error is overall lower than the iterative error for both quantities of interest; however, the difference between the two errors tends to be less significant as the iterative tolerance chosen for the simulation is reduced.

5.4.2 IDW-BC-DEF

$\mathbf{CD_{avg}}$

Iterative tolerance	Statistical error (%)	Iterative error (%)
5×10^{-5}	5.95E-05	2.51E-03
5×10^{-6}	4.69E-06	1.27E-03
1×10^{-6}	2.05E-06	7.92E-04

Table 5.5: Statistical and iterative error for the IDW-BC-DEF method, $U_R = 3.0$. Variable: CD_{avg}.

$\mathbf{CL_{rms}}$

Iterative tolerance	Statistical error (%)	Iterative error (%)
5×10^{-5}	4.16E-05	1.95E-02
5×10^{-6}	3.14E-06	1.23E-03
1×10^{-6}	1.37E-06	1.78E-04

Table 5.6: Statistical and iterative error for the IDW-BC-DEF method, $U_R = 3.0$. Variable: CL_{rms}.

Tables 5.5 and 5.6 again display comparable values for the statistical and iterative error between the two quantities of interest. However, it is interesting to outline that, overall, the error tends to be larger (both in its statistic and iterative components) in the imposed motion case, when compared to the fixed case. This behaviour is not surprising, since the imposed motion test cases comprise additional sources of error, which are not present in the fixed case (namely, the mesh deformation itself). Nevertheless, it should be outlined that, for the same value of iterative tolerance (say, 5×10^{-6}), the statistical error might still be slightly larger for the fixed case (taking as an example the comparison between the quantity CL_{rms} for both setups). A possible explanation for this trend is the number of cycles needed for the onset of vortex shedding (and for attaining the solution) in the fixed and imposed motion cases: in the former, a greater number of cycles is required, and thus a simulation comprising a total of 200 periods might have a larger contribution of the first cycles when computing the statistical error; in the latter, a smaller number of cycles is needed, thus diminishing the influence of the first periods in the (statistical) error computation.

Nevertheless, it is worth pointing out that the (potential) difference introduced by this factor is indeed small (the values displayed in tables 5.4 and 5.6 are within the same order of magnitude, 1×10^{-6}), and therefore a modification of the total number of cycles in each simulation was not deemed necessary.

5.5 Grid/time refinement studies

The statistical and iterative convergence studies are fundamentally decisive in the process of estimating the numerical uncertainty of CFD calculations. According to Eça et al. [44], and as previously mentioned, "the iterative error should be two to three orders of magnitude smaller than the discretisation error in order not to disturb the estimation of the numerical error". Thus, as in the previous sections the statistical and iterative error were shown to be sufficiently small, in this section the iterative, statistical and round-

off components of the numerical error will be considered negligible when compared to the discretisation error.

5.5.1 Discretisation error estimation

According to [48], the recommended method for discretisation error estimation is the Richardson extrapolation (RE) method. In spite of some of the identified shortcomings of the RE (namely, the local extrapolated values of the predicted variables may not display neither a smooth nor monotonic dependence on grid resolution), this method is still considered the most reliable strategy to predict and assess numerical uncertainty.

The estimation of the discretisation error in the present work followed the procedure found in [44]. In [44], the error is estimated using a truncated power series expansion: being Φ an integral of a local flow quantity, Φ_0 an estimate of the exact solution, α a constant to be determined, h_i the typical cell size, Δt_i the timestep, and p_x and p_t the observed order of grid/time convergence (respectively), the discretisation error can be computed as:

$$\epsilon_\Phi \simeq \delta_{RE} = \Phi_i - \Phi_0 = \alpha_x \left(\frac{h_i}{h_1}\right)^{p_x} + \alpha_t \left(\frac{\Delta t_i}{\Delta t_1}\right)^{p_t} \tag{5.3}$$

Using an equal grid/time refinement ratio,

$$\left(\frac{h_i}{h_1}\right)^{p_x} = \left(\frac{\Delta t_i}{\Delta t_1}\right)^{p_t} \tag{5.4}$$

which yields

$$\epsilon_\Phi = \Phi_i - \Phi_0 = \alpha \left(\frac{\lambda_i}{\lambda_1}\right)^{p} \tag{5.5}$$

With the three unknowns (Φ_0, α, and p), it can be concluded that the minimum number of grids required for error estimation is therefore $n_g = 3$. In order to apply equation 5.5, it is necessary to ensure that the higher order terms (ommited in the power series expansion) can be considered negligible. When this condition is verified, the selected grids are considered to be in the **assymptotic range of convergence**. Another condition necessary to the applicability of equation 5.5 is the use of **geometrically similar** grids, also recommended by [48]. In other words, the grid refinement ratio (h_i/h_1) must be constant in all directions, and the deviation from orthogonality and skewness of the grid must remain unaffected.

While for simple problems it is usually possible to ensure that the three grids are in the assymptotic range and that the data has little or no scatter, the data yielded by most simulations hardly ever complies with these conditions. Consequently, the work presented in [44] adds three additional possibilities for error estimation:

$$\epsilon_\Phi \simeq \delta_1 = \Phi_i - \Phi_0 = \alpha \left(\frac{\lambda_i}{\lambda_1}\right) \tag{5.6}$$

$$\epsilon_\Phi \simeq \delta_2 = \Phi_i - \Phi_0 = \alpha \left(\frac{\lambda_i}{\lambda_1} \right)^2 \tag{5.7}$$

$$\epsilon_\Phi \simeq \delta_{12} = \Phi_i - \Phi_0 = \alpha_1 \left(\frac{\lambda_i}{\lambda_1} \right) + \alpha_2 \left(\frac{\lambda_i}{\lambda_1} \right)^2 \tag{5.8}$$

The first two equations can be used for monotonically converging solutions (if the estimation with equation 5.5 is unreliable) and the last one is also appropriate for situations with non-monotonic convergence. It should be mentioned that, even though only **two** grids are needed for error estimation with equations 5.6 and 5.7, and only **three** grids if equations 5.5 and 5.8 are to be used, it is beneficial to include a **fourth** grid to determine the error. The addition of an additional grid allows a quality check for p (order of convergence), which is helpful since this parameter is extremely sensitive to perturbations present in the data.

Having at least a set of **four** grids, it is possible to perform the error estimation in the least-squares sense, either using an unweighted or weighted approach (which assigns a greater weight to the solution in the finest grid). More details concerning the the least-squares minimization, and the measure of the quality of the fits can be found in [44].

Knowing the period of the imposed motion to the cylinder, it was then possible to define the number of timesteps necessary for each cycle (a full oscillation of the cylinder), according to the relation

$$Number\ of\ timesteps\ per\ cycle = \frac{T}{\Delta t} \tag{5.9}$$

being T the period of the motion. After completing the tuning for the reference grid, the value for Δt to be used in the simulations with the remaining grids was computed, keeping in mind that the grid refinement ratio and time refinement ratio should be chosen to be the same from grid to grid, in order to preserve the initial CFL condition tuned for the reference grid. That is,

$$\frac{h_i}{h_j} = \frac{\Delta t_i}{\Delta t_j} \tag{5.10}$$

being the subscripts i and j used in the present case to designate any subset of two grids i, j from the set of grids initially selected. Tables 5.7 to 5.10 summarize the computed parameters for each of the used grids, both in the fixed and imposed motion cases.

5.5.2 2D Fixed cylinder

As suggested by table 5.7, the number of timesteps corresponding to a full cycle had to be computed (in a post-processing stage) using the time traces of the transverse force (y-direction). In the fixed cylinder case, there is no external excitation and, therefore, it is not possible to determine the number of timesteps/period according to the reduced velocity being used. Thus, this value was computed through a post-processing routine which took as a reference the points with $C_L = 0$ in the time history of the forces. The figures below (5.29 and 5.30) present the grid refinement study for the fixed case, using the

Grid number	Number of timesteps per cycle (computed)	Δt [s]
40	≈ 157	0.03
48	≈ 187	0.025
56	≈ 214	0.0214(285714)
64	≈ 241	0.01875
80	≈ 293	0.015
96	≈ 344	0.0125

Table 5.7: Fixed cylinder: selected grids and corresponding Δt for the grid refinement study.

grids displayed in table 5.7.

It is clear that there is very little scatter in the obtained data (the curve fits are nearly ideal), and that the choice of boundary conditions hardly influences the curve fits and the estimated results in the limit $\frac{h_i}{h_1} \rightarrow 0$. Also, the convergence behaviour with and without the contribution of the two finest grids (80 and 96) is presented, displaying a clear improvement in both setups when the two finest grids are considered. This trend displays the ideal situation that would be desirable in the imposed motion cases - that is, the use of two additional, finer grids - if not for the shortcomings concerning the appearance of low frequencies with grid refinement (as previously explained for the case of $U_R = 3.0$).

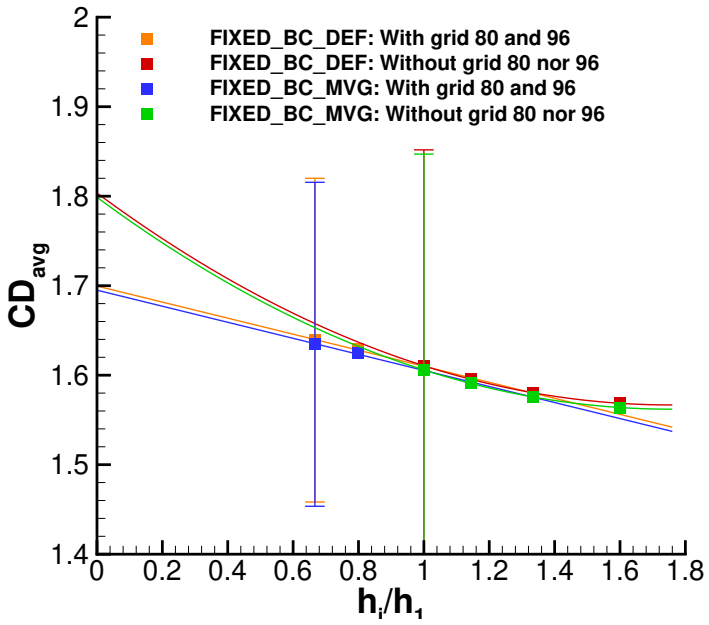

Figure 5.29: Convergence behaviour of the variable CD_{avg} for both setups (FIXED-BC-DEF and FIXED-BC-MVG), superimposed on the same plot, with and without the inclusion of the two finest grids (80 and 96).

5.5.3 2D Moving cylinder: $U_R = 3.0$

Figures 5.31 and 5.32 display the grid refinement study performed for the two variables of interest, for the imposed motion setup with $U_R = 3.0$. The (undesirable) influence of the coarsest grid is clear, dramatically modifying the curve fit for the RBF method when compared to the IDW and MVG methods.

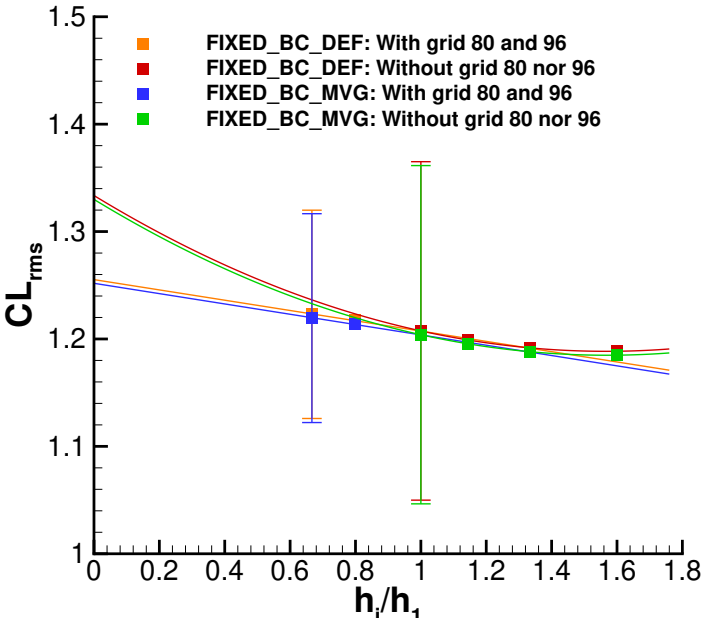

Figure 5.30: Convergence behaviour of the variable CL_{rms} for both setups (FIXED-BC-DEF and FIXED-BC-MVG), superimposed on the same plot, with and without the inclusion of the two finest grids (80 and 96).

Grid number	Number of timesteps per cycle	Δt [s]
40	100	0.03
48	120	0.025
56	140	0.0214(285714)
64	160	0.01875

Table 5.8: $U_R = 3.0$: selected grids and corresponding Δt for the grid refinement study.

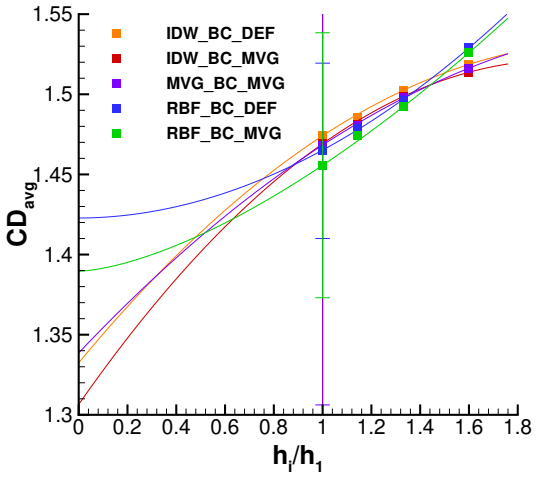

Figure 5.31: Grid refinement study for CD_{avg}, for $U_R = 3.0$, using the four grids up to grid 64.

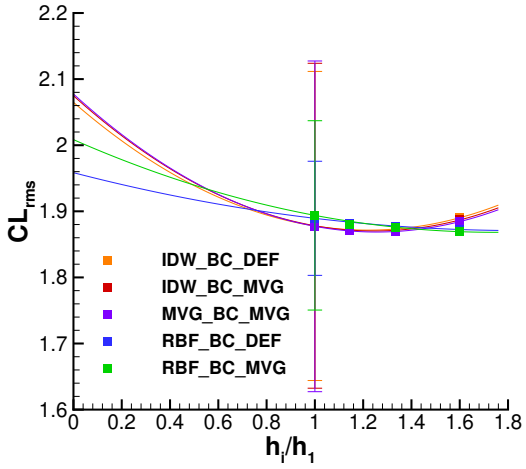

Figure 5.32: Grid refinement study for CL_{rms}, for $U_R = 3.0$, using the four grids up to grid 64.

Figures 5.33 and 5.34 exhibit the influence of excluding from the study the information corresponding to the coarsest grid. It is clearly observed that the estimation of the exact solution dramatically changes when the coarsest grid is removed, which is a good indication that the influence of this data point is potentially overestimated when performing the curve fit (and thus the estimation of the exact solution using coarse grids should be analysed under a conservative point of view).

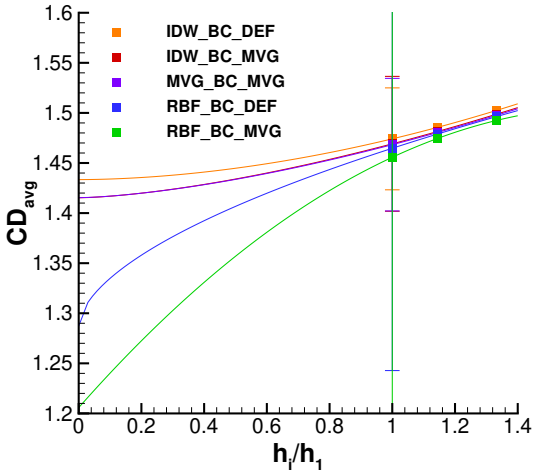

Figure 5.33: Grid refinement study for CD_{avg}, for $U_R = 3.0$, using the **three finest** grids (64, 56, 48).

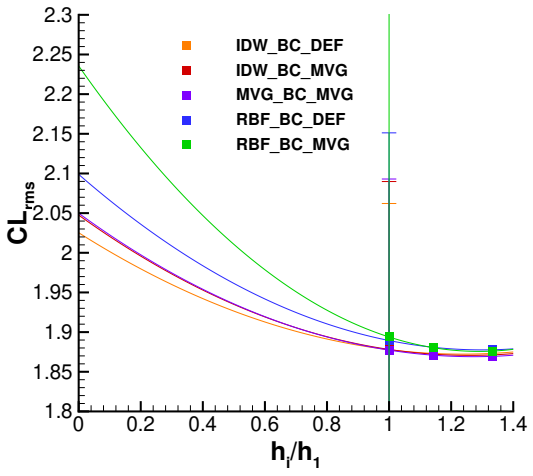

Figure 5.34: Grid refinement study for CL_{rms}, for $U_R = 3.0$, using the **three finest** grids (64, 56, 48).

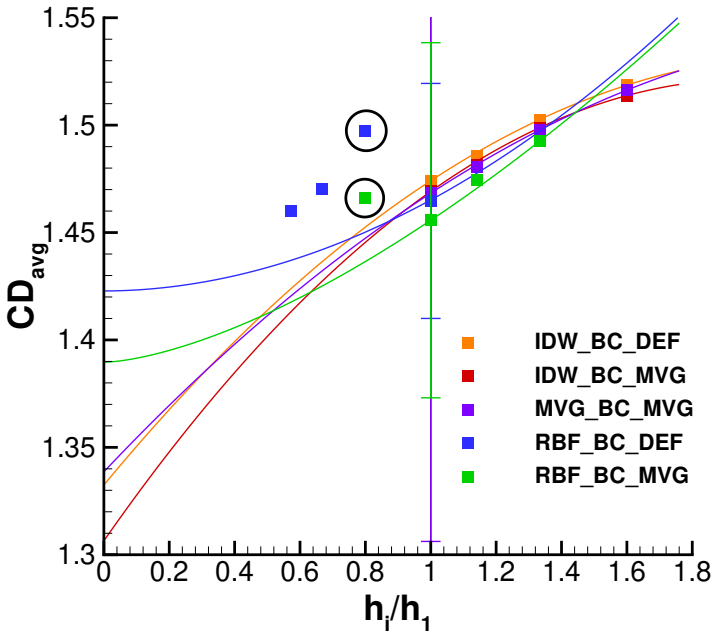

Figure 5.35: Grid refinement study for CD_{avg}, for $U_R = 3.0$, using the four selected grids, **with the addition of grid 80** (for the RBF-BC-MVG setup) and **grids 80, 96 and 112** (for the RBF-BC-DEF setup).

Figure 5.35 displays the trend observed in the computed CD_{avg} when adding the information corresponding to grids 80, 96 and 112 (for which the FFT of the time history of the force coefficients revealed low frequency peaks, as previously mentioned). As it is clearly seen, the data points corresponding to these grids are completely off-trend with respect to the remaining grids (and there is even a clear difference between the RBF-BC-DEF and RBF-BC-MVG setups for grid 80, outlined with black circles), which is a good indication that, in this case, the mean flow properties are not correctly captured anymore, leading to a mathematical model that depends on the grid size (which is not the goal of a RANS formulation).

However, an important aspect that should be outlined is the similarity registered in the data points for all the methods and boundary conditions (in the grids selected for the refinement study, in which the mean flow properties were considered to be captured), which is a good indication that all three techniques (RBF, IDW and MVG) accurately handle imposed motion.

5.5.4 2D Moving cylinder: $U_R = 5.0$

Grid number	Number of timesteps per cycle	Δt [s]
40	125	0.04
48	150	0.0(3)
56	175	0.0(285714)
64	200	0.025

Table 5.9: $U_R = 5.0$: selected grids and corresponding Δt for the grid refinement study.

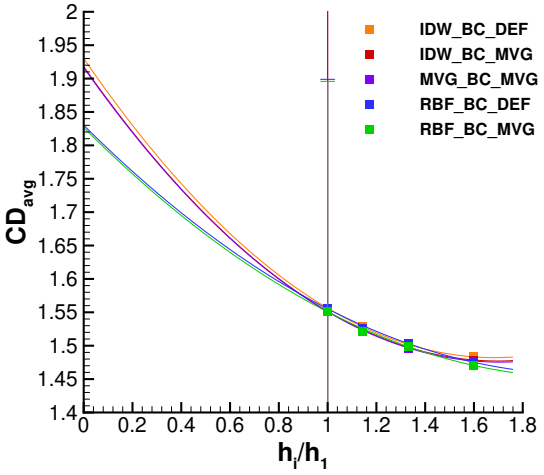

Figure 5.36: Grid refinement study for CD_{avg}, for $U_R = 5.0$, using the four grids up to grid 64.

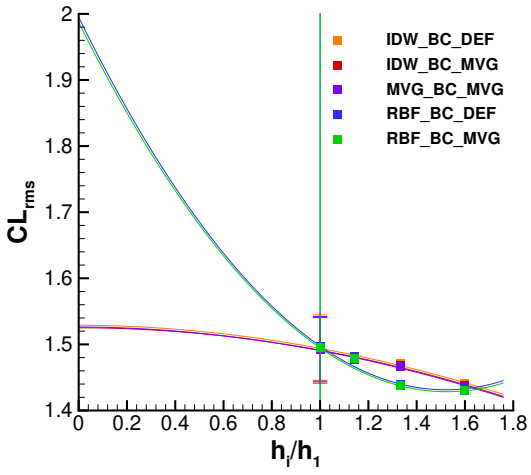

Figure 5.37: Grid refinement study for CL_{rms}, for $U_R = 5.0$, using the four grids up to grid 64.

The trends shown in figures 5.36 and 5.37 once again illustrate the shortcomings of using information from coarse grids in the study. In spite of a smaller influence of the coarsest grid ($\frac{h_i}{h_1} = 1.6$) on the estimation of the exact solution for the case of CD_{avg}, the effect on CL_{rms} is much more significant.

Namely, it can be argued that the position of the points corresponding to the coarsest grid in this case can dramatically change the tendency of the curve fit, and, ultimately, the estimation of the exact solution. In order to obtain a clearer insight on the effects of the coarsest grid data on the refinement study, a new analysis was performed, using only the information of the three finest grids. The results are displayed in figures 5.38 and 5.39.

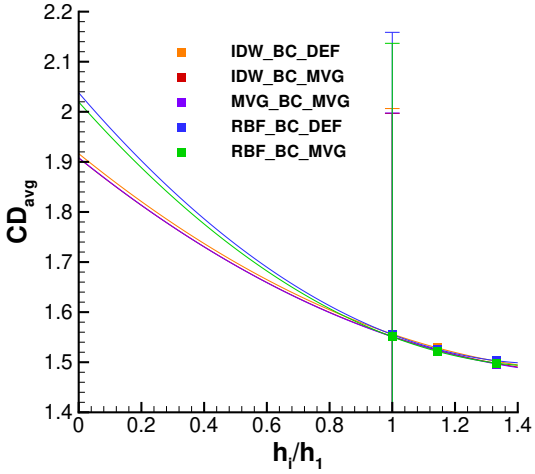

Figure 5.38: Grid refinement study for CD_{avg}, for $U_R = 5.0$, using the **three finest** grids.

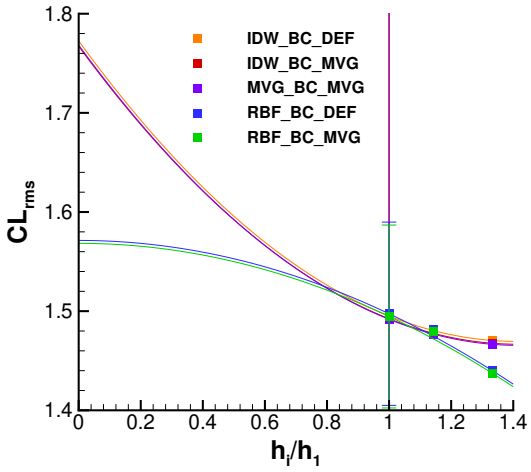

Figure 5.39: Grid refinement study for CL_{rms}, for $U_R = 5.0$, using the **three finest** grids.

The effects of this change are small in the case of CD_{avg} (in the sense that the trend in the estimation of the exact solution is maintained for all methods + BC). Nevertheless, it is observed that in this second case, the RBF-BC-DEF and RBF-BC-MVG setups overpredict the exact solution with respect to the remaining methods + BC (IDW-BC-DEF, IDW-BC-MVG, MVG-BC-MVG), contrarily to what was seen in the study with the original four grids. However, the effects of using only the three finest grids are much more dramatic in the case of CL_{rms}, completely changing the trend of the curve fits for the RBF method (with both BC) and severely changing the estimation for $\frac{h_i}{h_1} = 0$. This type of behaviour would therefore benefit from the addition of finer grids to the study (to improve the overall confidence in the estimation of the exact solution); however, the 2D analysis was severely limited in this aspect due to the absence of sufficient turbulent dissipation in finer grids (which ultimately prevented the correct capturing of the mean flow properties). This aspect will be further explored in chapter 6, which will reflect on some of the most relevant shortcomings of the adopted modelling strategies.

Figure 5.40 displays the data points corresponding to the simulations using grid 80, for the IDW-BC-DEF setup, and grids 80, 96, and 112 for the RBF-BC-DEF setup. In this case, it was observed that the appearance of low frequency content in the time traces of the force coefficients did not significantly affect the convergence behavioural trend (the data points corresponding to grid 80 for the IDW-BC-DEF and RBF-BC-DEF setups are even superimposed, due to a very negligible difference in the CD_{avg} value), possibly due to the fact that in the lock-in region, in which the vortex shedding frequency and the external excitation frequency collapse onto one, the expected frequency content is still well separated from the

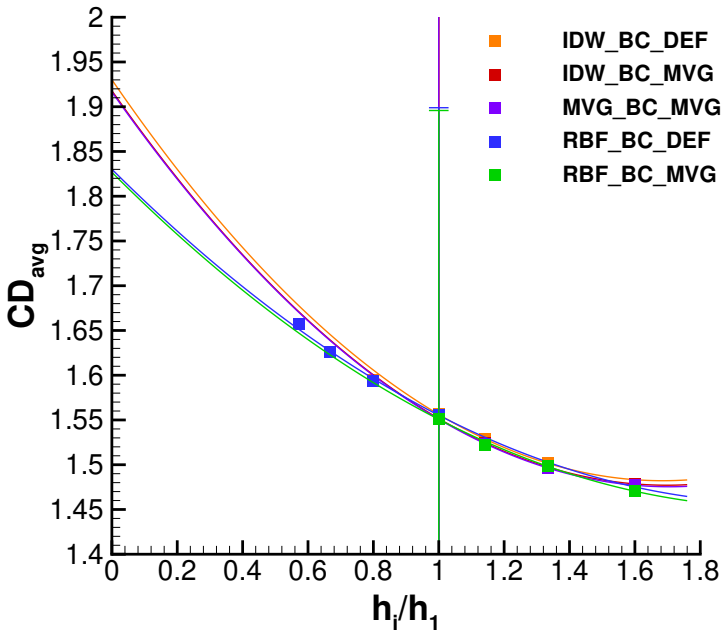

Figure 5.40: Grid refinement study for CD_{avg}, for $U_R = 5.0$, using the four selected grids, **with the addition of grid 80** for the IDW-BC-DEF setup and **grids 80, 96 and 112** for the RBF-BC-DEF setup.

low frequency oscillations appearing with grid refinement. However, no error estimation was performed for the three finest grids (80, 96, 112), since it was still not entirely clear if the mean flow properties were accurately being captured.

As verified in the imposed motion cases with $U_R = 3.0$, the results yielded by the several techniques (either moving or deforming) were quite similar, which again indicates that in the range where the mean flow properties are accurately being captured the methods to handle imposed motion can be considered equivalent. Additionally, the effect of the selected set of boundary conditions on the computed quantities of interest can be considered negligible,

5.5.5 2D Moving cylinder: $U_R = 10.0$

Grid number	Number of timesteps per cycle	Δt [s]
40	250	0.04
48	300	0.0(3)
56	350	0.0(285714)
64	400	0.025
80	500	0.02

Table 5.10: $U_R = 10.0$: selected grids and corresponding Δt for the grid refinement study

A brief comparison between the $U_R = 5.0$ and $U_R = 10.0$ cases reveals that, for both variables (CD_{avg} and CL_{rms}), the estimated exact solutions fall within a much narrower range for $U_R = 10.0$ (figures 5.41 and 5.42) than for $U_R = 5.0$. As expected, the curve fits are not optimal in the CL_{rms} case due to a larger dispersion in the available data; nevertheless, the uncertainty associated with the data

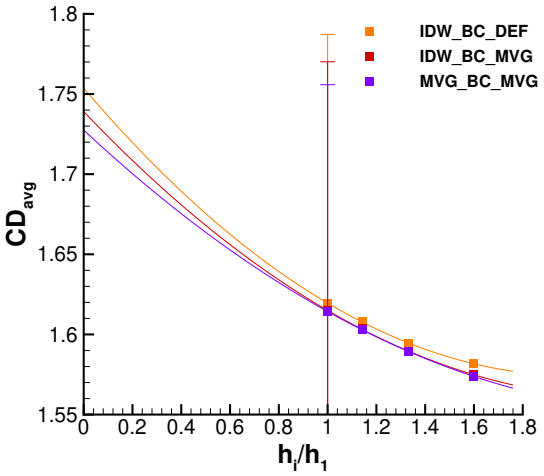

Figure 5.41: Grid refinement study for CD_{avg}, for $U_R = 10.0$, using the four grids up to grid 64.

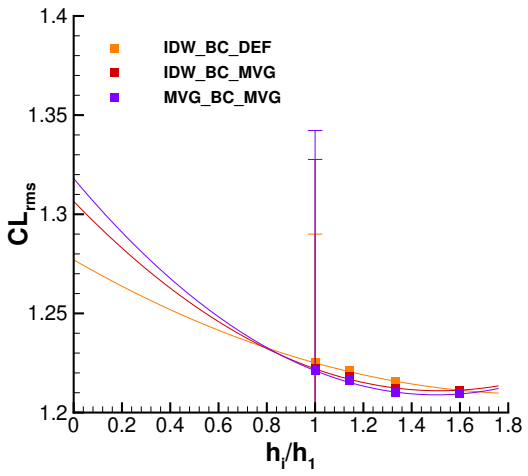

Figure 5.42: Grid refinement study for CL_{rms}, for $U_R = 10.0$, using the four grids up to grid 64.

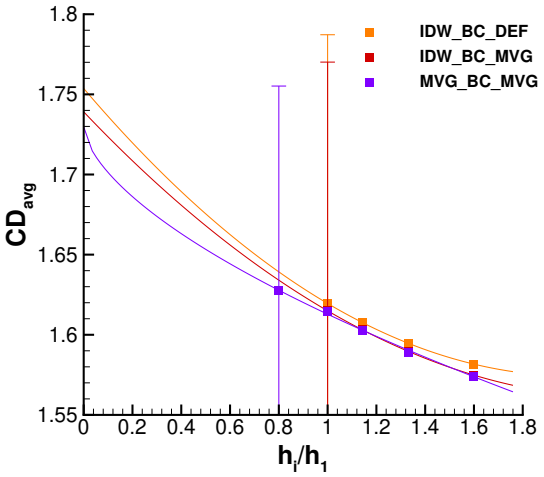

Figure 5.43: Grid refinement study for CD_{avg}, for $U_R = 10.0$, using all five selected grids (80, 64, 56, 48, 40).

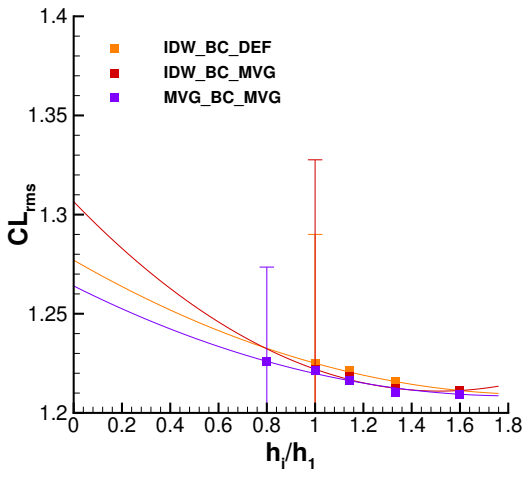

Figure 5.44: Grid refinement study for CL_{rms}, for $U_R = 10.0$, using all five selected grids (80, 64, 56, 48, 40).

for the reference grid ($\frac{h_i}{h_1} = 1$) is overall smaller for $U_R = 10.0$.

The aforementioned behaviour is not surprising. In fact, it is visible that the test case with $U_R = 10.0$ approaches the fixed case results (previously presented), both in the expected exact values for CD_{avg} (the dispersion in CL_{rms} data points - figure 5.42 - is higher and therefore the trend is not as clear for this variable) and in the expected uncertainty associated with the results. This confirms an expected similarity between both cases, since as U_R is increased (or, conversely, as the frequency of excitation is decreased), the cylinder approaches a fixed condition, which is attained in the limit $U_R = \infty$.

Figures 5.43 and 5.44 feature the data points, line adjustment and error bars for **grid 80**, in the

MVG-BC-MVG setup, since according to the FFT analysis the solution in this grid was still considered to represent the mean flow properties (well isolated peaks; absence of well-distributed low frequency content).

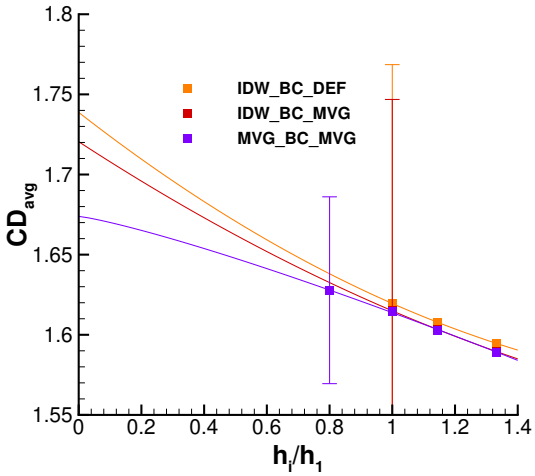

Figure 5.45: Grid refinement study for CD_{avg}, for $U_R = 10.0$, using the **four finest** grids (80, 64, 56, 48).

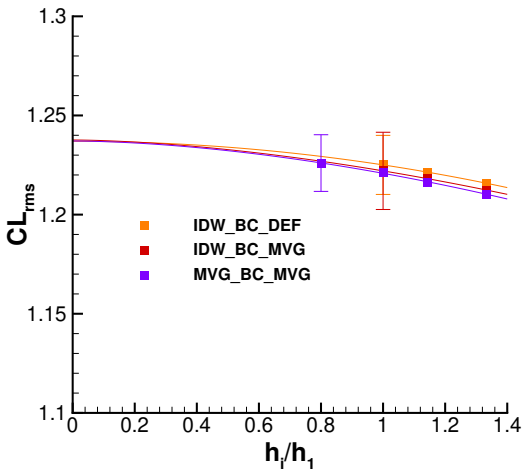

Figure 5.46: Grid refinement study for CL_{rms}, for $U_R = 10.0$, using the **four finest** grids (80, 64, 56, 48).

Figures 5.45 and 5.46 once again display the influence of removing the coarsest grid (grid 40) from the analysis. While a slight improvement is observed for the MVG-BC-MVG estimation of a CD_{avg} exact solution (due to a more dominant effect of the presence of grid 80), a dramatic change is noticed in the case of CL_{rms}: all three setups display approximately the same estimation of an exact solution and the computed error is significantly decreased with respect to the case including grid 40, figure 5.44. Once again, the similarity in the results yielded by the three setups (IDW-BC-DEF, IDW-BC-MVG, MVG-BC-MVG) is also clear in this case (complemented with the advantage of the inclusion of grid 80 in the curve fit, giving a more reliable error estimation, which was not possible in the previous reduced velocities).

5.6 3D Analysis

In order to gain a broader insight on the phenomena identified for the 2D test cases, a few simulations were performed using a three-dimensional setup. Essentially, the 3D test cases aimed at:

- Analysing the influence of the cylinder aspect ratio (L/D) on the obtained frequency spectrum of the lift force coefficient response;
- Analysing the influence of the grid refinement on the computed force coefficients of interest (CD_{avg} and CL_{rms}).

The RBF-BC-DEF setup, and three different cylinder aspect ratios were evaluated: $L/D = 3.0; 6.0; 12.0$.

Figure 5.47 shows the influence of the cylinder length (or, equivalently, aspect ratio) in the frequency spectrum of the lift coefficient signal. It is clear that reducing the length from $L/D = 12.0$ to 6.0 (and even further to 3.0) leads to the appearance/growth of the low frequency peaks in the response. This behaviour essentially confirms the decrease of the dissipation provided by the turbulence model as the cylinder aspect ratio (length) is decreased. Since the number of cells in the z direction is the same for the three values of aspect ratio, lower values of L/D will be associated with lower diffusion from the turbulence model, leading to an enrichment in the unwanted frequency content of the signal.

Figure 5.48 exhibits the change in the frequency content of the lift coefficient signal as the grid is refined (for $U_R = 3.0$ and an aspect ratio $L/D = 3.0$). It is visible that the aforementioned low frequency content is already present for the coarsest grid (grid 40) and its prominence tends to increase with grid refinement (the low frequency peaks are clearly visible for grid 64), as expected. This behaviour fundamentally questions the capability to capture mean flow properties in the 3D simulations (according to the used RANS formulation), even in the coarsest grids, thus limiting the analysis performed in the present study (additional grid refinement would be unnecessary to confirm this trend).

Figure 5.49 displays the FFT for the lift coefficient signal, concerning a simulation in grid 56, for an aspect ratio of $L/D = 12.0$, and several levels of iterative tolerance. It is clear that even at low values of iterative tolerance (1×10^{-6}), grid 56 displays significant, well-distributed, low-frequency content in the spectrum, which provides useful insight on the influence of the iterative error in the registered behaviour. At a sufficiently low level of 1×10^{-6}, the low frequency content is still present, and thus it was considered that further lowering the iterative tolerance would not eliminate this shortcoming.

Finally, figures 5.50 and 5.51 display the data points obtained for the two variables of interest (CD_{avg} and CL_{rms}), for grids 40, 48, and 56. It is important to outline that, in the 3D cases, the unwanted frequency content is even more significant than in the 2D simulations; therefore, the systematic procedure to compute statistical variables of interest employed in the 2D study is no longer applicable in the present case (which is revealed by the differences in the calculated variables when using the last 40 or 100 cycles of the time history of the forces, as shown in figures 5.50 and 5.51 for $L/D = 3.0$) and the obtained force coefficients should be evaluated under a conservative point of view.

All in all, the results obtained display the clear shortcomings of a RANS formulation (already identified in the 2D cases) in the studied 3D cases: the appearance of well distributed low frequency content questions the correct attainment of mean flow properties, due to a lack of diffusion provided by the employed turbulence model to filter these frequencies.

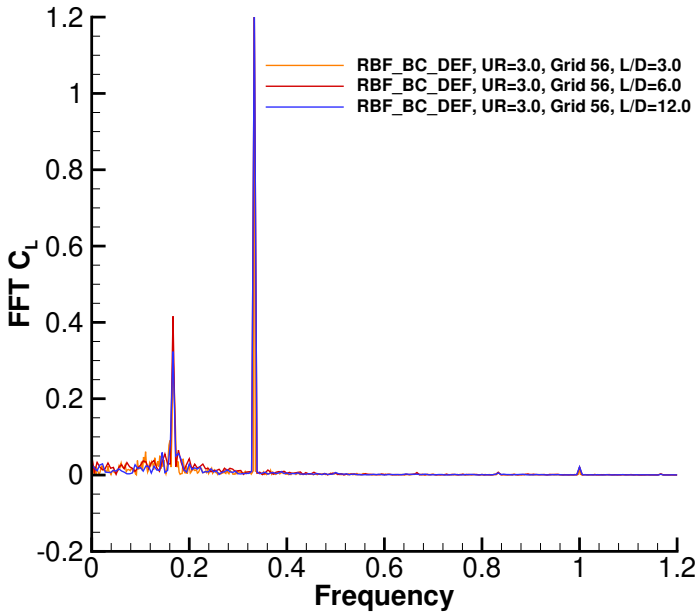

Figure 5.47: FFT analysis for the lift coefficient signal, using the RBF-BC-DEF setup, $U_R = 3.0$, **grid 56**, for $L/D = 3.0$, 6.0, and $L/D = 12.0$.

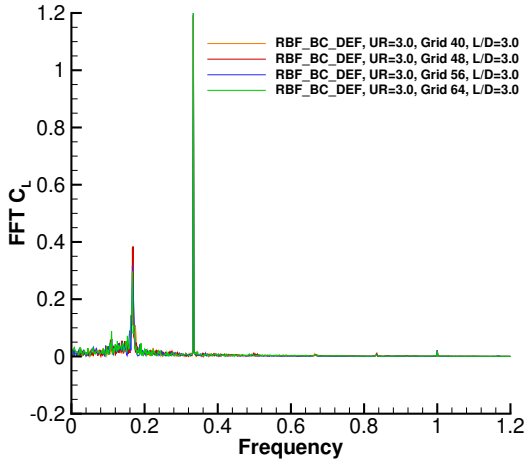

Figure 5.48: FFT analysis for the lift coefficient signal, using the RBF-BC-DEF setup, $U_R = 3.0$, for $L/D = 3.0$, grids **40, 48, 56, 64**.

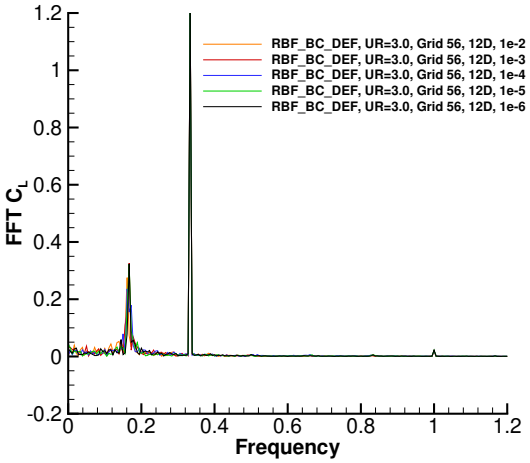

Figure 5.49: FFT analysis for the lift coefficient signal, using the RBF-BC-DEF setup, $U_R = 3.0$, **grid 56**, for $L/D = 12$, for 5 different iterative tolerance levels.

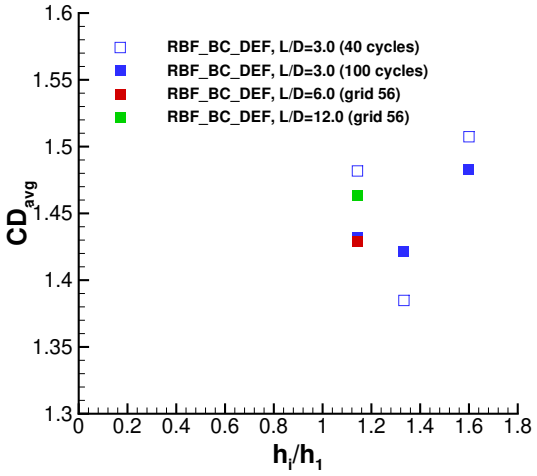

Figure 5.50: Data points for CD_{avg}, for $U_R = 3.0$ and $L/D = 3.0$, RBF-BC-DEF setup (grids 56, 48, 40). Additional points for $L/D = 6.0$ and $L/D = 12.0$ displayed for **grid 56**.

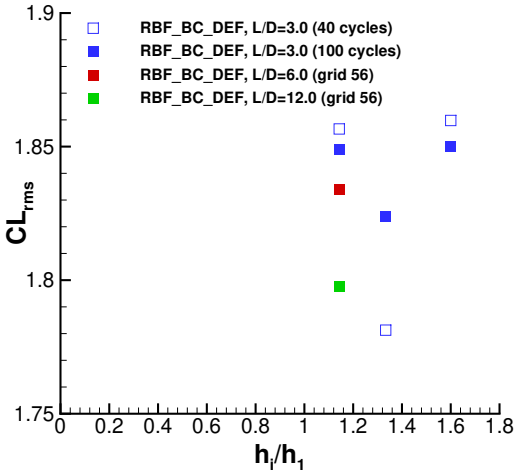

Figure 5.51: Data points for CL_{rms}, for $U_R = 3.0$ and $L/D = 3.0$, RBF-BC-DEF setup (grids 56, 48, 40). Additional points for $L/D = 6.0$ and $L/D = 12.0$ displayed for **grid 56**.

Chapter 6

Comparison with experimental data and flow analysis

6.1 Validation exercise: 2D and 3D cases

In order to perform a validation exercise, the work of Gopalkrishnan [30] was chosen as a reference in terms of experimental data (as mentioned in previous section of the present study). A quantitative comparison was intended; however, the experimental uncertainty was not clearly quantified and the error bars concerning the numerical calculations performed were quite significant (figure 6.1). Thus, only a qualitative comparison was performed for the RBF-BC-DEF setup (both for he 2D data, which is quite representative of the other setups represented in figure 6.1, and 3D data), using as a reference the experimental results.

Figure 6.1 presents the collection of 2D imposed motion results (for the three selected reduced velocities, $U_R = 3.0$, $U_R = 5.0$ and $U_R = 10.0$) and the reference experimental data from Gopalkrishnan [30]. The information displayed in this figure concerns the average drag coefficient (CD_{avg}), a representative parameter for this analysis. One of the first aspects standing out when analysing this plot is the proximity of the 2D numerical results to the experimental data, for $U_R = 3.0$. Nevertheless, this matching between results appears to be progressively lost as the reduced velocity is increased (that is, the experimental data is still comprised within the numerical error bars for $U_R = 5.0$, in spite of some difference in the results, and for $U_R = 10.0$ the numerical and experimental data are clearly different).

One may wonder about the relevance of the comparison between 2D and experimental (3D) cases, since the flow features are different in these two cases. On the one hand, the proximity of the 2D results and experimental data for the lowest reduced velocity, $U_R = 3.0$ (that is, the greatest frequency of excitation) suggests that the three-dimensional effects become less and less relevant for situations in which the cylinder is moving with a greater externally imposed frequency (situations in which the inertial terms are preponderant in the overall momentum balance, in comparison to the diffusive terms). On the other hand, as U_R is increased (that is, as the frequency of excitation is decreased and the cylinder approaches a fixed condition, which would correspond to $U_R = \infty$), the differences between the 2D and

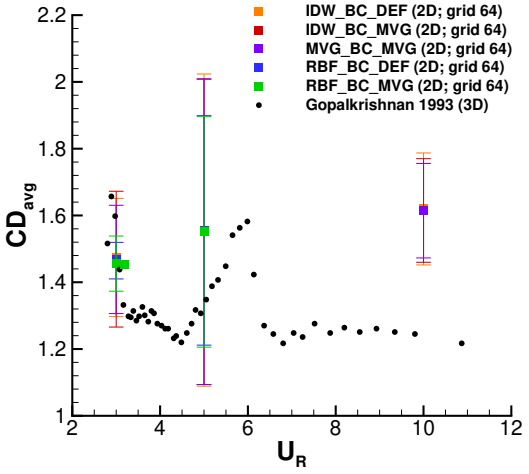

Figure 6.1: Comparison of the obtained 2D results with the available experimental data (3D) for the selected range of reduced velocities (U_R).

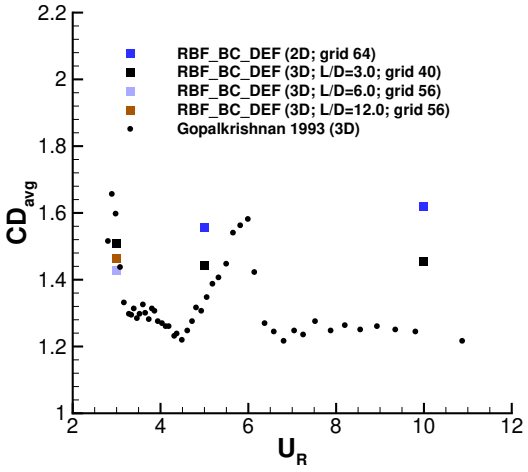

Figure 6.2: Comparison of the obtained 2D and 3D results with the available experimental data (3D) for the selected range of reduced velocities (U_R), for the RBF-BC-DEF setup.

3D cases become extremely clear. Figure 6.1 also includes an additional calculation (performed only for the reference grid, grid 64) for $U_R = 3.2$. The proximity of the data point corresponding to $U_R = 3.2$ to the points corresponding to $U_R = 3.0$ reinforces the confidence in the matching with the experimental data, in this range of reduced velocities. Additionally, the 3D numerical results (presented in figure 6.2) comply with the previously presented hypothesis: in fact, it is clear that there is a small difference between the 2D/3D cases for the lowest reduced velocity analysed ($U_R = 3.0$), whereas this difference becomes more apparent as the reduced velocity increases.

Thus, in spite of the identified problems for $U_R = 3.0$ with respect to capturing the mean flow, this case is also the one in which the 2D/3D/experimental have a better match, which confirms that, as the reduced velocity is decreased, the role of diffusion/turbulence modelling also decreases with respect to the overall momentum balance.

6.2 Vortex synchronization regions along the reduced velocity spectrum (2D cases)

In order to complement the analysis developed so far, it was found that it would be relevant to compare the main characteristics of the cylinder near-wake for all three reduced velocities, taking as a reference the work of Williamson [19], in which the vortex synchronization regions in the cylinder near wake were characterized (see subsection 2.1.3 for further details concerning Williamson's work). Furthermore, a comparison was also established for the different combinations deforming/moving grid methods + set of BC used in the present work. A brief analysis of figures 6.3 to 6.8 reveals a strong similarity in the near

wake structures for both selected setups (RBF-BC-DEF and MVG-BC-MVG), for each of the reduced velocities. This significantly improves the overall confidence in the obtained results; in fact, in spite of the selected set of BC and moving/deforming grid setup chosen, the well known near wake structures are correctly captured in both cases, and match the vortex synchronization patterns identified by Williamson in his work [19].

6.2.1 Near wake for $U_R = 3.0$

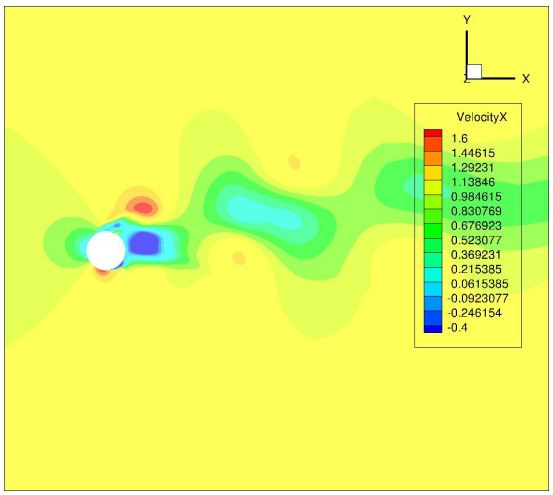

Figure 6.3: Instantaneous x velocity plot for the **RBF-BC-DEF** setup, at the point of minimum lift coefficient, for $U_R = 3.0$.

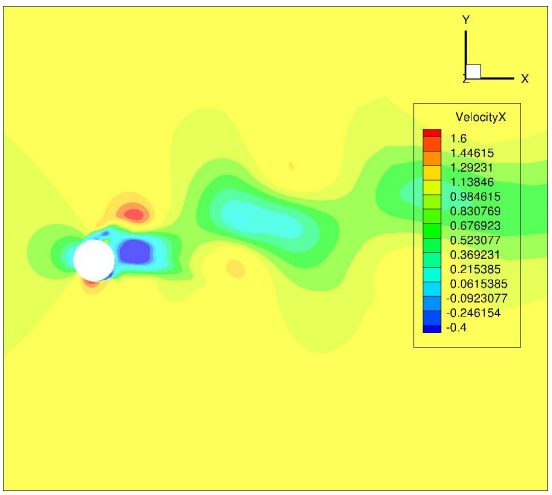

Figure 6.4: Instantaneous x velocity plot for the **MVG-BC-MVG** setup, at the point of minimum lift coefficient, for $U_R = 3.0$.

Figures 6.3 and 6.4 display the coalescence pattern identified by Williamson in [19] (C mode), in which the small structures coalesce in the cylinder's nearest wake.

6.2.2 Near wake for $U_R = 5.0$

For $U_R = 5.0$, figures 6.5 and 6.6 display the shedding of single, counter-rotating vortices in the cylinder near wake, according to the **2S** pattern identified by Williamson [19], in which two single vortices are shed per cycle.

6.2.3 Near wake for $U_R = 10.0$

Concerning the near wake for the case with $U_R = 10$, the complete absence of a vortical synchronization pattern - as stated by Williamson in [19] - is not entirely clear through the observation of figures 6.7 and 6.8. Furthermore, it can be argued that there is still a resemblance between the x velocity field corresponding to the cases of $U_R = 5.0$ and $U_R = 10.0$. Thus, it is not possible to identify a clear 2S mode, nor a complete absence of pattern.

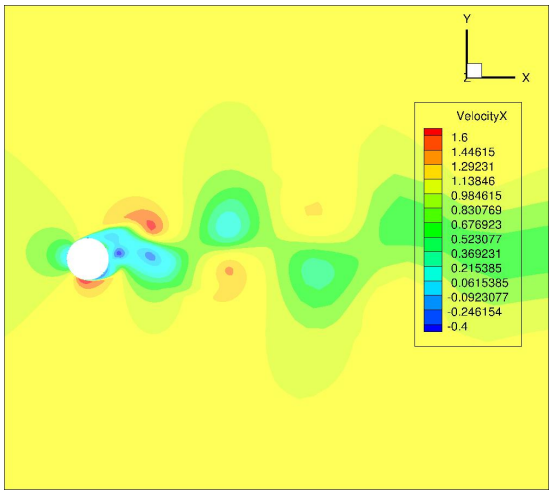

Figure 6.5: Instantaneous x velocity plot for the **RBF-BC-DEF** setup, at the point of minimum lift coefficient, for $U_R = 5.0$.

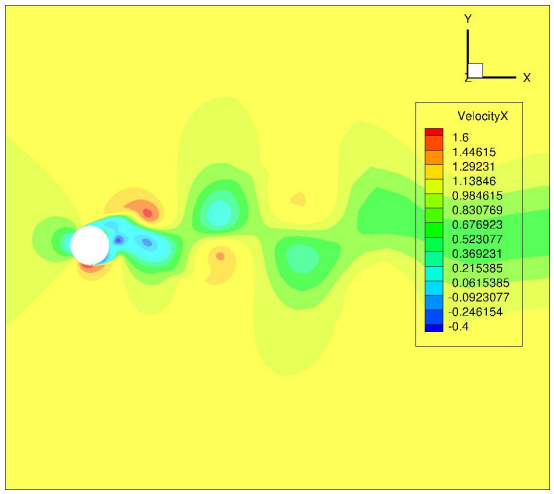

Figure 6.6: Instantaneous x velocity plot for the **MVG-BC-MVG** setup, at the point of minimum lift coefficient, for $U_R = 5.0$.

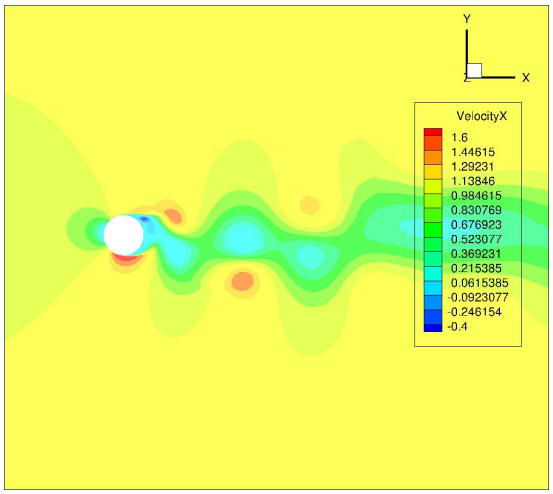

Figure 6.7: Instantaneous x velocity plot for the **RBF-BC-DEF** setup, at the point of minimum lift coefficient, for $U_R = 10.0$.

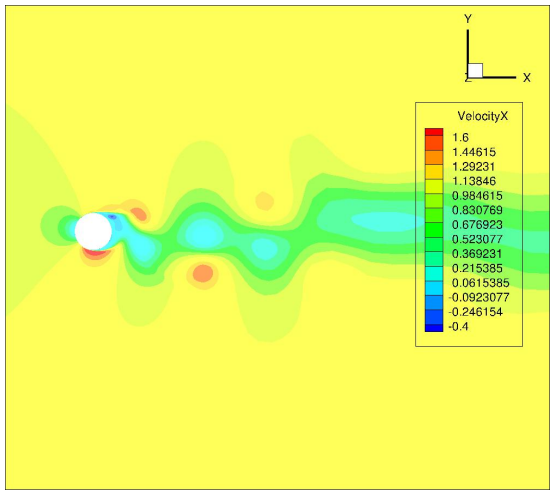

Figure 6.8: Instantaneous x velocity plot for the **MVG-BC-MVG** setup, at the point of minimum lift coefficient, for $U_R = 10.0$.

6.3 Lift force phase and influence on the average value of C_L

As mentioned so far, the analysis of the lift force throughout this study (for all the selected test cases) was essential to gain further insight on some of the physical characteristics of the problem. When dealing with a symmetrical domain with respect to the x direction, and with symmetrical excitation amplitude with respect to the same axis (for the imposed motion cases), one may wonder about the expected value for the average lift force. Theoretically - and taking as a reference the fixed case - it would be reasonable to assume that CL_{avg} would be zero. However, an important aspect that stood out while performing the statistical post-processing of the available data (computing average, minimum, maximum and *rms* values for the quantities of interest) was that the average value of the lift force coefficient was found to be **different** from zero, for some of the imposed motion cases. In the fixed cases, and in the case of

$U_R = 5.0$, the residual value found for CL_{avg} was found to tend to zero with grid refinement (that is, for the finest grids used in each of the test cases, values of the order of magnitude of 10^{-5}, 10^{-6} were reached for CL_{avg}). Nevertheless, the test cases corresponding to $U_R = 3.0$ and $U_R = 10.0$ yielded non-zero values in a more consistent way: namely, values of the order of magnitude 10^{-2}, 10^{-1} were obtained in the test case $U_R = 3.0$, sometimes with a positive sign, and other times with a negative sign. In order to further explore this behaviour, the time traces of the lift force coefficient were confronted with the translation distance of the cylinder in the y direction, for the RBF-BC-DEF setup and $U_R = 3.0$. Also, the influence of the grid chosen was investigated; thus, the results are presented for grids 40 and 64, in figures 6.9 to 6.12.

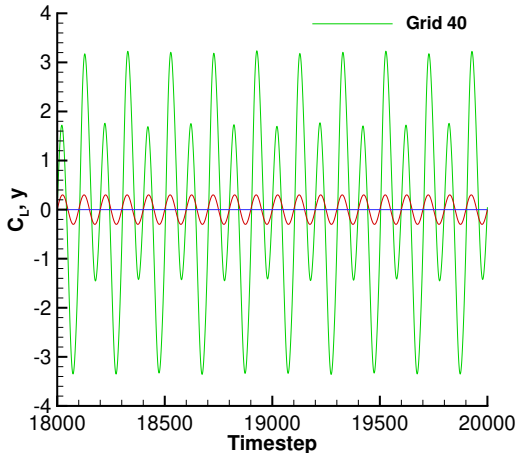

Figure 6.9: Comparison of the time traces of the lift coefficient (green), and the translation distance of the cylinder along the y direction (red), for $U_R = 3.0$, RBF-BC-DEF setup and iterative tolerance of 1×10^{-7}. Result for **grid40**.

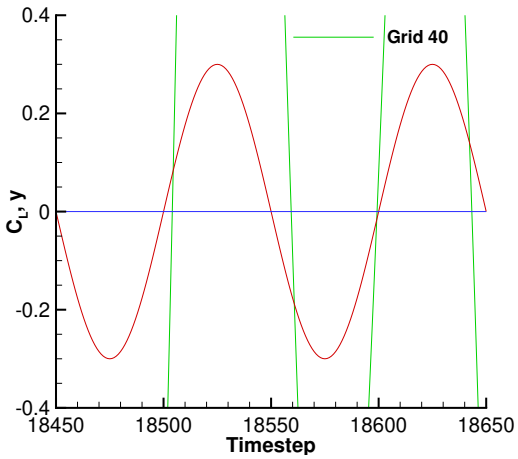

Figure 6.10: Detail of figure 6.9 displaying the lag between the lift force coefficient time trace (green) and the translation distance along the y direction (red). Result for **grid40**.

Figure 6.10 clearly displays an out-of-phase behaviour between the two signals (the blue line $y = 0$ clarifies this aspect). As a result, since there is a clear asynchronism between the lift force and the imposed motion signal, it is expectable to find an assymetry in the flow properties concerning the y direction, namely, a non-zero CL_{avg}. Consequently, this quantity can either tend to a positive or a (symmetric) negative value (which was observed in the several test cases with $U_R = 3.0$, depending on the iterative tolerance, the grid, or the deforming/moving grid method used). In spite of not being entirely clear from figure 6.12, it was observed that the lag between the imposed motion signal and lift force coefficient time trace increased from grid 40 to grid 64. These observations reflect an essential physical feature of the flow around the cylinder, both in the fixed and imposed motion cases: the original "symmetry" that characterizes the problem along the y direction is only kept in the fixed setup and in the lock-in region of the imposed motion cases, when the natural vortex shedding frequency collapses onto the imposed motion frequency (corresponding to $U_R = 5.0$). Otherwise (in the remaining imposed motion cases studied, $U_R = 3.0$ and $U_R = 10.0$), the lag between the lift force and the imposed motion position causes the lift force to oscillate around a non-zero value, which can be positive or negative depending

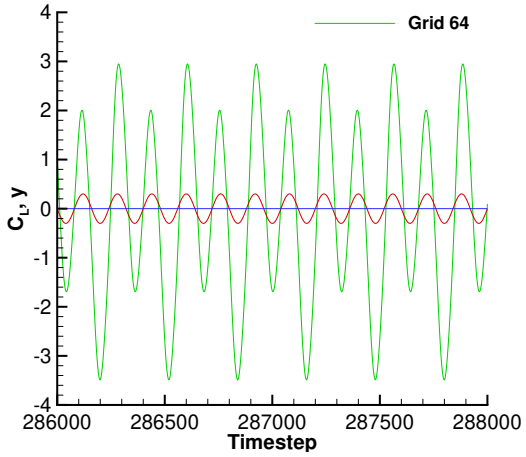

Figure 6.11: Comparison of the time traces of the lift coefficient (green), and the translation distance of the cylinder along the y direction (red), for $U_R = 3.0$, RBF-BC-DEF setup and iterative tolerance of 1×10^{-7}. Result for **grid64**.

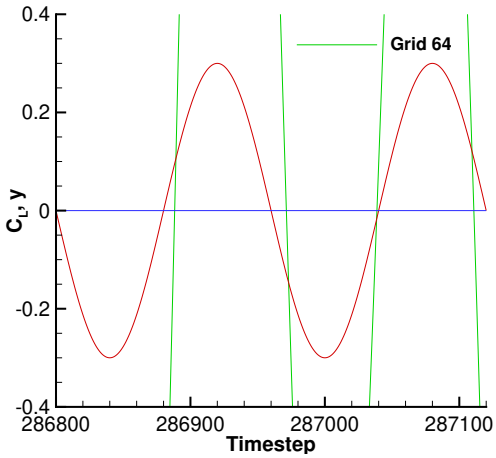

Figure 6.12: Detail of figure 6.11 displaying the lag between the lift force coefficient time trace (green) and the translation distance along the y direction (red). Result for **grid64**.

on the history of the flow (which is affected by the factors mentioned in the previous paragraph). Furthermore, a dependence of the obtained phase lag with respect to the chosen grid is registered, which once more reinforces the desirable goal of increasing grid refinement.

6.4 The choice of a RANS approach with a $k - \omega$ SST turbulence model

In this section an analysis of some of the shortcomings associated with the chosen mathematical formulation is presented. Namely, the following subsections intend to demonstrate that the selected turbulence model ($k - \omega$ SST) does not provide sufficient diffusion to capture only the mean flow properties, especially for the lowest reduced velocity studied, $U_R = 3.0$

6.4.1 Behaviour in fine grids

In the process of selecting the five relevant grids for the grid refinement study, finer grids than **grid 64** were originally considered for the imposed motion test cases with $U_R = 3.0$ and $U_R = 5.0$. Namely, grids **80** and **96** were an early option considered for this analysis.

However, when performing simulations in any of these two finer grids (either for the moving or deforming grid methods - figures 6.14 and 6.16), it was found that the time evolution of the relevant physical quantities displayed unwanted low frequency content. Since the frequencies present in the response appeared to be quite low, a first explanation proposed for this behaviour admitted the reflection of pressure waves in the domain's walls, which would certainly enrich the signal content in frequency. However,

if these were present the solution would still display a periodic behaviour over time (the signal would just possibly be modulated with this additional interference, and would still display some visible periodicity).

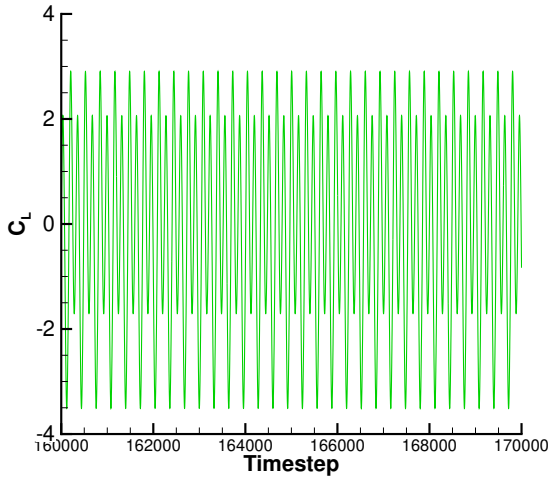

Figure 6.13: Lift coefficient response for the **RBF-BC-MVG** setup, $U_R = 3.0$, using **grid 64** and an iterative tolerance of 5×10^{-6}.

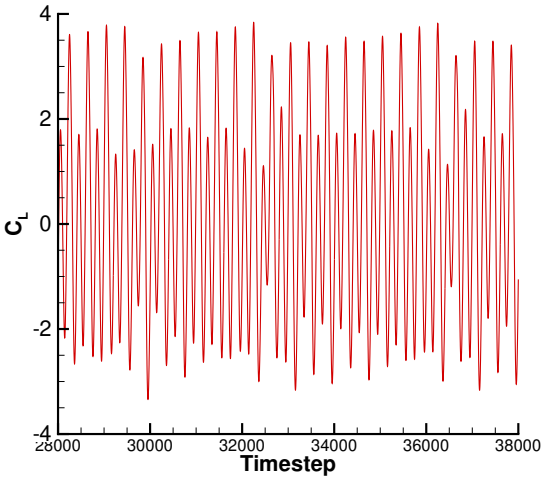

Figure 6.14: Lift coefficient response for the **RBF-BC-MVG** setup, $U_R = 3.0$, using **grid 80** and an iterative tolerance of 5×10^{-6}.

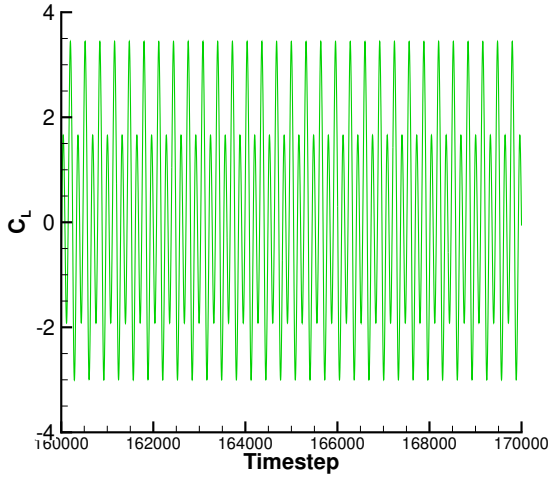

Figure 6.15: Lift coefficient response for the **MVG-BC-MVG** setup, $U_R = 3.0$, using **grid 64** and an iterative tolerance of 5×10^{-6}.

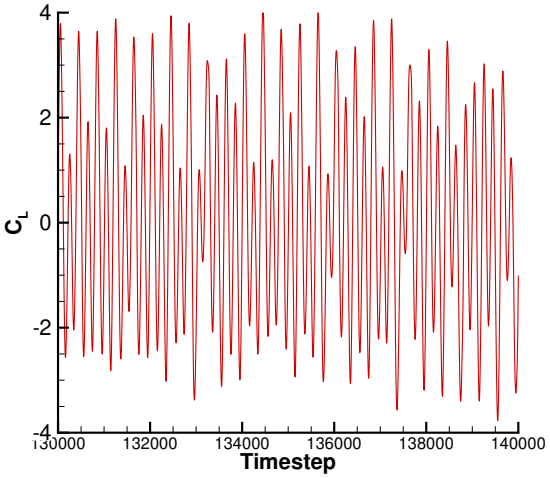

Figure 6.16: Lift coefficient response for the **MVG-BC-MVG** setup, $U_R = 3.0$, using **grid 80** and an iterative tolerance of 5×10^{-6}.

6.4.2 Behaviour in an extended domain

However, and in order to fully confirm/discard this possibility, the calculations were repeated for the **RBF** deforming method, using the boundary conditions corresponding to the moving grid (**RBF-BC-MVG**) and a larger domain (the x distance between the cylinder center and the outlet wall was increased from **78.0 D** to **118.0 D**). Grid **80** was selected for the computation, in order to optimize computation

time (performing the same computation in a finer grid would require more time without any obvious advantage in terms of the topic being analysed in this part). The simulation for this case comprised 20 initial cycles (with a convergence tolerance of 5×10^{-3}) followed by 100 additional cycles (with a convergence tolerance of 1×10^{-5}).

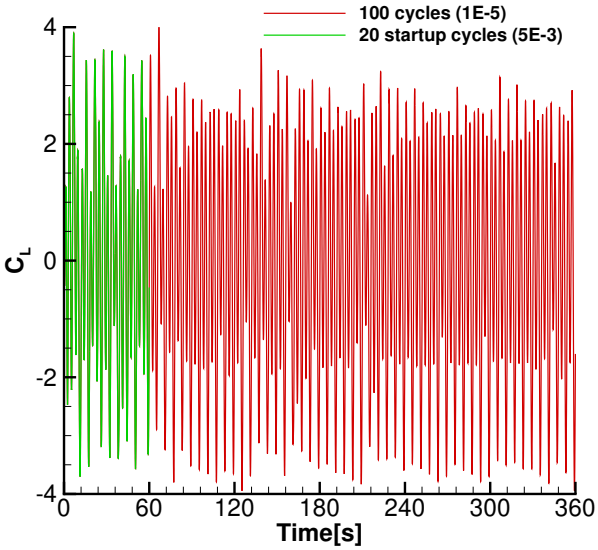

Figure 6.17: Lift coefficient as a function of time for the RBF-BC-MVG setup, using the extended domain (outlet placed at $118.0D$).

The results of this simulation confirmed the original hint: in fact, in spite of the response still exhibiting a rich low-frequency content, the obtained force signals over time did not display any visible periodicity, which allowed discarding the possibility of pressure waves' reflection in the walls of the (possibly too small) domain.

6.4.3 Behaviour when modifying the CFL condition

In order to further analyse this possibility, an alternative approach was adopted, which consisted in repeating the calculations for the 5 possible combinations method+boundary condition (RBF-BC-DEF, RBF-BC-MVG, IDW-BC-DEF, IDW-BC-MVG, MVG-BC-MVG), however using a different timestep. Consequently, the simulations were repeated first using **half** the original value for the timestep, followed by a second test **doubling** the original timestep value. This approach consists in a simple strategy to evaluate the influence of numerical dissipation in the computed solution (thus introducing additional artificial dissipation by analysing the flow at larger timesteps, and reducing the dissipation when halving the originally selected timestep). The results presented concern the (originally) **coarsest** grid used, **grid 32**, and **grid 40**, since there was also a clear lack of dissipation from the turbulence model on the coarsest grids (essentially, the numerical error on coarsest grids produces a reduction of the turbulent viscosity, ultimately creating a need for numerical diffusion in order to correctly capture the mean flow properties). Furthermore, performing these calculations for the coarsest grid allowed a faster confirmation of the aforementioned thesis (since computations required less time).

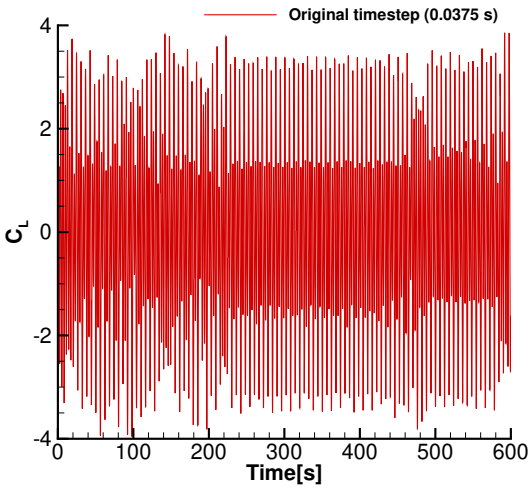

Figure 6.18: Lift coefficient as a function of time for the **RBF-BC-DEF** setup, **grid 32**, using the original timestep of $\Delta t = 0.0375s$.

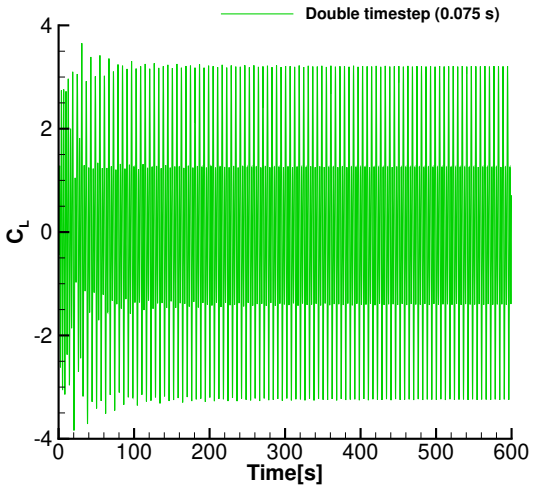

Figure 6.19: Lift coefficient as a function of time for the **RBF-BC-DEF** setup, **grid 32**, doubling the timestep to $\Delta t = 0.075s$.

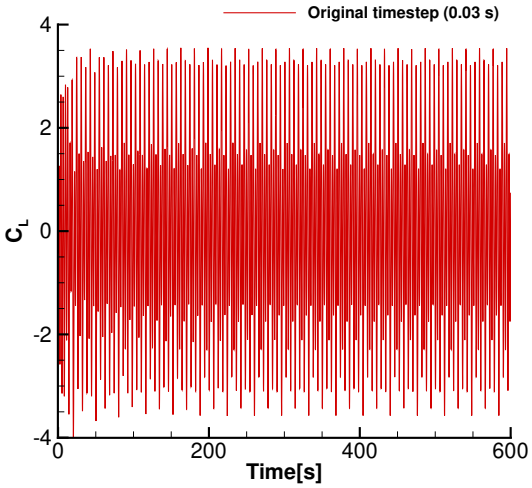

Figure 6.20: Lift coefficient as a function of time for the **IDW-BC-MVG** setup, **grid 40**, using the original timestep of $\Delta t = 0.03s$.

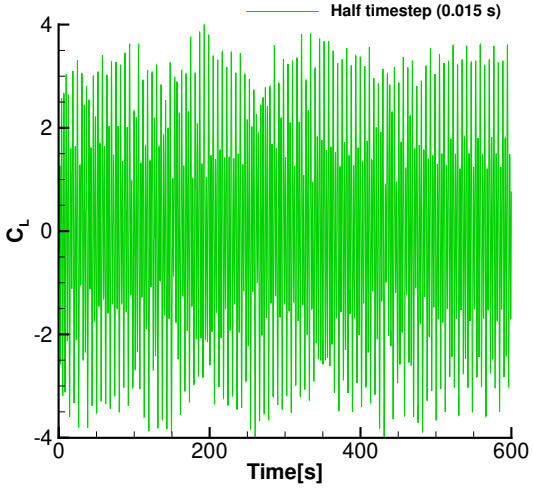

Figure 6.21: Lift coefficient as a function of time for the **IDW-BC-MVG** setup, **grid 40**, halving the timestep to $\Delta t = 0.015s$.

The results of this analysis indeed proved the suspected shortcomings of the turbulence model being used ($k - \omega\ SST$) to close the RANS system of equations. It is visible that using a larger timestep (figures 6.18 and 6.19), some of the originally non-periodic solutions become periodic (indicating that the artificially introduced dissipation prevents the resolution of some of the unwanted frequencies and, conversely, with a smaller timestep (figures 6.20 and 6.21), some of the originally periodic solutions become non-periodic, displaying the aforementioned low-frequency content.

This behaviour confirms that increasing diffusion (numerically, in this case) essentially increases the damping of lower frequencies and correctly captures the mean-flow properties. The same happens when the discretisation scheme used in the equations' convective fluxes is changed to a first order scheme

(again, with more numerical diffusion). This analysis can be found in appendix B, section B.3.

6.4.4 Modelling limitations of a RANS formulation in statistically unsteady flows

After investigating the aspects mentioned in the previous subsections, the study pointed to an analysis of the modelling limitations of the selected formulation. In order to correctly capture the mean flow properties, the turbulence model used in the calculations has to ensure enough dissipation to prevent the resolution of lower frequencies and to keep the validity of the RANS formulation in a statistically unsteady problem. From the previous analysis, it is clear that this is not verified for the case of $U_R = 3.0$.

As stated by Pereira in [49], the success of using a RANS formulation will naturally depend on the "ability of the closure strategy to represent the flow field". That is, the RANS approach will essentially be appropriate when the largest, energy containing scales of turbulence are accurately modelled. For the practical case of this study - a statistically unsteady flow - this would imply a good separation (in terms of the frequency spectrum) between the mean flow and the turbulent structures. However, as it has been shown along this analysis, the presence of coherent structures (such as the vortex shedding phenomenon) essentially poses a possible interaction with turbulent structures, then making the "analysis of flow-fields non-trivial", as observed by Pereira in [49].

Furthermore, as previously mentioned in chapter 2, Williamson [17] had already identified the "developing instability of the separating shear layers from the sides of the body" and stated that "three-dimensional structures on the scale of the shear layer vortices were expected to appear in this regime", when analysing the shear-layer transition regime, comprising the range of Reynolds numbers from 1000 to 200000.

All in all, the aforementioned aspects support the narrow range of application of a RANS formulation in statistically unsteady flows - confirmed by the numerical simulations run in the course of the present work - and pose the need to accurately define this range with precise indicators.

6.4.5 Indicators to evaluate the suitability of the RANS approach

An aspect that was considered relevant at this point of the analysis was the definition of appropriate indicators to evaluate the suitability of a RANS formulation, closed with a $k-\omega$ SST turbulence model. In order to perform this evaluation, the **effective Reynolds number** (defined as follows), and previously proposed by Pereira [49] was used:

$$Re_{eff} = \frac{U_\infty D}{\nu + \nu_t} = Re \frac{1}{1 + \frac{\nu_t}{\nu}} \tag{6.1}$$

As stated by Pereira in [49], "an effect of modelling a fraction of the turbulence field is the reduction of the effective Reynolds number at which the computations are performed". Hence, a qualitative indicator

of how appropriate the mathematical modelling is (meaning that only the mean flow is captured and turbulence is entirely modelled) will be the extension of regions in which a low effective Reynolds number is observed (specifically, lower than 1000, which corresponds to the onset of the shear layer transition regime identified by Williamson in [17]) in the cylinder near wake).

Figures 6.22 to 6.24 display the differences in the onset of the shear layer transition regime found for all three imposed motion cases ($U_R = 3.0, 5.0, 10.0$). Naturally, due to a difference in the external excitation frequency, the region corresponding to an effective Reynolds number lower than 1000 will be different in each of the three cases. However, after identifying this region in all cases (say, for reference grid 64), it is possible to evaluate how the effective Reynolds number changes in the near wake when the grid is refined.

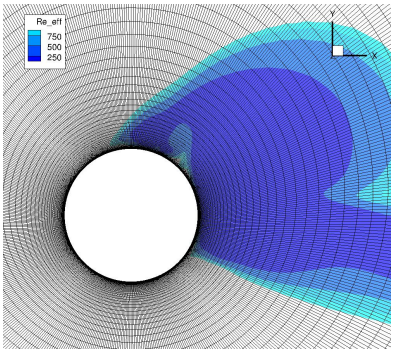

Figure 6.22: Effective Reynolds number in the cylinder near wake, at the point of minimum lift coefficient, for grid 64, using the RBF-BC-DEF setup at a reduced velocity $U_R = 3.0$.

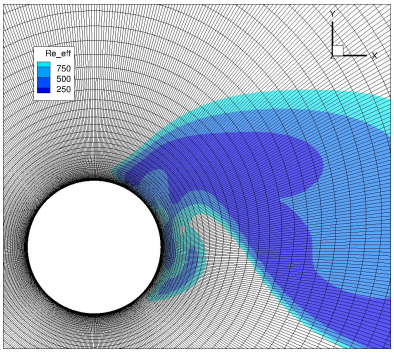

Figure 6.23: Effective Reynolds number in the cylinder near wake, at the point of minimum lift coefficient, for grid 64, using the RBF-BC-DEF setup at a reduced velocity $U_R = 5.0$.

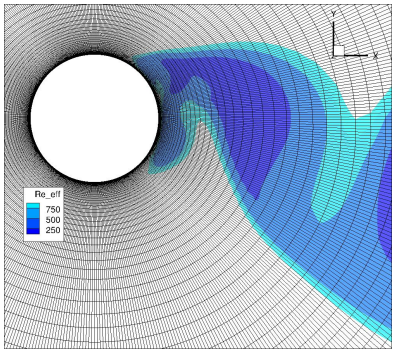

Figure 6.24: Effective Reynolds number in the cylinder near wake, at the point of minimum lift coefficient, for grid 64, using the RBF-BC-DEF setup at a reduced velocity $U_R = 10.0$.

Thus, in order to evaluate the behaviour of the selected indicator (the effective Reynolds number) with grid refinement, the flow field was also evaluated for the RBF-BC-DEF setup, at the point of minimum C_L, for grid 64 (figure 6.22) and grid 80, $U_R = 3.0$, in order to capture potential differences. The obtained result is presented in figures 6.25 and 6.26. It is possible to observe that the extension of the region where $Re_{eff} < 1000$ is observed clearly decreases when refining the grid (from grid 64 to grid 80), which reinforces the hypothesis that the turbulence model used for closure is not efficiently damping out the unwanted fluctuations, leading to an undesired resolution (instead of modelling) of turbulent scales.

The use of this indicator essentially reveals a viable strategy to qualitatively assess the suitability of the chosen modelling approach. Moreover, the monitoring of local variables (velocity, pressure) at given points on the cylinder near wake, which clearly display the appearance of unwanted frequency content with grid refinement, (as revealed by the figures included in appendix B for further analysis) strengthens the analysis carried out so far, thus shedding additional light on RANS modelling properties in statistically unsteady flows.

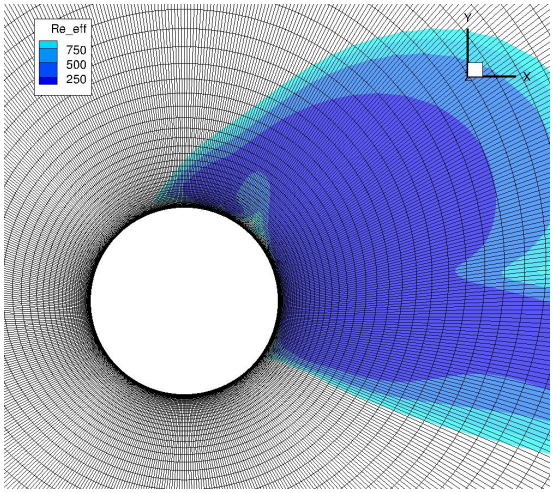

Figure 6.25: Effective Reynolds number in the cylinder near wake, at the point of minimum lift coefficient, **for grid 64**, using the RBF-BC-DEF setup at a reduced velocity $U_R = 3.0$.

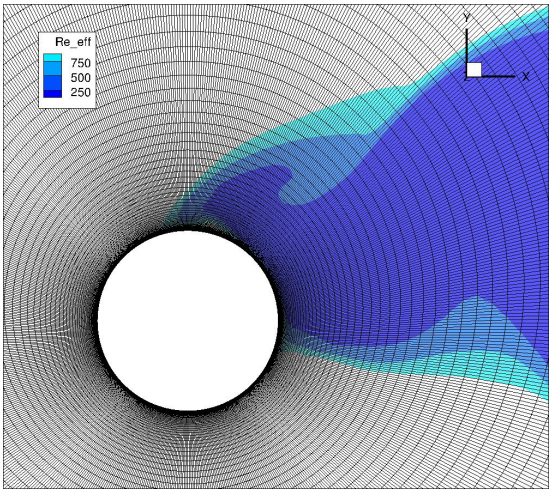

Figure 6.26: Effective Reynolds number in the cylinder near wake, at the point of minimum lift coefficient, **for grid 80**, using the RBF-BC-DEF setup at a reduced velocity $U_R = 3.0$.

Chapter 7

Conclusions

The present section aims at summarising the main achievements obtained with this study, while also identifying useful investigation paths for future work.

7.1 Achievements

It is now relevant to outline some of the most important achievements of the developed work, having in mind the objectives stated in chapter 1.

7.1.1 Effect of the choice of boundary conditions on the computed solution

An extensive comparison of the results obtained with both sets of boundary conditions (BC-DEF and BC-MVG) was performed, both for the fixed and imposed motion scenarios. Overall, it was found that the influence of the chosen BC on the computed solution was negligible, which confirms the initial selection of a sufficiently large computational domain. This observation provides additional confidence in the obtained results, essentially proving that the difference between selecting a computational domain with fixed walls (corresponding to the BC-DEF condition, in which a free-slip condition is applied in the top and bottom walls) or moving walls (corresponding to the BC-MVG condition, in which a zero-pressure condition is applied in the top and bottom walls) can be neglected if the computational domain is selected to be large enough.

7.1.2 Effect of the choice of deforming/moving grid techniques on the computed solution

The first fundamental finding registered when using the moving grid technique was the need to select an appropriate set of boundary conditions that accurately represented the moving walls of the computational domain, in order to avoid artificial pressure oscillations in the computed solution. As stated in previous sections, this motivated the implementation of the second set of boundary conditions (BC-MVG) in order to appropriately simulate the test cases associated with a moving grid approach.

Nevertheless, it was observed that both the two selected deforming grid techniques (*Radial Basis Function* (RBF) and *Inverse Distance Weighting* (IDW) methods) and the moving grid approach yielded comparable results (both for the force coefficients of interest, as seen in chapter 5, and for the near wake vortex synchronization patterns, as seen in chapter 6). This conclusion sustains the suitability of any of the three methods for handling imposed motion, as confirmed by the presently studied cylinder test case (which can be considered an example of a canonical flow).

7.1.3 Main differences registered between the fixed and moving test cases

Apart from the natural differences in the force coefficients' computed statistical values, the main differences registered between the fixed and imposed motion cases were revealed by an extensive frequency analysis of the time history of the forces (mainly in the y direction). One of the expected differences - which was indeed confirmed - was the presence of an additional energy peak in the imposed motion cases, corresponding to the external excitation frequency. Another predictable difference - also confirmed - was the slight shift of the natural vortex shedding frequency (associated with the Strouhal number relation for the fixed case) in the imposed motion cases, with respect to the fixed ones.

7.1.4 Quality of the modelling approach in statistically unsteady problems

One the most surprising findings yielded by this analysis concerns the behaviour of the frequency content in both fixed and imposed motion scenarios with respect to grid refinement. Whereas in the 2D fixed case and in the 2D imposed motion cases with larger reduced velocities (say, $U_R = 10.0$) grid refinement did not cause the resolution of unwanted frequencies, the 2D imposed motion cases corresponding to lower reduced velocities (say, $U_R = 3.0$) were dramatically affected when the grid was refined, displaying well distributed, low frequency content.

This behaviour was attributed to a particularly strong lack of diffusion in the latter cases, which essentially caused an undesired resolution of lower frequencies by the model, preventing an appropriate capturing of the mean flow properties and ultimately questioning the validity of a RANS formulation complemented with a $k-\omega$ SST turbulence model in these cases. Equations solved by unsteady RANS are equivalent to those solved by mathematical models that partially solve turbulence/fluctuations, and the function of the turbulence model is to avoid the appearance of such fluctuations in the solution.

7.1.5 Main differences registered between the 2D and 3D cases

An important finding brought by the (brief) 3D analysis carried out in the present work was the confirmation of the already identified (in the 2D analysis) limitations of the RANS formulation for statistically unsteady problems.

However, the obtained 3D numerical results (along with the experimental data found in the work of Gopalkrishnan [30]) were extremely helpful to identify similarities in the computed force coefficients for lower reduced velocities ($U_R = 3.0$), while outlining some differences for larger reduced velocities, thus

hinting at a preponderance of convective terms over diffusive terms in the overall momentum balance for cases with a larger external frequency of excitation (conversely, with a lower reduced velocity).

7.2 Future Work

The final conclusions yielded by the present study display significant potential for future work. Essentially, the specification of sensors/quantities that define the suitability of a RANS formulation in statistically unsteady problems could be a future path to identify flow conditions for which a RANS approach complemented with a $k-\omega$ SST turbulence model can be safely used in order to correctly represent mean flow quantities.

Another important aspect that could be further detailed - combined with the findings already gathered with respect to the modelling properties of the RANS formulation - is the 3D analysis performed in the present study. In spite of the identified limitations in this study, a greater number of test cases could essentially provide a more complete insight on the suitability of the mathematical formulation, potentially not yet revealed by the 2D test cases which were extensively analysed in the present work. Namely, the 3D test case for $U_R = 5.0$ could benefit from a grid refinement study in order to better assess the proximity of the obtained result with respect to the experimental data. Furthermore, the present study could also be extended to test cases concerning freely-moving cylinders, in order to grasp relevant differences in the suitability of the mathematical formulation with respect to the fixed and imposed motion cases herein analysed. In this freely-moving cylinder, the work carried out in the present study (comparing the moving/deforming grid techniques and outlining similarities between them) is particularly helpful, as an approach with a moving grid in this setup might not be feasible.

As for the identification/development of relevant sensors to provide a stronger assessment of the RANS formulation modelling properties, the work of Pereira [49] has already presented successful contributions concerning this aspect. In order to extend the already developed analysis, the use of the effective Reynolds number (computed with local velocity, instead of the reference velocity, U_∞), could yield additional information to provide a better distinction between the cases with different reduced velocities. Additionally, a technique to identify the relative importance of convective/diffusive terms in the overall momentum balance could be developed, thus quantifying the contribution of diffusion from the turbulence model in each test case.

Finally, assessing the behaviour of a different turbulence model (possibly the $k-\omega$, which does not feature a turbulent viscosity limiter, instead of the herein used $k-\omega$ SST, which includes one) could be a useful pathway for additional investigation. Furthermore, it would also be interesting to analyse the use of hybrid models (featuring a RANS formulation in the boundary layer and a LES formulation elsewhere) in order to identify if the mean flow properties are accurately captured in this case.

Bibliography

[1] D. B. Armstrong, A. Najafi-Yazdi, and L. Mongeau. Numerical Simulations of Flow over a Landing Gear with Noise Reduction Devices using the Lattice-Boltzmann Method. AIAA 2013-2114, R&D Department, Heroux-Devtek, St-Hubert, QC, J3Y 9G1, Canada, May 2013. 19th AIAA/CEAS Aeroacoustics Conference. doi:10.2514/6.2013-2114.

[2] T. Imamura, T. Hirai, K. Amemiya, Y. Yokokawa, S. Enomoto, and K. Yamamoto. Aerodynamic and Aeroacoustic Simulations of a Two-wheel Landing Gear. volume 1, pages 293–302. IUTAM Symposium on Computational Aero-Acoustics for Aircraft Noise Prediction, 2010. doi:10.1016/j.proeng.2010.09.031.

[3] S. Gildersleeve, D. Clingman, and M. Amitay. Flow around Low Aspect Ratio Cylinders and their Applications for Flow Control. AIAA 2017-1449, Grapevine, Texas, 2017. AIAA SciTech Forum, 55th AIAA Aerospace Sciences Meeting. doi:10.2514/6.2017-1449.

[4] R. T. Gonçalves, G. R. Franzini, G. F. Rosetti, J. R. Meneghini, and A. L. C. Fujarra. Flow around circular cylinders with very low aspect ratio. *Journal of Fluids and Structures*, 54:122–141, 2015. doi:10.1016/j.jfluidstructs.2014.11.003.

[5] R. T. Gonçalves, J. R. Meneghini, and A. L. C. Fujarra. Vortex-induced vibration of floating circular cylinders with very low aspect ratio. *Ocean Engineering*, 154:234–251, 2018. doi:10.1016/j.oceaneng.2018.02.019.

[6] P. P. S. de Paula Lopes. *A CFD Investigation on the Flow around a Low Aspect Ratio Vertical Cylinder: Modeling Free Surface and Turbulent Effects*. Escola Politécnica da Universidade de São Paulo, 2019.

[7] G. F. Rosetti, G. Vaz, and A. L. C. Fujarra. On the Effects of Turbulence Modeling on the Fluid-Structure Interaction of a Rigid Cylinder. *Proceedings of the ASME 2016 35th International Conference on Ocean, Offshore and Arctic Engineering*, June 2016. doi:10.1115/OMAE2016-54989.

[8] *ReFRESCO controls documentation*, . version 2.5.0.

[9] M. S. Adaramola, O. G. Akinlade, D. Sumner, D. J. Bergstrom, and A. J. Schenstead. Turbulent wake of a finite circular cylinder of small aspect ratio. *Journal of Fluids and Structures*, (22):919–928, July 2007. doi:10.1016/j.jfluidstructs.2006.04.007.

[10] D. Sumner. Flow above the free end of a surface-mounted finite-height circular cylinder: A review. *Journal of Fluids and Structures*, (43):41–63, 2013.

[11] A. D. Hay. Flow About Semi-submerged Cylinders of Finite Length. *Princeton University Report*, 1947.

[12] G. F. Rosetti and G. Vaz. On the numerical simulations of captive, driven and freely moving cylinder. *Journal of Fluids and Structures*, (74):492–519, Aug. 2017. doi:10.1016/j.jfluidstructs.2017.06.013.

[13] J. L. Heseltine. *Flow Around a Circular Cylinder with a Free End*. University of Saskatchewan, Department of Mechanical Engineering, 2003.

[14] T. Kawamura, M. Hiwada, T. Hibino, I. Mabuchi, and M. Kumada. Flow around a Finite Circular Cylinder on a Flat Plate (cylinder height greater than turbulent boundary layer thickness). *Bulletin of JSME (The Japan Society of Mechanical Engineers)*, 27(232), Oct. 1984. doi:10.1299/jsme1958.27.2142.

[15] S. Tanaka and S. Murata. An Investigation of the Wake Structure and Aerodynamic Characteristics of a Finite Circular Cylinder (Time-Averaged Wake Structures behind Circular Cylinders with Various Aspect Ratios). *JSME International Journal*, 42(2), 1999. doi:10.1299/jsmeb.42.178.

[16] T. v. Kármán. Uber den Mechanismus den Widerstands, den ein bewegter Korper in einer Flussigkeit erfahrt. *Göttingen Nachr.*, 12:509–517, 1912.

[17] C. H. K. Williamson. *Vortex dynamics in the cylinder wake*. Mechanical and Aerospace Engineering, Upson Hall, Cornell University, 1996.

[18] A. Roshko. *On the development of turbulent wakes from vortex streets*. National Advisory Committee for Aeronautics, Report 1191, 1954.

[19] C. H. K. Williamson and A. Roshko. Vortex formation in the wake of an oscillating cylinder. *Journal of Fluids and Structures*, 2:355–381, Jan. 1988. doi:10.1016/S0889-9746(88)90058-8.

[20] J. H. Ferziger and M. Peric. *Computational Methods for Fluid Dynamics*. Springer-Verlag Berlin Heidelberg 2002, 3rd edition, 2002.

[21] G. Alfonsi. Reynolds-Averaged Navier-Stokes Equations for Turbulence Modeling. *Applied Mechanics Reviews*, (62), July 2009. doi:10.1115/1.3124648.

[22] H. Tennekes and J. L. Lumley. *A First Course in Turbulence*. MIT Press, Cambridge, MA, 1972.

[23] F. R. Menter. Zonal Two Equation $k-\omega$ Turbulence Models for Aerodynamic Flows. Number 93-2906. AIAA 24th Fluid Dynamics Conference, American Institute of Aeronautics and Astronautics, July 1993.

[24] D. C. Wilcox. Reassessment of the Scale-Determining Equation for Advanced Turbulence Models. *AIAA Journal*, 26(11), November 1988. doi:10.2514/3.10041.

[25] D. A. Johnson and L. S. King. A Mathematically Simple Turbulence Closure Model for Attached and Separated Turbulent Boundary Layers. *AIAA Journal*, 23(11), Nov. 1985.

[26] S. J. Kline, W. C. Reynolds, F. A. Schraub, and P. W. Runstadler. The structure of turbulent boundary layers. *Journal of Fluid Mechanics*, 30:741–773, Feb. 1967.

[27] F. R. Menter, M. Kuntz, and R. Langtry. Ten years of Industrial Experience with the SST Turbulence Model. *Turbulence, Heat and Mass Transfer*, 4, 2003. Begell House, Inc.

[28] NASA Langley Research Center Turbulence Modeling Resource: The Menter Shear Stress Transport Turbulence Model. https://turbmodels.larc.nasa.gov/sst.html.

[29] L. Eça. On the Limiter of the Production Term of the k Transport Equation in the SST $k-\omega$ Eddy-Viscosity Turbulence Model. Technical report, MARIN/IST Cooperative Research Project, may 2008.

[30] R. Gopalkrishnan. *Vortex-Induced Forces on Oscillating Bluff Cylinders*. Doctoral dissertation, Woods Hole Oceanographic Institution Massachusetts Institute of Technology, Woods Hole, Massachusetts 02543, February 1993. WHOI-92-38.

[31] ReFRESCO official webpage. http://www.refresco.org/resources/overview-2/, . [Online, accessed 30.10.2019].

[32] Portable Extensible Toolkit for Scientific Computation. https://www.mcs.anl.gov/petsc/index.html. [Online, accessed 30.10.2019].

[33] L. Eça. Grid Generation Tools for Structured Grids. Technical report, MARIN/IST Cooperative Research Project, may 2003.

[34] L. Eça, G. Vaz, H. Abreu, and G. Saraiva. The Pros and Cons of Wall Functions. OMAE2015-41518, St. John's, NL, Canada, June 2015. Proceedings of ASME 34rd International Conference on Ocean, Offshore and Arctic Engineering OMAE2015. doi:10.1115/OMAE2015-41518.

[35] P. Coulier and E. Darve. Efficient mesh deformation based on radial basis function interpolation by means of the inverse fast multipole method. *Computer methods in applied mechanics and engineering*, (308):286–309, June 2016. doi:10.1016/j.cma.2016.05.029.

[36] A. de Boer, M. S. van der Schoot, and H. Bijl. Mesh deformation based on radial basis function interpolation. *Computers & Structures*, (85):784–795, 2007. doi:10.1016/j.compstruc.2007.01.013.

[37] J. Windt. Incompressible Flow Simulations on Moving and Deforming Grids - Part II: Mesh Deformation. Final Report 70058-2-RD, ARD Maritime Research Institute Netherlands, Haagsteg 2 6708 PM Wageningen The Netherlands, September 2013. ARD 2013.

[38] T. C. S. Rendall and C. B. Allen. Efficient mesh motion using radial basis functions with data reduction algorithms. *Journal of Computational Physics*, (228):6231–6249, 2009. doi:10.1016/j.jcp.2009.05.013.

[39] J. Windt. Improvement of the Grid Deformation Methods in ReFRESCO. Final Report 70058-7-RD, ARD Maritime Research Institute Netherlands, Haagsteg 2 6708 PM Wageningen The Netherlands, January 2015. ARD 2014.

[40] M. A. Potsdam and G. P. Guruswamy. A parallel multiblock mesh movement scheme for complex aeroelastic applications. Tech. Report 2001-0716, AIAA, 2001.

[41] S. Spekreijse, B. Prananta, and J. Kok. A simple, robust and fast algorithm to compute deformations of multi-block structured grids. Tech. Report NLR-TP-2002-105, National Aerospace Laboratory NLR, 2002.

[42] Y. Wang, N. Qin, and N. Zhao. Fast dynamic meshing method based on Delaunay graph and Inverse Distance Weighting interpolation. volume 42. Sixth International Symposium on Physics of Fluids, International Journal of Modern Physics: Conference Series, June 2016. doi:10.1142/S2010194516601666.

[43] J. A. S. Witteveen. Explicit and robust inverse distance weighting mesh deformation for CFD. 48th AIAA Aerospace Sciences Meeting Including the New Horizons Forum and Aerospace Exposition, AIAA, Inc., 2010.

[44] L. Eça and M. Hoekstra. A procedure for the estimation of the numerical uncertainty of CFD calculations based on grid refinement studies. *Journal of Computational Physics*, 262:104–130, Jan. 2014. doi:10.1016/j.jcp.2014.01.006.

[45] M. Burgin and O. Duman. Statistical Convergence and Convergence in Statistics. Technical report, University of California and TOBB Economics and Technology University, January 2007.

[46] J. Brouwer, J. Tukker, and M. van Rijsbergen. Uncertainty Analysis of Finite Length Measurement Signals. pages 260–274, Gdansk, Poland, 2013. 3rd International Conference on Advanced Model Measurement Technology for the EU Maritime Industry (AMT'13).

[47] L. Eça, G. Vaz, S. L. Toxopeus, and M. Hoekstra. Numerical Errors in Unsteady Flow Simulations. *Journal of Verification, Validation and Uncertainty Quantification*, 4, June 2019. doi:10.1115/1.4043975.

[48] I. B. Celik, U. Ghia, P. J. Roache, and C. J. Freitas. Procedure for Estimation and Reporting of Uncertainty Due to Discretization in CFD Applications. *ASME Journal of Fluids Engineering*, 130, July 2008. doi:10.1115/1.2960953.

[49] F. M. S. Pereira. *Towards Predictive Scale-Resolving Simulations of Turbulent External Flows*. Phd degree in computational engineering, Instituto Superior Técnico, 2018.

Appendix A

Deforming/moving grid setups: details concerning the simulations

A.1 The deforming grid setup

In this section a practical analysis concerning some of the simulations using the deforming grid setup is presented. Namely, the choice of some relevant parameters is reviewed, and the practical effects of combining the use of deforming grid functions with some of the *ReFRESCO* software features are explored.

A.1.1 The RBF method and the support radius

The first case to be explored employed the use of the RBF method for grid deformation. One of the main parameters to be selected when using this technique is the support radius. The choice of this parameter can either be based on the maximum motion experienced by the grid (relatively to the reference mesh) [8] or on the characteristic length of the computational domain [36]. The former approach recommends a value "*at least five times larger*" than the largest amplitude of motion, whilst the latter suggests a value of "2.5 *times the characteristic length of the computational domain*", that is, the diameter of the cylinder. Bearing in mind the reference amplitude of motion ($\mathbf{A/D = 0.3}$), the second approach was chosen, since it yielded the most conservative approach (a larger support radius, in this case).

Figures A.1 and A.2 show the time evolution of the drag and lift force coefficient (respectively), for a simulation using the RBF technique for grid deformation, $U_R = 3.0$, with the BC-DEF set of boundary conditions, and a support radius of $2.5D$ (according to the aforementioned guidelines found in the literature).

A brief analysis of the figures reveals that neither the drag nor the lift coefficient are periodic over time. After confrontation with these results, some hypotheses that would possibly explain the origin of this behaviour were analysed:

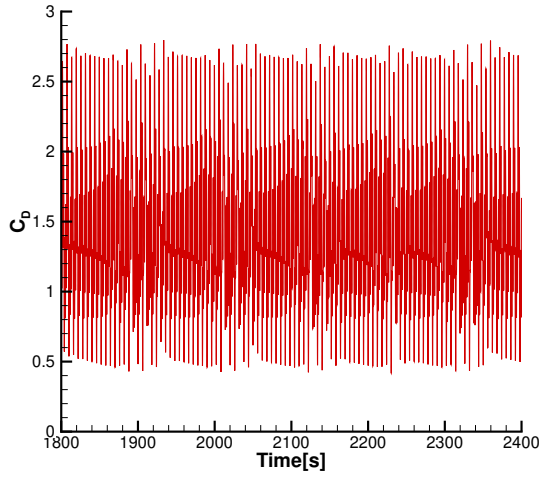

Figure A.1: Time response of drag force coefficient for an iterative convergence tolerance of 5×10^{-6} **(grid 64)**.

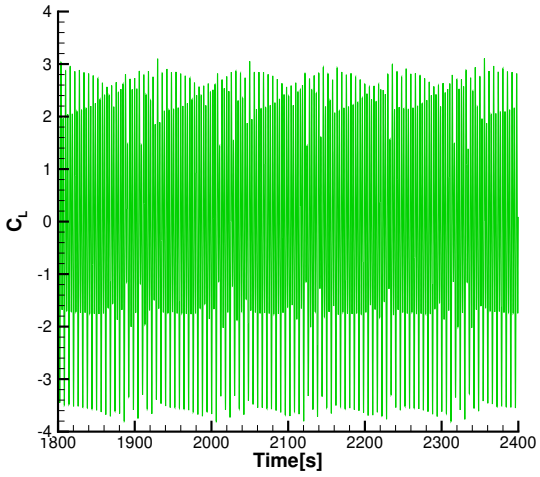

Figure A.2: Time response of lift force coefficient for an iterative convergence tolerance of 5×10^{-6} **(grid 64)**.

- The cumulative influence of the iterative error;
- The influence of the support radius.

The first possibility was soon discarded, since the remaining simulations (run with higher values for the convergence tolerance) did not indicate a significant dependence of the fluctuating trend on the convergence tolerance. Therefore, the iterative error was found to be of little relevance for the solution of this problem.

The influence of the support radius, however, was then investigated (in spite of the literature recommendations), since the fluctuations in the time response could potentially indicate low mesh quality (leading to a "contamination" of the solution). As a second approach, a support radius of $4.0D$ was selected (since this corresponded to a value slightly larger than the radius of the first mesh block around the cylinder, $3.5D$), which was believed to guarantee sufficient mesh quality in the near-cylinder-wall region (a naturally critical area for the force computation).

As expected, this second attempt yielded drag and lift signals over time that no longer displayed these fluctuations, as can be seen in the several examples using the RBF setup exposed in the main body of the present work.

A.1.2 The IDW method: exponent for the weighting function and absorption coefficient

The simulations performed using the IDW deforming technique proved to be quite straightforward. The parameters required in the input file (when using the software *ReFRESCO*) mainly concerned the exponent used in the weighting function (as it was previously described), the application (or not) of local grid

rotation, and an absorption coefficient which defines how far into the domain a boundary displacement should influence the interior node displacement. Since the problem being analysed only concerns translation, the rotation parameter was not used, and the remaining exponent and absorption coefficient were selected according to the default values suggested in the *ReFRESCO* documentation [8]. The values are presented below (table A.1):

IDW method	
Interpolation type	1
Power exponent 1	3
Power exponent 2	5
η	5

Table A.1: Choice of parameters for the IDW method.

According to the software documentation [8], the interpolation type 1 selects the most advanced interpolation method implemented in the software, while both the power exponents and η are constants used to compute the inverse distance weighting function. After analysing the simulation results, it was considered that the tuning of these parameters was not necessary, since the lift and drag force time responses yielded values quite comparable to the ones obtained with the RBF technique. A summary of the results (statistical values of interest) obtained using the IDW method together with the BC-DEF set of boundary conditions is presented below (tables A.2 and A.3), for an iterative tolerance of 5×10^{-6}:

Number of cycles considered	CD_{avg}	CL_{avg}	CD_{rms}	CL_{rms}
N-2T	1.47412806510417	-0.096288802776042	1.57012757444559	1.87782761733842
N-4T	1.4741281140625	-0.096288521239583	1.57012744570011	1.87782739976968
N-6T	1.47412894583333	-0.096287491211806	1.57012829487012	1.87782733533194
N-8T	1.47412884648437	-0.096287336108073	1.57012816385482	1.8778268779716
N-10T	1.47412863666667	-0.096287678832292	1.57012795259426	1.87782678566016
N-12T	1.47412853272569	-0.096287933546007	1.57012784766269	1.87782687939253
N-14T	1.47412857544643	-0.096287881828869	1.57012786452826	1.87782695660347
N-16T	1.47412866653646	-0.096287852191406	1.57012792509445	1.87782687497065

Table A.2: Statistical convergence study for the IDW-BC-DEF case. Average and rms force coefficients.

Number of cycles considered	CD_{min}	CL_{min}	CD_{max}	CL_{max}
N-2T	0.583316599906382	-3.43683210609743	2.71444045496173	3.02053231790369
N-4T	0.58331659992109	-3.43683197616338	2.71444045519456	3.02053231788159
N-6T	0.583316599717364	-3.43683197628707	2.71444212161441	3.02054381182028
N-8T	0.583316595967276	-3.43683197535574	2.71444212191273	3.02054381182825
N-10T	0.583316596021177	-3.43683196976781	2.71444212086499	3.02054381137714
N-12T	0.583316596224904	-3.43683210609743	2.71444200018595	3.0205438118428
N-14T	0.583316595293582	-3.43683194540063	2.71444200025871	3.02054381370544
N-16T	0.583316594362259	-3.43683194555342	2.71444199979305	3.02054382115602

Table A.3: Statistical convergence study for the IDW-BC-DEF case. Minimum and maximum force coefficients.

Analysing tables A.2 and A.3, it can be seen that the variability in the statistical values of interest (according to the number of signal cycles being analysed) is roughly in the same order of magnitude of the chosen iterative convergence tolerance, which indicates that the signal is statistically converged.

A.2 The moving grid setup

In this section the practical effects of the combination of the moving grid method with the originally established set of boundary conditions (BC-DEF) is explored, and the motivation for the analysis of a new set of boundary conditions is explained.

A.2.1 The moving grid method: the motivation for a new set of boundary conditions

The first approach selected for the simulations using the moving grid method consisted in choosing the boundary condition originally used with the deforming grid setup (so far designated as BC-DEF). However, analysing the data yielded by the calculations, it was soon noticed that the choice of boundary conditions compromised the solution quality, introducing undesirable fluctuations in the forces' response over time. This particular finding then motivated an alternative approach, in which the boundary conditions were modified. These differed from the boundary conditions used in the deforming grids' setup in the following aspects:

- The **outlet condition**: the streamwise derivatives of all dependent variables were set to zero ($\frac{\partial \phi}{\partial x} = 0$);
- The condition at the **top and bottom walls** of the tank: pressure was specified to be zero (in order to avoid free pressure values in the direction of motion of the cylinder), and the normal derivatives of the remaining quantities were set to zero ($\frac{\partial \phi}{\partial y} = 0$).

The drag and lift coefficients' response over time is presented in figures A.3 and A.4, respectively. The fluctuations - commonly present only at the beginning of the simulation - remain present throughout, even for considerably low iterative tolerance values. This allowed discarding the influence of the iterative error in the solution and motivated the aforementioned modifications in the original set of boundary conditions.

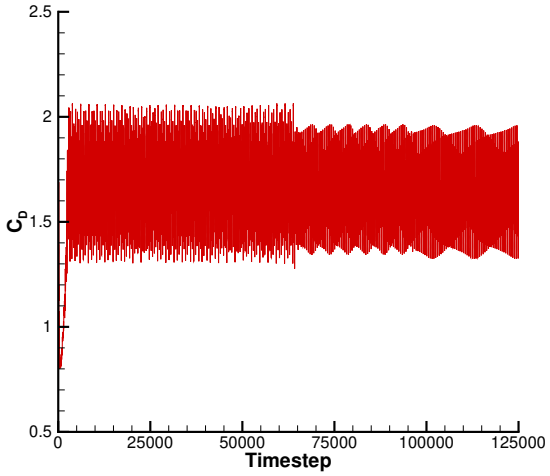

Figure A.3: Drag coefficient response for the **MVG-BC-DEF** setup, using **grid 64**.

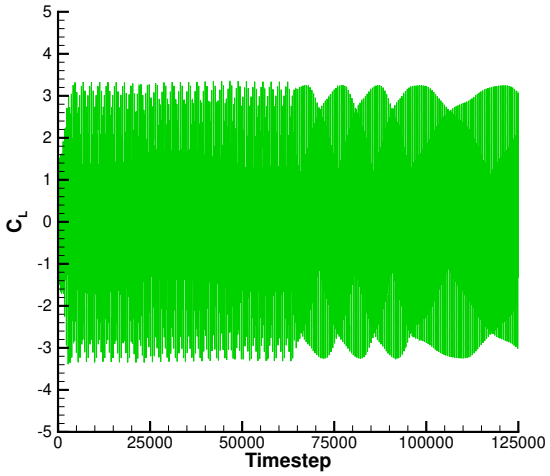

Figure A.4: Lift coefficient response for the **MVG-BC-DEF** setup, using **grid 64**.

Appendix B

Indicators to evaluate the suitability of the RANS formulation

B.1 Effective Reynolds numbers plots

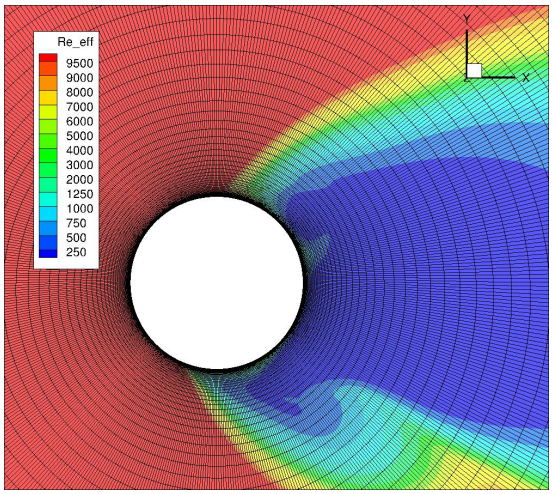

Figure B.1: Re_{eff} for $U_R = 3.0$ at the point of zero C_L (approximately), for the RBF-BC-DEF setup, **grid 64**.

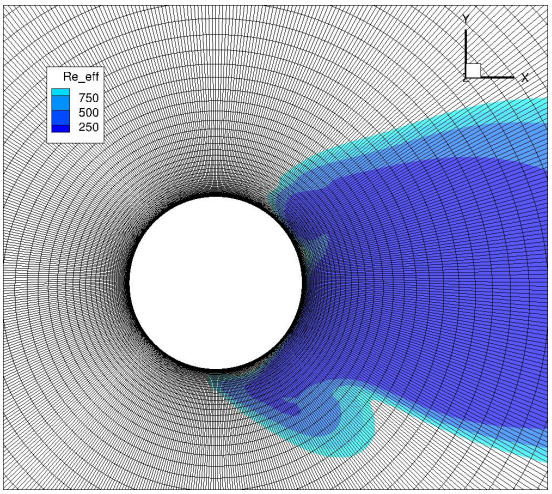

Figure B.2: Regions with $Re_{eff} < 1000$ for $U_R = 3.0$ at the point of zero C_L (approximately), for the RBF-BC-DEF setup, **grid 64**.

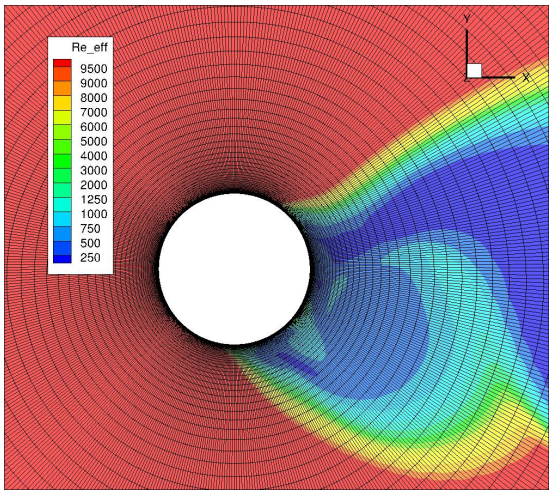

Figure B.3: Re_{eff} for $U_R = 5.0$ at the point of zero C_L (approximately), for the RBF-BC-DEF setup, **grid 64**.

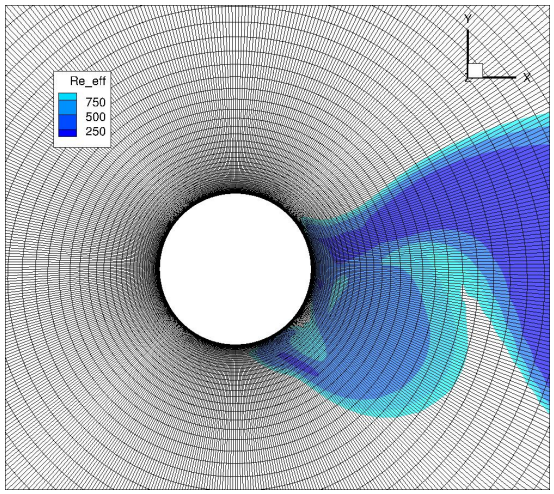

Figure B.4: Regions with $Re_{eff} < 1000$ for $U_R = 5.0$ at the point of zero C_L (approximately), for the RBF-BC-DEF setup, **grid 64**.

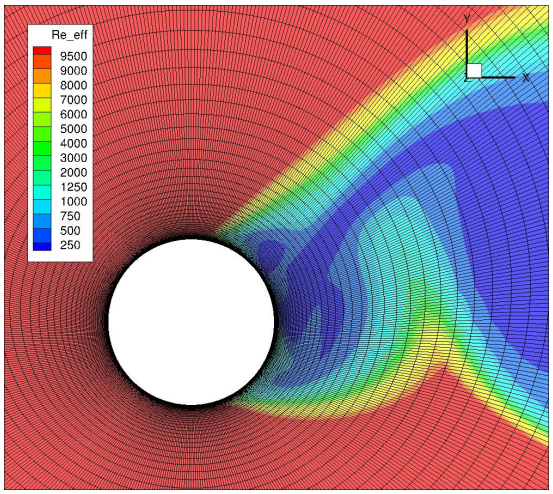

Figure B.5: Re_{eff} for $U_R = 10.0$ at the point of zero C_L (approximately), for the RBF-BC-DEF setup, **grid 64**.

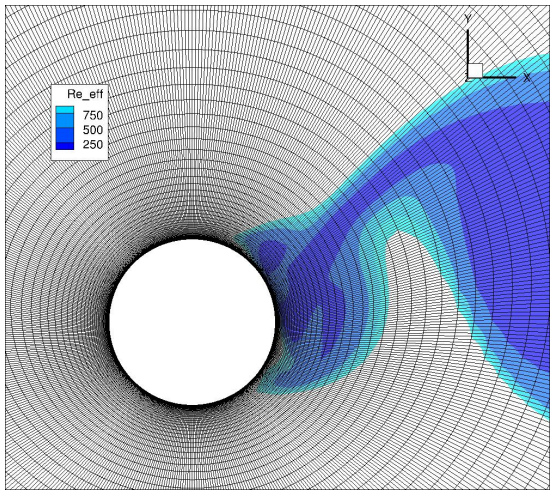

Figure B.6: Regions with $Re_{eff} < 1000$ for $U_R = 10.0$ at the point of zero C_L (approximately), for the RBF-BC-DEF setup, **grid 64**.

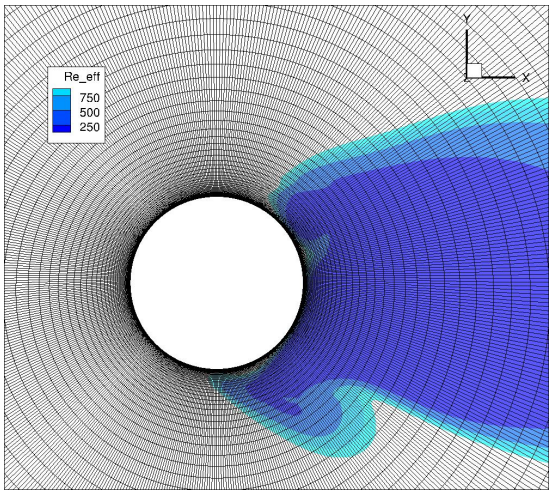

Figure B.7: Regions with $Re_{eff} < 1000$ for $U_R = 3.0$ at the point of zero C_L (approximately), for the RBF-BC-DEF setup, **grid 64**.

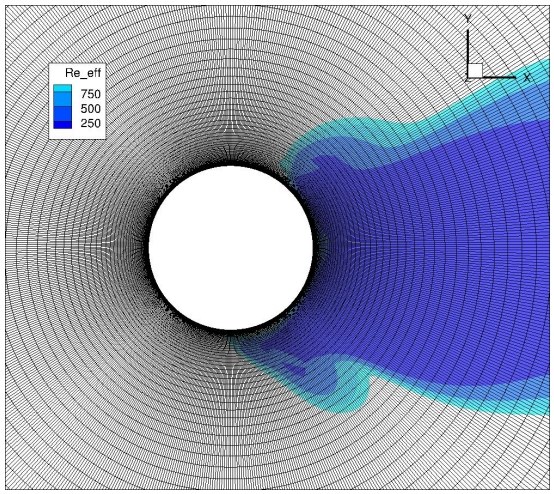

Figure B.8: Regions with $Re_{eff} < 1000$ for $U_R = 3.0$ at the point of zero C_L (approximately), for the RBF-BC-DEF setup, **grid 80**.

B.2 Monitoring local variables in the cylinder vicinity

B.2.1 Velocity (x component)

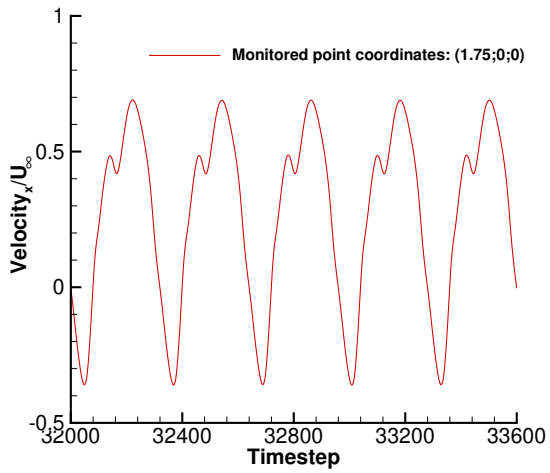

Figure B.9: Velocity (x component) monitored at the point of coordinates $(1.75D; 0; 0)$, for $U_R = 3.0$, **grid 64**, using the RBF-BC-DEF setup.

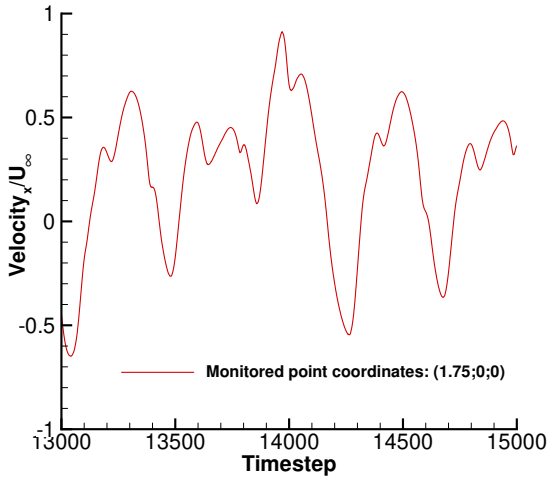

Figure B.10: Velocity (x component) monitored at the point of coordinates $(1.75D; 0; 0)$, for $U_R = 3.0$, **grid 80**, using the RBF-BC-DEF setup.

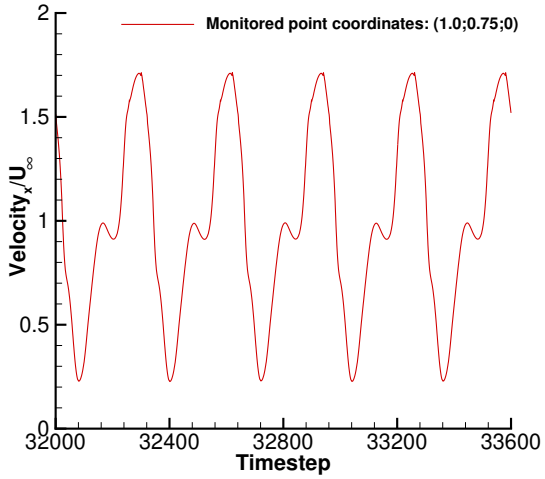

Figure B.11: Velocity (x component) monitored at the point of coordinates $(1.0D; 0.75D; 0)$, for $U_R = 3.0$, **grid 64**, using the RBF-BC-DEF setup.

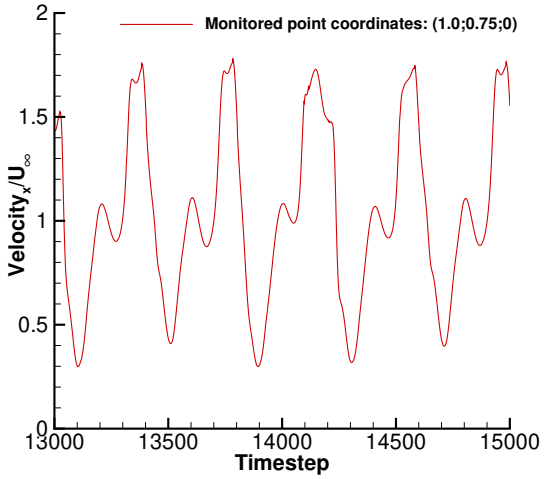

Figure B.12: Velocity (x component) monitored at the point of coordinates $(1.0D; 0.75D; 0)$, for $U_R = 3.0$, **grid 80**, using the RBF-BC-DEF setup.

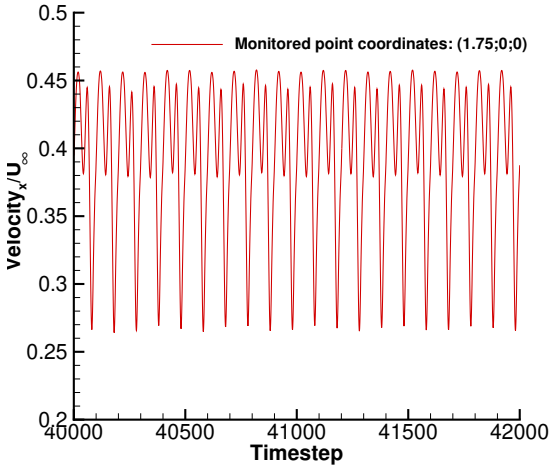

Figure B.13: Velocity (x component) monitored at the point of coordinates $(1.75D; 0; 0)$, for $U_R = 5.0$, **grid 64**, using the RBF-BC-DEF setup.

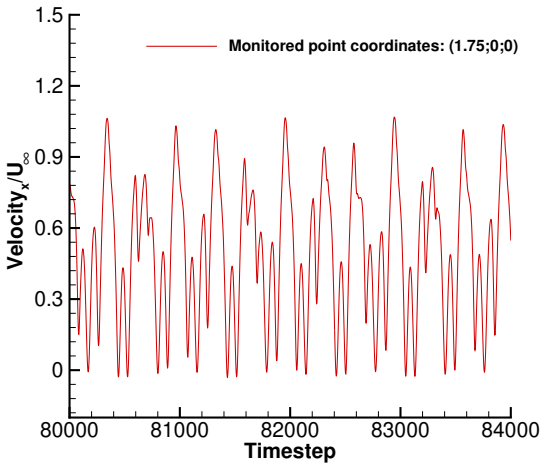

Figure B.14: Velocity (x component) monitored at the point of coordinates $(1.75D; 0; 0)$, for $U_R = 10.0$, **grid 64**, using the RBF-BC-DEF setup.

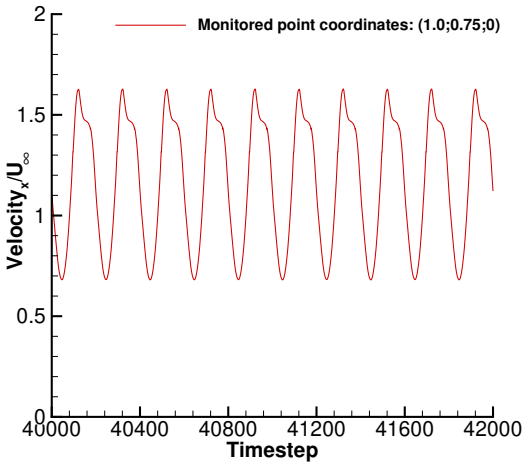

Figure B.15: Velocity (x component) monitored at the point of coordinates $(1.0D; 0.75D; 0)$, for $U_R = 5.0$, **grid 64**, using the RBF-BC-DEF setup.

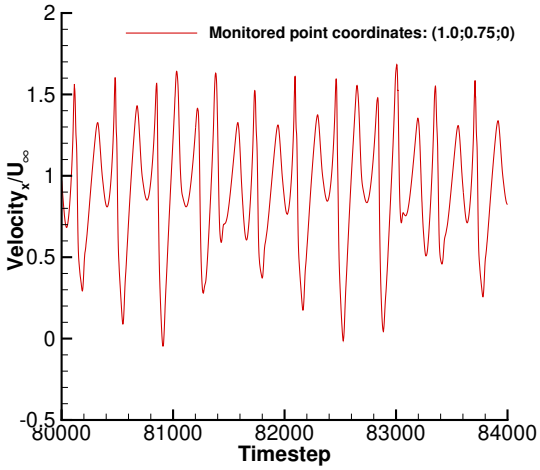

Figure B.16: Velocity (x component) monitored at the point of coordinates $(1.0D; 0.75D; 0)$, for $U_R = 10.0$, **grid 64**, using the RBF-BC-DEF setup.

B.2.2 Pressure

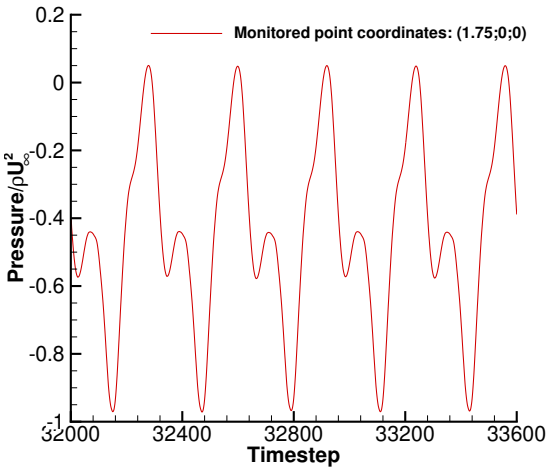

Figure B.17: Pressure monitored at the point of coordinates $(1.75D; 0; 0)$, for $U_R = 3.0$, **grid 64**, using the RBF-BC-DEF setup.

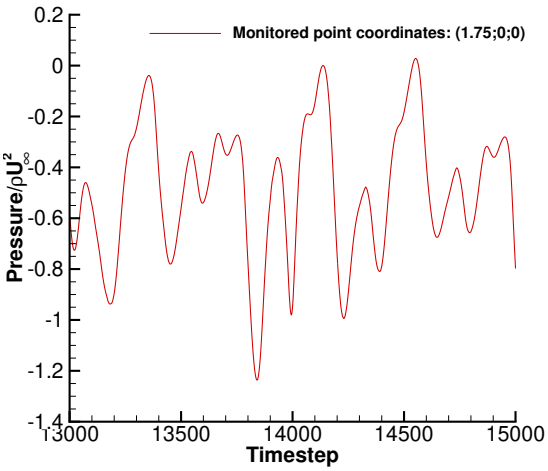

Figure B.18: Pressure monitored at the point of coordinates $(1.75D; 0; 0)$, for $U_R = 3.0$, **grid 80**, using the RBF-BC-DEF setup.

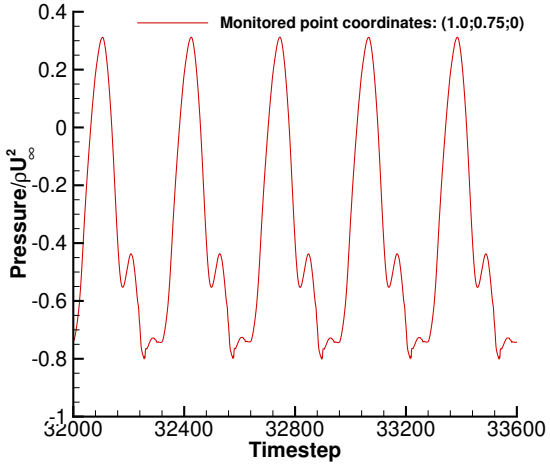

Figure B.19: Pressure monitored at the point of coordinates $(1.0D; 0.75D; 0)$, for $U_R = 3.0$, **grid 64**, using the RBF-BC-DEF setup.

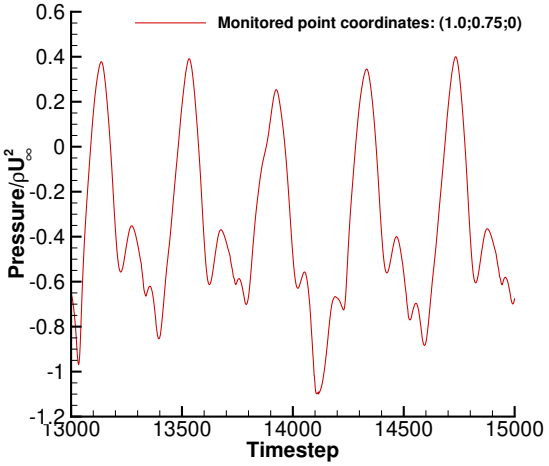

Figure B.20: Pressure monitored at the point of coordinates $(1.0D; 0.75D; 0)$, for $U_R = 3.0$, **grid 80**, using the RBF-BC-DEF setup.

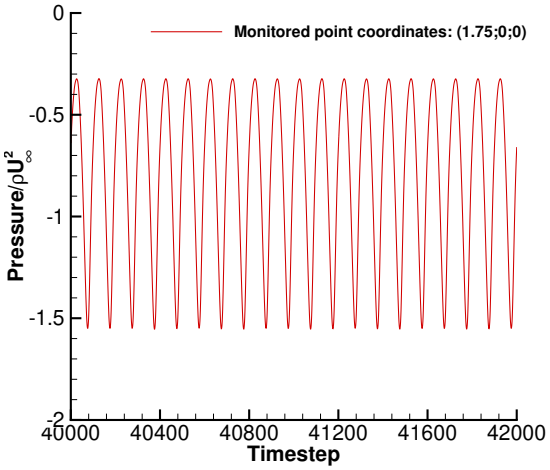

Figure B.21: Pressure monitored at the point of coordinates $(1.75D; 0; 0)$, for $U_R = 5.0$, **grid 64**, using the RBF-BC-DEF setup.

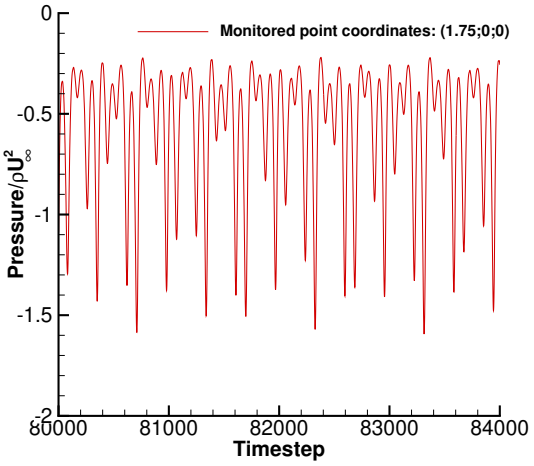

Figure B.22: Pressure monitored at the point of coordinates $(1.75D; 0; 0)$, for $U_R = 10.0$, **grid 64**, using the RBF-BC-DEF setup.

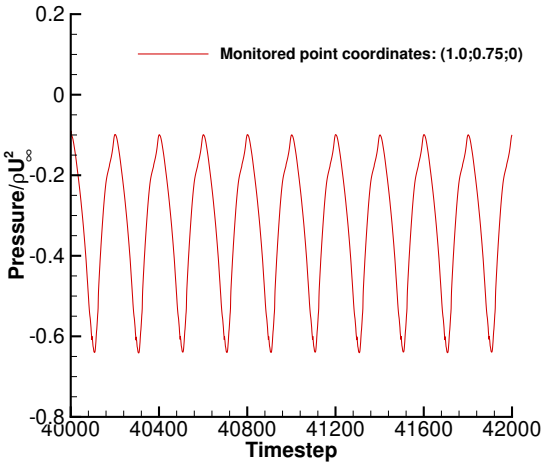

Figure B.23: Pressure monitored at the point of coordinates $(1.0D; 0.75D; 0)$, for $U_R = 5.0$, **grid 64**, using the RBF-BC-DEF setup.

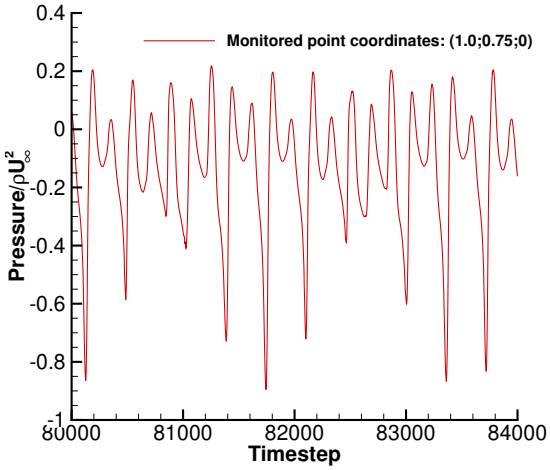

Figure B.24: Pressure monitored at the point of coordinates $(1.0D; 0.75D; 0)$, for $U_R = 10.0$, **grid 64**, using the RBF-BC-DEF setup.

B.3 Evaluating the influence of the convective flux discretisation scheme used in the momentum equations

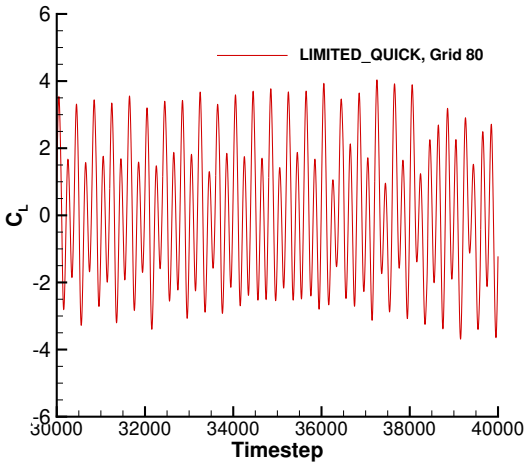

Figure B.25: Lift coefficient signal using the LIMITED QUICK scheme for convective flux discretisation in the momentum equations. Result obtained for **grid 80** using an iterative tolerance of 5×10^{-6}.

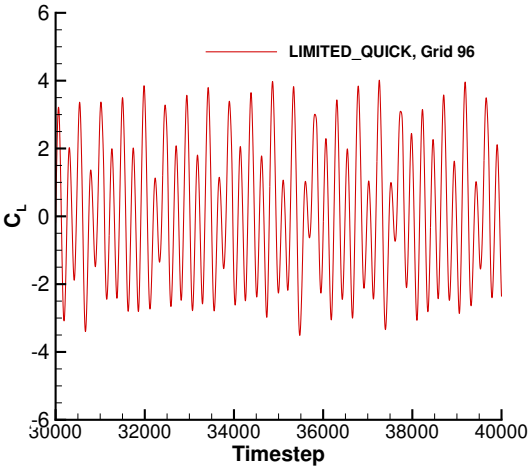

Figure B.26: Lift coefficient signal using the LIMITED QUICK scheme for convective flux discretisation in the momentum equations. Result obtained for **grid 96** using an iterative tolerance of 5×10^{-6}.

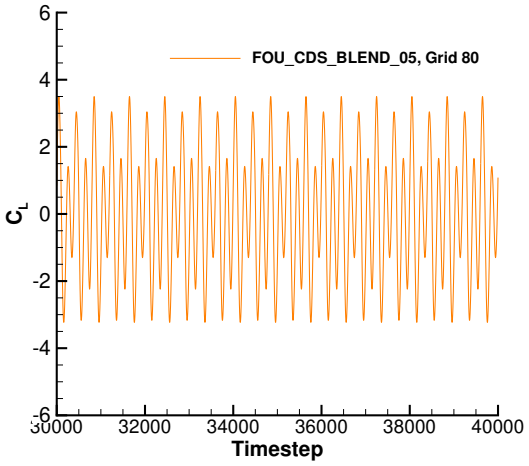

Figure B.27: Lift coefficient signal using a mixed first order upwind/central difference scheme (blending factor 0.5) for convective flux discretisation in the momentum equations. Result obtained for **grid 80** using an iterative tolerance of 5×10^{-6}.

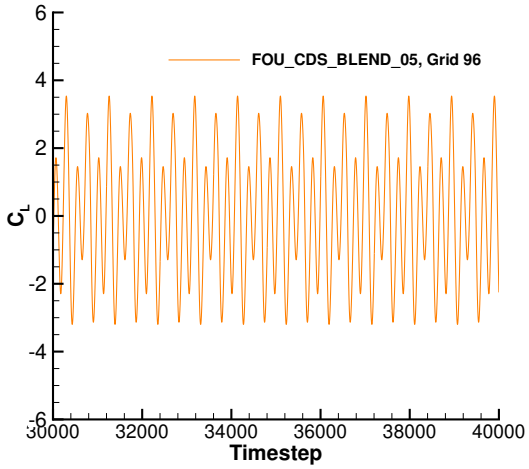

Figure B.28: Lift coefficient signal using a mixed first order upwind/central difference scheme (blending factor 0.5) for convective flux discretisation in the momentum equations. Result obtained for **grid 96** using an iterative tolerance of 5×10^{-6}.

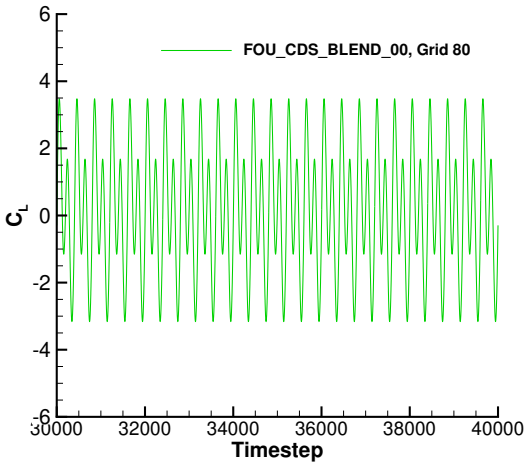

Figure B.29: Lift coefficient signal using a pure first order upwind scheme for convective flux discretisation in the momentum equations. Result obtained for **grid 80** using an iterative tolerance of 5×10^{-6}.

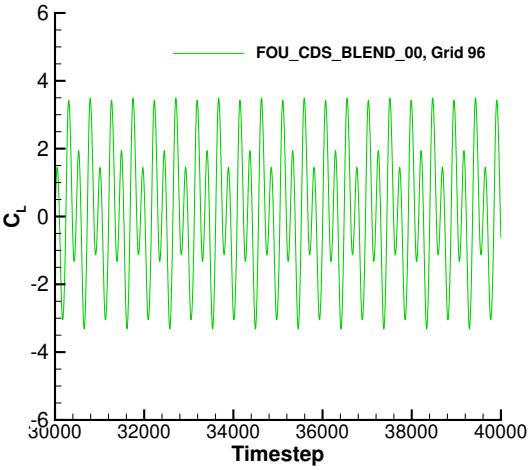

Figure B.30: Lift coefficient signal using a pure first order upwind scheme for convective flux discretisation in the momentum equations. Result obtained for **grid 96** using an iterative tolerance of 5×10^{-6}.